Proceeding
Of
2nd International Conference on Recent Development In Mechanical, Production, Industrial And Automobile Engineering (ICMPIAE 2015)

Date: 25th January 2015
Bangalore

Editor-in-Chief

Prof. Dipak S.Bajaj
Assistant Professor,
Department of Mechanical Engineering,
Amrutvahini College of Engineering,
Sangamner.

Organized by:

About Conference

Technical Research Organisation India (TROI) is pleased to organize the 2nd International Conference on Recent Development In Mechanical, Production, Industrial And Automobile Engineering (ICMPIAE 2015)

ICMPIAE is a comprehensive conference covering the various topics of Mechanical, Production, Industrial and automobile Engineering. The aim of the conference is to gather scholars from all over the world to present advances in the aforementioned fields and to foster an environment conducive to exchanging ideas and information. This conference will also provide a golden opportunity to develop new collaborations and meet experts on the fundamentals, applications, and products of Mechanical, Production, Industrial and automobile engineering. We believe inclusive and wide-ranging conferences such as ICMPIAE can have significant impacts by bringing together experts from the different and often separated fields of Mechanical, Production, Industrial and automobile Engineering. It creating unique opportunities for collaborations and shaping new ideas for experts and researchers. This conference provide an opportunity for delegates to exchange new ideas and application experiences, we also publish their research achievements. ICMPIAE shall provide a plat form to present the strong methodological approach and application focus on Mechanical, Production, Industrial and automobile engineering that will concentrate on various techniques and applications. The conference cover all new theoretical and experimental findings in the fields of Mechanical, Production, Industrial and automobile engineering or any closely related fields.

Topics of interest for submission include, but are not limited to:
Mechanical Engineering
Aerodynamics
Aerospace Systems and Technology
Applied Mechanics
Automation
Biomechanics
Design and Manufacturing
Energy Management
Fluid Dynamics
Fuels and Combustion
Industrial Tribology
Instrumentation and Control
Internal Combustion Engines
Mechatronics
Micro-Machining
Nano- Technology
Robotics
Solid Mechanics
Mechatronics Engineering
Advanced Motion Control
Intelligent Control
System Integration
Automotive and Transportation Systems
Micro Mechatronics
Mechatronics in Energy Systems and many more....

Organizing Committee

Editor-in-Chief:
Prof. Dipak S.Bajaj
Assistant Professor,
Department of Mechanical Engineering,
Amrutvahini College of Engineering,
Sangamner.

Programme Committee Members:
Dr. Dariusz Jacek Jakóbczak
Assistant Professor , Computer Science & Management .
Technical University of Koszalin, Poland

Prof. (Dr.) Arjun P. Ghatule
Director, Sinhgad Institute of Computer Sciences (MCA),Solapur(MS)

Dr. S.P.ANANDARAJ.,
M.Tech(Hon's),Ph.D.,
Sr.Assistant Professor In Cse Dept,
Srec, Warangal

Prof O. V. Krishnaiah Chetty
Dean, Mechanical Engineering
Sri Venkateswara College of Engineering and Technology
Chittoor- Tirupati

Dr. D.J. Ravi
Professor & HOD, Department of ECE
Vidyavardhaka College of Engineering, Mysore

Prof. Roshan Lal
PEC University of Technology/Civil Engineering Department,
Chandigarh, India
rlal_pec@yahoo.co.in

Dr. Bhasker Gupta
Assistant Professor. Jaypee University of Information Technology, Himachal Pradesh

Dr. A. Lakshmi Devi,
Professor, department of electrical engineering,
SVU college of Engineering, Sri Venkateswara university, Tirupati

Dr. Hansa Jeswani
Asso. Professor.,
Sardar Patel College of Engineering, Mumbai

Prof. Shravani Badiganchala

Assistant professor, Shiridi sai institute of science and engineering

Prof. Surjan Balwinder Singh
Associate Professor in the Electrical Engineering Department,
PEC University of Technology, Chandigarh.

Dr. Shilpa Jindal ,
PEC University of Technology (Deemed University), Chandigarh
ji_shilpa@yahoo.co.in

Prof. S. V. Viraktamath
Dept. of E&CE S.D.M. College of Engg. & Technology Dhavalagiri, Dharwad

Subzar Ahmad Bhat
Assistant Professor, Gla University
Dr. G.Suresh Babu
 Professor,Dept. of EEE,CBIT, Hyderabad

Prof .Ramesh
Associate Professor in Mechanical Engineering,
St.Joseph's Institute of Technology

Prof. Sanjith J
Assistant Professor,
Department of Civil Engineering,
Adhichunchanagiri Institute of Technology,
Chikkamagaluru, Karnataka

 Prof.Amit R. Wasnik
Sinhgad Institute of Technology, Pune, Maharashtra

IIT KHARAGPUR
Prof. Rajakumar R. V.
DEAN Acadedemic, rkumar @ ece.iitkgp.ernet.in
Prof. Datta D., ddatta @ ece.iitkgp.ernet.in
Prof. Pathak S S,r,ssp @ ece.iitkgp.ernet.in

XIMB,BHUBANESWAR
Prof Dr. Subhajyoti Ray.M-Stat, (ISI); Fellow, IIM(A),
Dean academic,XIMB-subhajyoti@ximb.ac.in ,

TABLE OF CONTENTS

SL NO	TOPIC	PAGE NO

Editor-in-Chief

Prof. Dipak S.Bajaj

Editorial

The conference is designed to stimulate the young minds including Research Scholars, Academicians, and Practitioners to contribute their ideas, thoughts and nobility in these two integrated disciplines. Even a fraction of active participation deeply influences the magnanimity of this international event. I must acknowledge your response to this conference. I ought to convey that this conference is only a little step towards knowledge, network and relationship.

The conference is first of its kind and gets granted with lot of blessings. I wish all success to the paper presenters.

I congratulate the participants for getting selected at this conference. I extend heart full thanks to members of faculty from different institutions, research scholars, delegates, TROI Family members, members of the technical and organizing committee. Above all I note the salutation towards the almighty.

Editor -in-Chief:
Prof. Dipak S.Bajaj
Assistant Professor,
Department of Mechanical Engineering,
Amrutvahini College of Engineering, Sangamner

STRESS ANALYSIS OF GLASS FIBRE REINFORCED COMPOSITES USED IN WIND TURBINES

Kalyana Chakravarthy P[1],Dr. Raghunandana.K[2]
[1]Assistant Professor Sr. Scale Dept. of Mechatronics, Manipal Institute of Technology, Manipal,   [2]Professor Dept. of Mechatronics, Manipal Institute of Technology, Manipal,

Abstract—Wind turbines transform kinetic energy in the wind into electrical energy. Glass fiber Reinforced Polymer Composite (GFRP) have seen to be the best option for the wind turbines blades due to their high impact strength, light weight and high strength to weight ratio, etc. The objective of this of this paper is to study and analyze the mechanical behavior of GFRP composite specimen subjected to three point flexural loading conditions. GFRP was modeled in ANSYS using SHELL 91element. Loading conditions were simulated and results were recorded. GFRP specimens were fabricated as per ASTM D790 dimensions using hand lay-up process and subjected to three point loading conditions in Instron material testing machine and results were recorded. Simulation results were validated with the experimental results. Study confirms that defining matrix and fiber bonding properties in SHELL 91 element may lead to good agreement between the simulation and experimental results.

   Index Terms—Ansys, composite, glass-fiber, hand lay-up, Instron, material testing, matrix.

I. INTRODUCTION

Composites are materials consisting of two or more chemically distinct constituents on a macro-scale, having a distinct interface separating them and with properties which cannot be obtained by any constituent working individually. Composite contains matrix and reinforcement materials. The reinforcing fibre provides strength and stiffness to the composite, whereas the matrix gives rigidity and environmental resistance. Typically, composite material is formed by reinforcing fibres in a matrix / resin. The reinforcements can be fibers, particulates, and the matrix materials can be metals, plastics, or ceramics.

Polymer composites use thermoset or thermoplastic resins. In case of GFRP composites, glass fibres are reinforced in the polyester resin the reinforcing fibres constitute the backbone of the material and they determine its strength and stiffness in the direction of fibres. The main advantage that enables the widespread use of glass fibres in composites are its competitive price, availability, good usability, ease of processing, high strength and other convenient properties [1]. The most common glass fibres are made of E-glass and S-glass. E-glass is the least expensive of all glass types and it has a wide

application in fibre reinforced plastic industry. S-glass has higher tensile strength and higher modulus than E-glass. However, the higher cost of S-glass-fibres makes them less popular than E-glass. The E-glass fibre is a kind of glass fibre with low alkali, excellent strength, stiffness, ductility, insulation, heat resistance and moisture resistance. E glass is the primary reinforced material of wind turbine blades, having low cost and good applicability. It is a better match with many resins, and the molding process. However, as the density of the E-type fiber is large, it is generally used in smaller blades about 22 meters [2].

Table 1.1 shows the mechanical properties of different glass fibres.

Type	Tensile strength /GPa	Tensile modulus /GPa	Density g/cm³	Elongation %
E-type glass fiber	3.1	74	2.54	2.5-3
S-type glass fiber	4.6	90	2.5	4.0
Carbon fiber	5.5	294	1.76	1.9
Aramid fiber	2.8	124	1.44	2.8
Polyethylene fiber	3.0	172	0.97	2.7
Basalt fiber	3.0~4.8	79.3~93.1	2.80	3.1

Table 1.1 Mechanical properties of different glass fibres.

Wind turbine blades are subjected to external loading which includes flap-wise and edge-wise bending loads, gravitational loads, inertia loads due to pitch and acceleration, as well as torsional loading. The flap-wise loads are caused mainly by wind pressure, while edge-wise load is caused by gravitational force and torque load.

The flap-wise and edge-wise bending loads cause high longitudinal tensile and compressive stress in the blade material. The up-wind side is subjected to tensile stresses, while down-wind side is subjected to compressive stresses [3]. Also environmental conditions such as moisture, icing, heat, rain, chemical corrosions etc. have considerable effect on the life of wind turbine materials.

Because of the above prevalent different types of loads acting on wind turbine blades advanced composites like GFRP are commonly used in blade construction. Traditional E-glass fiber (70-75% by weight) bonded with epoxy or unsaturated polyester resin is the most common resin because it is easier to process, needs no post-curing and is less expensive, Carbon fibre bonded with polyester provides high stiffness and less weight but mainly used for longer turbine blades. Epoxy resin is preferred to polyester for fabricating longer blades for its better tensile and flexural strength. Polyester is easier to process, needs no post-curing and is less expensive. Polypropylene is a new emerging trend in thermoplastic wind turbine blades as it is having an advantage of recyclability [1].

II. FINTE ELEMENT ANALYSIS

Finite element analysis is used to study the behavior of an actual GFRP composite material. Element, SHELL 91 of ANSYS has the following features

- 8-Node Element.
- Non-Linear Structured Shell.
- Layers Permitted-100(Max.)
- Large Strain Capabilities.
- Suitable for laminates and sandwich structures

To ensure that the model created is an accurate mathematical model of a physical prototype, Glass fiber is laid up in a uni-directional manner in the matrix. CADEC Matlab based software *is used to* calculate mechanical properties like Young's *Modulus,* shear *m*odulus*,* and poisson's *r*atio*.* Rules *of* mixtures are applied to calculate the effective mechanical properties. Graph 2.1 shows the young's modulus for Polyester-E-Glass composite for various fibre volume fractions.
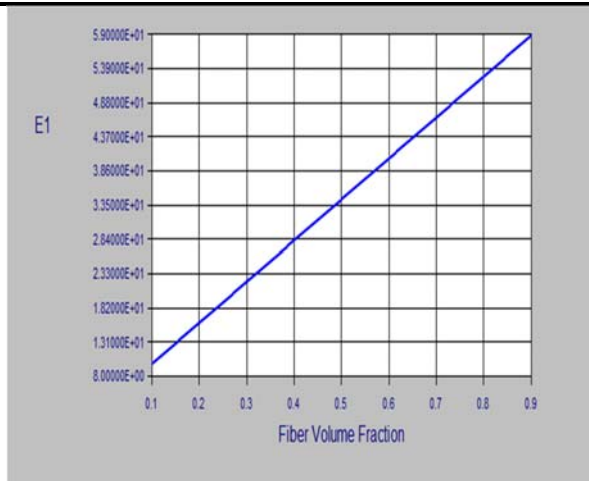
Table 2.1: Polyester-E Glass Young's Modulus for different volume fractions

Figure 2.2: Finite element analysis of 0.16 volume fraction Polyester-E-Glass composite

Polyester-E-Glass composite was modeled in accordance with the Instron Machine setup used for Flexural Analysis. Therefore a 3-point Bending test setup was applied in ANSYS. The load applied was 364.92 N at the middle nodes while at the supporting nodes all DOF are constrained. The composites were modeled using volume fractions of 0.16 and 0.30. Figure 2.2 and 2.3 shows the stress analysis of 0.16 and 0.3 volume fraction Polyester-E-Glass composite performed in ANSYS. The ANSYS model and fabricated specimen have same dimensions, number of layers, fiber orientation, volume fraction and thickness. Subsequently the models were subjected to loads and the nodal solution such as Von Mises Stress was obtained. Figures 2.2 and 2.3 show that the colour pattern observed is in alignment to the stress intensity at that particular region. Ex: Red indicates a highly stressed region whereas the dark blue represents a low intensity region.

Figure 2.3: Finite element analysis of 0.16 volume fraction Polyester-E-Glass composite

III. Specimen Preparation and Testing

The Polyester-E Glass specimens were prepared by hand layup process which is low-cost and the most common processes employed for manufacturing wind turbine blades using fiberglass composites. A release agent, usually in either wax or liquid form, is applied to the chosen mold. This will allow the finished product to be removed cleanly from the mold. Resin – typically a 2-part polyester or epoxy is mixed with its hardener and applied to the surface. Sheets of glass-fibre matting are laid onto the mold, then more resin mixture is added using a brush or roller. The material must conform to the mold, and air must not be trapped between the fibre- glass and the mold.

Additional resin is applied and possibly additional sheets of fibre-glass. Hand pressure, vacuum or rollers are used to make sure the resin saturates and fully wets all layers, and any air pockets are removed before the resin starts to cure. Figure 3.2 shows the hand layup process.

Figure 3.2: Schematic of hand layup process

Figure 3.3 shows the photograph of Polyester-E-Glass composite specimen having 0.16 and 0.3 volume fraction of fibres oriented along the length of the specimen. As per ASTM D790 specimens of dimensions 127×17.5×3.9 mm were prepared by hand lay-up process as discussed above.

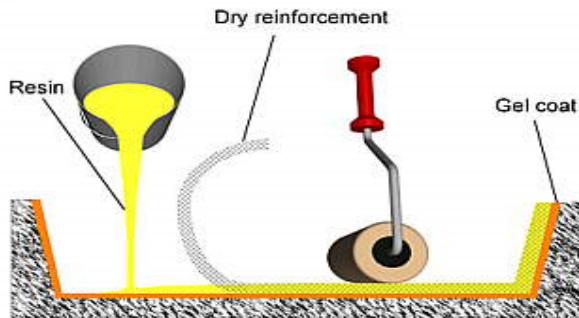Figure 3.3: Photograph of Polyester-E-Glass composite specimen

Instron Universal Testing Machine (UTM) was used for experimental stress analysis of the Polyester-E-Glass composite samples prepared by hand lay-up process. This testing machine meets the testing standards according to ASTM D790. The machine is also used for testing various types of polymer matrix composite specimens according to the necessary type of loading requirement. Various jigs are provided for suitable mounting arrangements of the different specimens like tensile, shear, bending, short beam etc. Figure 3.4 shows the photograph of UTM. The machine consists of a cross head jaw which is fixed between two railings. The cross head is used for applying weight on the specimen when subjected to a particular loading. This crosshead weight applied on the specimen is controlled by a parameter called cross head speed or jaw speed. The crosshead is pneumatically controlled.
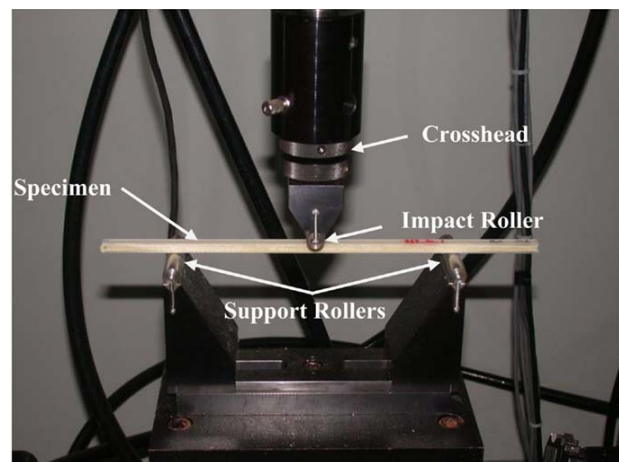
Figure 3.4 Photograph of Instron UTM

The machine is integrated with a computer and software called "Instron Suite". This is used to run the test machine by using input parameters of the sample test specimen such as span length, width, thickness and cross head speed (Z). The cross head speed, when set, will start the cross head to impinge downwards onto the surface of the specimen and the moment it makes contact with the surface, the software will display real time bending strength variation up to the point of fracture. The variation can be observed clearly by looking onto the computer screen where the material deformation is monitored at each instant of time period. For this study, the jig of standard three point flexural test was selected; the specimen is placed on the two supports at a particular span length as shown in figure 3.4. The span length

of 64 mm was used for the experimentation. Once the specimen is placed, the cross head jaw is brought in contact with the surface and the jaw speed is set into motion at a particular feed rate (mm/min). Here for the experimentation, feed rate was set at 1.8 mm/min. Experimental values of flexural strength, flexural modulus, graph of flexural stress vs flexural strain, maximum load up to the point of fracture were recorded.

Three Polyester-E-Glass composite samples with fibre volume fraction of 0.16 were named as specimen A, B and C and were subjected to a 3 point Flexural/Bending Test in the Instron machine. The load was applied up to the point of fracture and the parameters such as flexural strength, flexural modulus, and maximum load at the point of fracture for each specimen was obtained from the machine were recorded. The specimen D without fiber reinforcement was also prepared and subjected to testing to confirm the influence of the fibre in increasing the strength of the composite. All the data obtained during experimentation and simulation are recorded and tabulated in section IV.

IV. Results

The simulation results and experimental results obtained for 0.16 fibre volume fraction were recorded. Figure 4.1,4.2 ,4.3 and 4.4 shows the Instron UTM plot of flexure stress vs flexure strain for sample A, sample B, sample C and sample D respectively. Table 4.1, 4.2, 4.3 and 4.4 shows the Instron UTM stress analysis data of sample A, sample B, sample C and sample D respectively. Table 4.5 shows the CADEC software results which were used for ANSYS analysis. Table 4.6 shows the stress analysis results of ANSYS simulation and table 4.7 shows the summary of stress analysis results obtained by Instron UTM machine.

Figure 4.1: Instron UTM plot of flexure stress vs flexure strain for sample A

	Maximum Load (N)	Flex Modulus (MPa)	Flexure stress at Maximum Flexure load (MPa)	Thickness (mm)	Width (mm)
1	371.27	9173.57	133.90	3.90000	17.50000
2	122.89	2201.08	44.32	3.90000	17.50000
Mean	247.08	5687.32	89.11	3.90000	17.50000
Standard Deviation	175.62555	4930.29606	63.34199	0.00000	0.00000
Minimum	122.89	2201.08	44.32	3.90000	17.50000
Maximum	371.27	9173.57	133.90	3.90000	17.50000

Table 4.1: Instron UTM stress analysis data of sample A

Figure 4.2: Instron UTM plot of flexure stress vs flexure strain for sample B.

	Maximum Load (N)	Flex Modulus (MPa)	Flexure stress at Maximum Flexure load (MPa)	Thickness (mm)	Width (mm)
1	364.92	5065.00	131.61	3.90000	17.50000
Mean	364.92	5065.00	131.61	3.90000	17.50000
Standard Deviation	*****	*****	*****	*****	*****
Minimum	364.92	5065.00	131.61	3.90000	17.50000
Maximum	364.92	5065.00	131.61	3.90000	17.50000

XTable 4.2: Instron UTM stress analysis data of sample B

Figure 4.3: Instron UTM plot of flexure stress vs flexure strain for sample C

	Maximum Load (N)	Flex Modulus (MPa)	Flexure stress at Maximum Flexure load (MPa)	Thickness (mm)	Width (mm)
1	445.08	6770.63	160.52	3.90000	17.50000
Mean	445.08	6770.63	160.52	3.90000	17.50000
Standard Deviation	*****	*****	*****	*****	*****
Minimum	445.08	6770.63	160.52	3.90000	17.50000
Maximum	445.08	6770.63	160.52	3.90000	17.50000

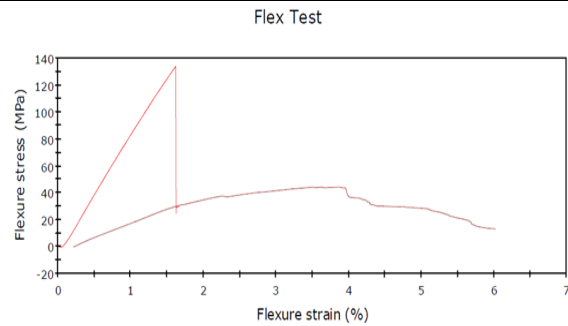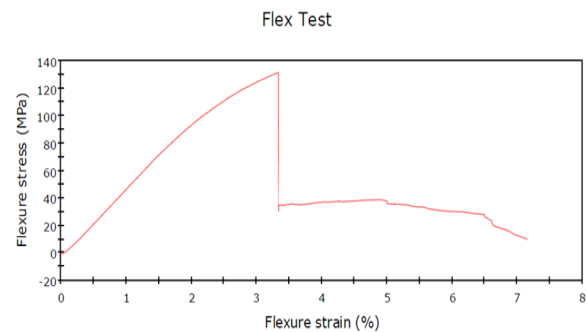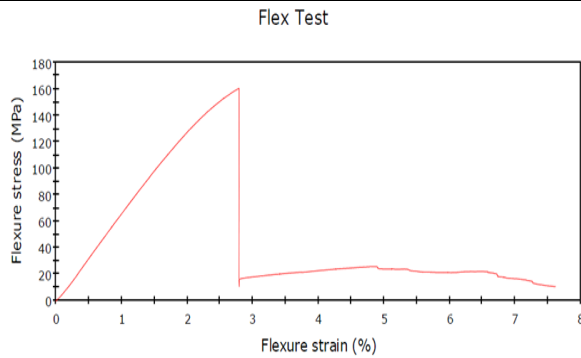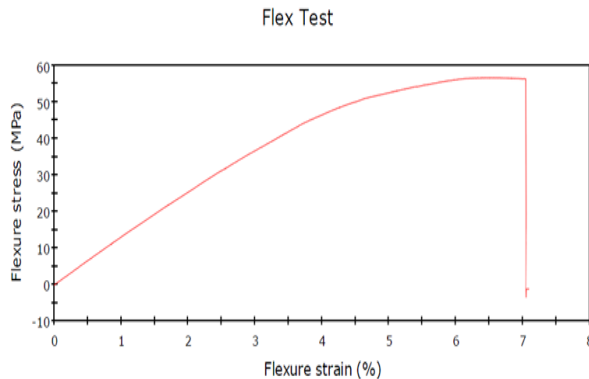Table 4.3: Instron UTM stress analysis data of sample C

Figure 4.4: Instron UTM plot of flexure stress vs flexure strain for sample D

	Maximum Load (N)	Flex Modulus (MPa)	Flexure stress at Maximum Flexure load (MPa)	Thickness (mm)	Width (mm)
1	157.30	1304.06	56.73	3.90000	17.50000
Mean	157.30	1304.06	56.73	3.90000	17.50000
Standard Deviation	*****	*****	*****	*****	*****
Minimum	157.30	1304.06	56.73	3.90000	17.50000
Maximum	157.30	1304.06	56.73	3.90000	17.50000

Table 4.4: Instron UTM stress analysis data of sample D

Composite	E1	E2=E3	G12=G13	G23	NU12=NU13	NU23
Polyester-E-Glass	14.024	4.508	2.050	1.931	0.245	0.165

Table 4.5: Mechanical Properties Obtained fromCADEC

E1=Young's Modulus in X-direction (GPa)
E2=Young's Modulus in Y-direction (GPa)
E3=Young's Modulus in Z-direction (GPa)
G12=Shear Modulus in XY plane (GPa)
G23=Shear Modulus in YZ plane (GPa)
G13=Shear Modulus in XZ plane (GPa)
NU12=Poisson's Ratio in XY plane
NU23=Poisson's Ratio in YZ plane
NU13=Poisson's Ratio in XZ plane

Composite	Von Mises Stress(MPa)	XY Shear Stress (MPa)	YZ Shear Stress (MPa)	XZ Shear Stress (MPa)
Polyester-E-Glass	110.21	62.882	23.714	6.348

Table 4.6:Stress analysis results of ANSYS.

Specimen	Flexural Strength(MPa) (at max. load)	Flexural Modulus(MPa) (at max. load)	Maximum Load, N (at point of fracture)
Specimen A	133.90	9173.57	371.27
Specimen B	131.61	5065.00	364.92
Specimen C	160.52	6770.63	445.08

Table 4.7: Summary of Stress analysis results obtained by Instron UTM machine

V. CONCLUSION

Test specimens were subjected to standard flexural 3 point bending load using instron testing machine. Loading is of vertical type, in between the span length. The average flexural strength of all three readings of each specimen is considered in order to obtain the most correct value of the flexural strength. The flexural strength of E-glass-fibre reinforced Polyester matrix composite was observed to be around

~143 MPa. The values obtained for the flexural stress obtained from testing the specimen in machine and ANSYS differs by 10-12 MPa due to following shortcomings. In fabrication of specimen by hand layup method, it is impossible to remove voids and cracks inside specimen. Raw materials obtained were not of standard quality. Shortcoming in ANSYS model may be because of no provision for feeding matrix-Fiber bonding for the considered SHELL 91 element. Exact environment setup is not possible to simulate in ANSYS.

REFERENCES

[1] NicolaeTaranu, Gabriel Oprisan, Mihai Budescu, AlexandruSecu, IonelGosav, "The use of glass fibre reinforced polymer composites as reinforcement for tubular concrete poles," Proceedings of the 11th WSEAS International Conference on Sustainability in Science Engineering.

[2] Anne Jungert, "Damage Detection in Wind Turbine Blades using two Different Acoustic Techniques,"NDT.net-The e-Journal of Nondestructive Testing ,December 2008.

[3] Sprint-Digital-Druck,Stuttgart, "FRP Reinforcement in RC Structures," fib bulletin 40th International Federation for Structural Concrete.

[4] VolneiTita, Jonas de Carvalho, Dirk Vandepitte, "Failure analysis of low velocity impact on thin composite laminates Experimental and numerical approaches, "Composite Structures 83, (2008), 413–428.

[5] Cairns DS, Lagace PA, "A consistent engineering methodology for the treatment of impact in composite materials," Compos 1992; 11(4):395–412.

[6] Leissa AW, "A review of recent developments in laminated composite plate buckling analysis". Comp Mat Tech ASME Petrol Div 1992;45:1–7.

[7] Seong Sik Cheon, Tae Seong Lim, Dai Gil Lee, "Impact energy absorption characteristics of glass-fibre hybrid composites," Elsiever,Composite Structures 46 (1999) 267-278.

[8] Piggott MR, "Why interface testing by single fibre may be misleading," Comp Sci and Tech 1997;57:965-974.

[9] Harding J, Welsh LM. A tensile testing technique for fibre reinforced composites at impact rates of strain. J Mater Sci 1983;18: 810-826.

[10] Lee DG, Kim KS, Kwak YK, "Manufacturing of a SCARA type direct-drive robot with graphite fibre epoxy composite materials," Robotica, 1991, 9:219-229.

OPTIMIZATION OF PROCESS PARAMETERS IN SINGLE POINT INCREMENTAL FORMING OF AA 6063-O ALLOY

G. Vigneshwaran[1], V.S. Senthil Kumar[2], S.P. Shanmuganatan[3]

[1]PG student, [2]Associate professor, College of engineering, Guindy, Anna University,

[3]Associate professor, S.A.Engineering College

Abstract— Incremental forming is a special technique that offers flexibility and cost-effectiveness in the metal forming process, requiring no high capacity presses or set of dies, thus meeting the ever increasing demand for low volume production and rapid prototyping. In this paper, the effect of process parameters such as feed rate, spindle speed, step size and tool diameter on wall angle was investigated. Aluminum sheet of grade Al 6063-O with 1 mm thickness is used as a work piece. Here an L9 (34) orthogonal array is used to plan the experiments and analyze the results. Experimental results were tested by analysis of variance (ANOVA) technique. The results indicated that a maximum wall angle of 55^0 can be achieved through the incremental forming. The forming limit diagram is also drawn for incremental forming.

Index Terms—Incremental forming, Design of experiment, Optimization, AA 6063**.**

I. INTRODUCTION

Traditionally a sheet-metal component is manufactured by using dies and punches. Because of the high cost of dies and punches, the traditional manufacturing method is adequate only for mass production. The production of customized products, the increasing demand of process flexibility and the necessity to reduce the time to market the products are probably the most significant requirements nowadays. For these reasons, the industrial applications have to be economically justified with a large volume production. Further, stamping cannot fully satisfy the demand of flexibility. These considerations clearly show that the current metal stamping processes may maintain a relevant role in the modern production routings only if cheaper and more flexible technologies are developed. Hence, in the last few years, incremental forming has been introduced as an alternative to the money consuming stamping technology. Here, the final component shape is achieved by the relative movement of a rotational hemispherical tool which follows computer generated tool paths with respect to the blank, without using any dedicated dies to achieve the shape. Its flexibility and low-cost tooling render SPIF more economical than spinning, which was considered as an economical process to produce axisymmetric components in small batches.

Several studies have been carried out on the

formability in Single Point Incremental Forming (SPIF). Leszak patented a process of incrementally deforming a sheet [1]. Kim and Park investigated the effect of some process parameters on the formability of an aluminum sheet [2]. Shanmuganatan et al. performed finite element and experimental analyses on profile forming of conical component and found the thinning variation of the component [3]-[4]. Ham and Jeswiet showed the methodology for developing Forming Limit Diagram for SPIF [5]-[6]. Hussain et al. suggested a novel method to test the thinning limits of sheet metals in negative incremental forming. He also studied the effect of the curvature of a part's generatrix on the formability of an aluminum sheet [7]-[8] Strano et al. also describe the effect on formability of various process parameters [9]. Ambrogio et al. proposed an integrated numerical/experimental procedure in order to limit the shape defects between the obtained geometry and the desired one. He also investigated the influence of the process parameters on accuracy through a reliable statistical analysis [10]-[11]. Myoung- Sup Shim et al. studied the formability of aluminum sheet by imposing different tool paths and found the forming limit curve [12]. Durante et al. evaluated the influence of tool rotation, both in terms of speed and direction of rotation [13].

The movement of the SPIF tool over the surface of the sheet causes a highly localized deformation. SPIF results in higher metal formability, when compared to conventional forming process. The following basic assumptions have been made during the modeling of the SPIF process:

a. The material is isotropic and elastic strains are neglected.

b. The periphery of the sheet is rigidly clamped.

c. Homogeneous deformation exists throughout the process.

II. EXPERIMENTAL DETAILS

The basic concept of the single point incremental forming process is to obtain the desired shape of the product of the relative movement of a simple hemispherical tool in relation to the sheet blank, without the use of dies.

Table 1. Chemical composition of AA6063 (in weight %)

Si	0.483	Mn	0.063
Pb	0.017	Zn	0.114
Fe	0.353	Mg	0.690
Cu	0.075	Cr	0.012
Ni	0.072	Al	Bal

Fig. 1.a Truncated cone to be formed
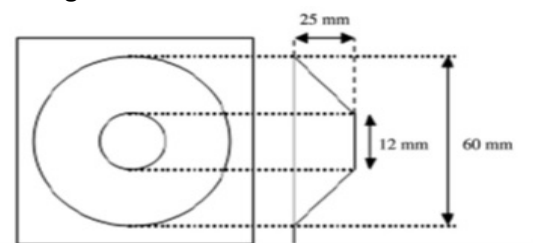
Fig. 1.b Dimensions of the truncated cone

Table 2. Process parameters and their levels

Factor	Process parameter	Unit	Levels		
			1	**2**	**3**
A	Feed rate	mm/min	1000	1500	2000
B	Spindle speed	rpm	2000	3500	5000
C	Step size	mm	0.2	0.5	0.8
D	Tool diameter	mm	5	10	15

In this process, a layer of constant depth in axial direction is formed by an in-plane movement of the tool. On completion of each

layer, the tool moves down with a small increment along the axis, to process the subsequent layers till the completion of the process.

The single point incremental forming is carried out on a three axes CNC vertical milling machine. The material used in this study was an Aluminium alloy, AA 6063- O sheet 200 mm in length, 200 mm in width and 1 mm in thickness. The chemical compositions are listed in Table 1.

Hemispherical head tools of three sizes were used: 5, 10 and 15 mm in diameter were made of H13 tool steel and were hardened up to 60 HRC. The truncated cone, which is taken as a model for study as shown in Fig. 1.a and 1.b is thus, generated using this process. It has been stated that the tool diameter, spindle speed, feed rate step size, forming angle, sheet thickness and shape of the component are the main factors that affect the wall angle of SPIF. In this present work, the tool diameter, spindle speed, feed rate and step size were considered to be variables in the optimization of SPIF process.

Trial experiments were performed to identify the working range of the selected parameters. The feasible limits of these parameters are determined on the basis that no defects are formed in the components during SPIF. The parameters and its levels are shown in table 2.

A coordinate measuring machine is used to measure the wall angle at 22 mm depth of the profile from the clamping section.

III. RESULTS AND DISCUSSIONS

3.1. *Signal to noise(S/N) ratio*

Taguchi's method uses the Signal to Noise (S/N) ratio in place of the mean value to convert the experimental results in a value for the evaluation characteristic in the optimum setting analysis. Some measurable responses to the analysis output during the operation of any engineering system or process are called performance characteristics [14]. The quality of

the formed cones is investigated by considering the wall angle as the main characteristic feature considered in this investigation describing the quality of the welded joints. In order to find the influence of process parameters on the response, the Signal to Noise ratio and means for each process parameter were calculated. In this current work, the S/N ratio was chosen according to the principle of 'the larger-the better' characteristics, which is shown in equation (1).

$$(S/N)_{HB} = -10\log_{10}\left(\frac{1}{n}\sum_{i=1}^{n}\frac{1}{H_i^2}\right)$$

(1)

Where n is the number of the repetitions and Hi is the value of the wall angle of the test on that trail. The process parameters, experimental wall angle and signal-to-noise (S/N) ratio are given in Table 3.

Table 3. L9 orthogonal array with response

ExpNo	Input Parameters				Wall angle (Response)	S/N ratio
	A	B	C	D		
	mm/min	rpm	mm	mm	Degrees (0)	Db
1	1000	2000	0.2	5	55	34.8073
2	1000	3500	0.5	10	52	34.3201
3	1000	5000	0.8	15	46	33.2552
4	1500	2000	0.5	15	43	32.6694
5	1500	3500	0.8	5	46	33.2552
6	1500	5000	0.2	10	52	34.3201
7	2000	2000	0.8	10	43	32.6694
8	2000	3500	0.2	15	51	34.1514
9	2000	5000	0.5	5	41	32.2557

Table 4. Mean response table for S/N ratio

Levels	Feed rate	Spindle speed	Step size	Tool diamete

	(mm/min)	(rpm)	(mm)	r (mm)
1	34.13	33.38	34.43	33.44
2	33.41	33.91	33.08	33.77
3	33.03	33.28	33.06	33.36
min-max	1.10	0.63	1.37	0.41
rank	2	3	1	4

Table 5. Mean response table for experimental data

Levels	Feed rate	Spindle speed	Step size	Tool diameter
	(mm/min)	(rpm)	(mm)	(mm)
1	51.00	47.00	52.67	47.33
2	47.00	49.67	45.33	49.00
3	45.00	46.33	45.00	46.67
min-max	6.00	3.33	7.67	2.33
rank	2	3	1	4

The mean response of S/N ratio and experimental data for each level of the process parameter are given in table 4 and table 5.

3.2. *Analysis Of Variance*

Analysis of variance (ANOVA) test was performed to identify the statistically significant process parameters [15]. This analysis was carried out for a level of significance of 5 %, i.e. for 95% confidence level. The ANOVA results of S/N ratio and the means (both initial and final) for wall angle are given in Table 6, Table 7, Table 8 and Table 9 respectively. The frequency test (F-test) is utilized in statistics to analyze the significant effects of the parameters, which form the quality characteristics.

Since the error is zero in table 6 and table 8, the significant factors cannot be found out. Hence, the minimum contributed factor's sum of squares can be pooled into error term i.e. sum of squares of tool diameter is pooled into error term in table 7 and table 9, and F-test is conducted.

Since $F_{0.05,2,8}$ =4. 46, factors A and C are only significant at the 5 % level of significance from table 7 and table 9.

Table 6. ANOVA (initial) of S/N ratio of wall angle

Factor	Process Parameters	Sum of squares	Degrees of freedom	Mean sum of squares	F-test
A	Feed rate	1.87388	2	0.93694	-
B	Spindle speed	0.68794	2	0.34397	-
C	Step size	3.67516	2	1.83758	-
D	Tool diameter	0.28481	2	0.14240	
Error (pure)		-	-	-	
Total		6.52179	8		

Table 7. ANOVA (final) of S/N ratio of wall angle

Factor	Process Parameters	Sum of squares	Degrees of freedom	Mean sum of squares	F-test
A	Feed rate	1.87388	2	0.93694	6.57
B	Spindle speed	0.68794	2	0.34397	2.41
C	Step size	3.67516	2	1.83758	12.90
Error (Pooled)		0.28481	2	0.14240	
Total		6.52179	8		

Table 8. ANOVA (initial) of means for wall angle

Factor	Process Parameters	Sum of squares	Degrees of freedom	Mean sum of squares	F-test
A	Feed rate	56.000	2	28.000	-
B	Spindle speed	18.667	2	9.333	-
C	Step size	112.667	2	56.333	-
D	Tool diameter	8.667	2	4.333	-
Error (pure)		-	-	-	
Total		196.000	8		

Table 9. ANOVA (final) of means for wall angle

Factor	Process Parameters	Sum of squares	Degrees of freedom	Mean sum of squares	F-test
A	Feed rate	56.000	2	28.000	6.46
B	Spindle speed	18.667	2	9.333	2.15
C	Step size	112.667	2	56.333	13.00
Error (pooled)		8.667	2	4.333	
Total		196.000	8		

Table 10. Percentage Contribution of Process Parameters

Process Parameters	Feed rate mm/min	Spindle speed rpm	Step size mm	Tool diameter mm
% Contribution	29	10	57	4

FORMING LIMIT DIAGRAM

Fig. 3 Forming limit diagram
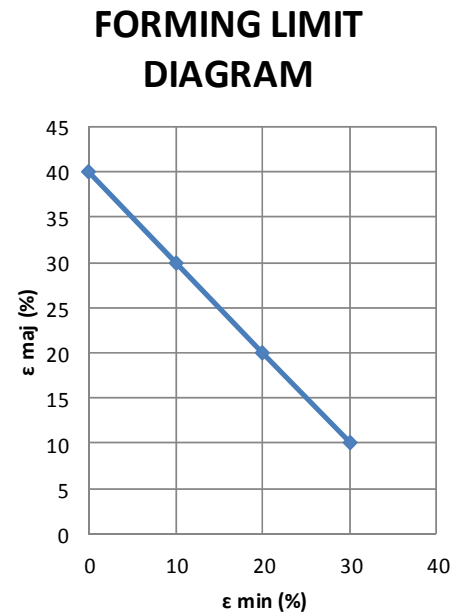

Fig.2.a Main effects plot for S/N ratio

Fig.2.b Main effects plot for wall angle

The portion of the total variation observed in an experiment attributed to each significant factor and/or interaction is reflected in the percentage of contribution. The percentage of contribution is a function of the sum of squares for each significant item. It indicates the relative power of a factor and/or interaction to reduce the variation. If the factor and/or interaction levels are controlled precisely, then the total variation could be reduced by the amount of the percentage of contribution. The percentage of the contribution of the tool pin profile, transverse speed and welding speed is shown in table 10.
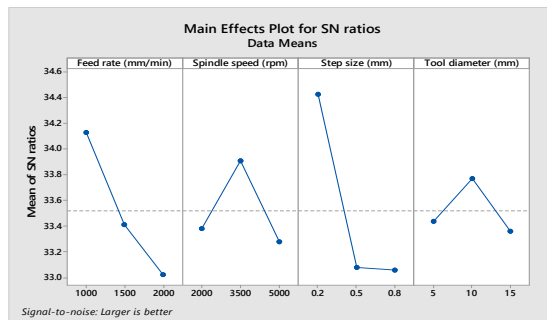
3.3. *Determination of optimum factor level combination*
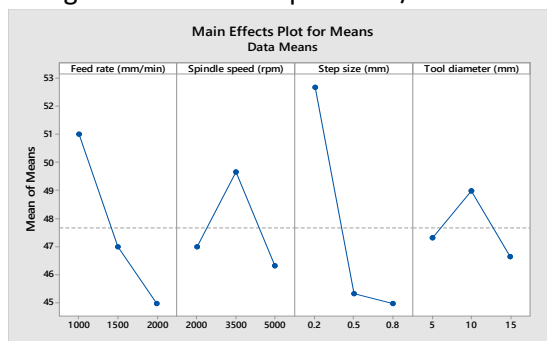
Fig 2. Shows four graphs, each of which represent the mean response and the mean S/N ratio for the feed rate, spindle speed, step size and tool diameter. The values of the graphs have been tabulated in Table 4 and Table 5. Based on the highest values of the S/N ratio and mean values (Fig 2.a and 2.b), the

overall optimum process parameters for wall angle are A1, B2, C1 and D2.

After the optimum level has been selected, one could predict the optimum wall angle using the following equation [16] which is shown in equation (2).

$$W_{predicted} = W_m + \sum_{i=1}^{n}(W_0 - W_m) \quad (1)$$

W_m is the mean response or the mean S/N ratio, W0 is the mean response or mean S/N ratio at optimal levels and n is the number of main design parameters that affect the quality characteristics. Substituting the values in Equation 2, the predicted wall angle value is 56^0. The highest wall angle achieved was 55^0 which was within the confidence limit.

The forming limit diagram is drawn for incremental forming of AA 6063-O alloy which is shown in Fig. 3. Here the graph is plotted with minor strain percentage (ε_{min} (%)) as x-axis and major strain percentage (ε_{maj} (%)) as y-axis. The graph obtained here is a straight line which is different from conventional forming processes. The region below the straight line is safe region and the region above it is unsafe region.

IV. CONCLUSION

In this investigation, AA 6063-O alloys were successfully formed incrementally. The results can be summarized as follows:

• The L9 Taguchi orthogonal designed experiments of SPIF of AA6063-O were successfully conducted.

• The percentage of contribution of SPIF process parameters was evaluated. It is found that the feed rate, spindle speed, step size and tool diameter contributes 29%, 10%, 57% and 4% respectively

• Feed rate of 1000 mm/min, spindle speed of 3500 rpm, Step size of 0.2 mm and tool diameter 10 mm provides higher wall angle.

• It was observed that the experimental results were close to the predicted values and they are falling within the confidence limits.

• The forming limit curve in SPIF is different from that in other conventional forming processes. It appears to be a straight line with a negative slope in the positive region of the minor strain in the forming limit diagram.

REFERENCES (2)

[1] Leszak E. Apparatus and process for incremental dieless forming. Patent US3342051A; 1967.

[2] Y.H. Kim, J.J. Park. "Effect of process parameters on formability in incremental forming of sheet metal". Journal of Materials Processing Technology, vol. 130-131, pp. 42–46, 2002.

[3] S.P. Shanmuganatan, V.S. Senthil Kumar. "Metallurgical analysis and finite element modelling for thinning characteristics of profile forming on circular cup". Materials and Design, vol. 44, pp. 208–215, 2013.

[4] S.P. Shanmuganatan, V.S. Senthil Kumar. "Experimental investigation and finite element modeling on profile forming of conical component using Al 3003(O) alloy". Materials and Design, vol. 36: 564–569, 2012.

[5] M. Ham & J. Jeswiet. "Single Point Incremental Forming and the Forming Criteria for AA3003". Annals of the CIRP, Vol. 55/1, pp. 1-4, 2006.

[6] M. Ham and J. Jeswiet. "Forming Limit Curves in Single Point Incremental Forming".Annals of the CIRP, Vol. 56/1, pp. 277-280, 2007.

[7] G. Hussain, L. Gao. "A novel method to test the thinning limits of sheet metals in negative incremental forming". International Journal of Machine Tools & Manufacture, vol. 47, pp. 419–435, 2007

[8] G. Hussain, L. Gao, N. Hayat, L. Qijian. "The effect of variation in the curvature of part on the formability in incremental forming: An experimental investigation". International Journal of Machine Tools & Manufacture, vol. 47, pp. 2177–2181, 2007.

DESIGN AND FABRICATION OF MULTI PURPOSE AGRICULTURAL EQUIPMENT

[1]R Jaffar Sadiq, [2]Dr.S.G.Gopala krishna, [3]Dr.N.G.S.Udupa

[1,2,3] NCET.Banglore

Abstract— A Study has been carried out to develop multi purpose agricultural equipment, for performing major agricultural operations like goods carrying, pesticide spraying, laddering, inter-cultivating and digging operations of sandy loam deep soils, to increase the efficiency and reduce the production and handling cost. Modifications were carried out, and the modification includes fabricating a vehicle which is small, compact in size which can move easily across the fields. This vehicle was named as NCET kissan all in one .which consists of various agricultural implements like inter-cultivator, ladder, pesticides sprayer, goods carrying container, plough, which can be easily assembled and Dis –assembled by a single person, the cost of equipment is less by 83% compared to a tractor. And 40% compared to a tiller (price in India).

NCET kissan all in one-agricultural equipment name

I. INTRODUCTION

Metal fabrication is the building of metal structures by cutting, bending, and assembling processes

- Cutting is done by sawing, shearing, or chiseling (all with manual and powered

- variants); torching with hand-held torches (such as oxy-fuel torches or plasma torches); and via numerical control (CNC) cutters (using a laser, mill bits, torch, or water jet).

- Bending is done by hammering (manual or powered) or via press brakes and similar tools. Modern metal fabricators utilize press brakes to either coin or air-bend metal sheet into form. CNC-controlled back gauges utilize hard stops to position cut parts in order to place bend lines in the correct position. Off-line programming software now makes programming the CNC-controlled press brakes seamless and very efficient.

- Assembling (joining of the pieces) is done by welding, binding with adhesives, riveting, threaded fasteners, or even yet more bending in the form of a crimped seam. Structural steel and sheet metal are the usual starting materials for fabrication, along with the welding wire, flux, and fasteners that will join the cut pieces. As with other manufacturing processes, both human labor and automation are commonly used. The product resulting from fabrication may be called a fabrication. Shops that specialize in this type of metal work are called fab shops. The end products of other common types of metalworking, such as machining, metal

stamping, forging, and casting, may be similar in shape and function, but those processes are not classified as fabrication.

- Blacksmithing has always involved fabrication, although it was not always called by that name.

- The products produced by welders, which are often referred to as weldments, are an example of fabrication.

  Similarly, millwrights originally specialized in setting up grain mills and saw mills, but today they may be called upon for a broad range of fabrication work.

- Ironworkers, also known as steel erectors, also engage in fabrication. Often the fabrications for structural work begin as prefabricated segments in a fab shop, then are moved to the site by truck, rail, or barge, and finally are installed by erectors.

II.Technical Specification of NCET kissan all in one

TECHNICAL SPECIFICATION	
ENGINE	
TYPE	4 STROKES 150CC WATER-COOLED
DISPLACEMENT RATIO	149CC
COMPRESSION RATIO	11:01
MAX. POWER	8.5KW / 8000R / MIN
MAX. TORQUE	10N.M / 7500R / MIN
CLUTCH	
TYPE	MULTI-PLATE WET TYPE
LUBRICATION METHOD	
PRESSURE SPLASH	
TRANSMISSION	
TYPE	CONSTANT MESH TYPE
NO. OF GEARS	5 FORWARD + 1 REVERSE

Table 1 back engine used in NCET kissan all in one

Table 1 shows the details of rear engine used in NECT   kissan all in one and multi-purpose agricultural equipment, the engine used was built by Bajaj Company and model was given by auto rickshaw re

III.Table 2 technical specification of NCET kissan all in one

ENGINE	
TYPE	2 STROKE
COOLING TYPE	FORCED AIR COOLED
DISPLACEMENT	145.45 CC
MAX POWER	7 BHP(5.15 KW) 5000 RPM
MAX TORQUE	12.1 NM @ 3500 RPM
IGNITION TYPE	CDI
TRANSMISSION TYPE	4 FORWARD AND ONE REVERSE
CLUTCH TYPE	WET MULTIDISC TYPE
ELECTRICAL SYSTEM	
SYSTEM	12V AC + DC
HEAD LIGHT	35/35W
HORN	12 V AC
SUSPENSION	
FRONT SUSPENSION	HELICAL SPRING AND HYDRAULIC SHOCK ABSORBER WITH ANTIDIVE LINK
REAR SUSPENSION	INDEPENDENT SUSPENSION WITH SPRING AND HYDRAULIC SHOCK ABSORBER
TYRES	
FRONT TYRE SIZE	4.00-8, 4PR
REAR TYRE SIZE	4.00-8, 4PR 2 NOS.
FRONT BRAKES	DRUM HYDRAULIC
REAR BRAKES	DRUM HYDRAULIC

Table 2 technical specification of NCET kissan all in one
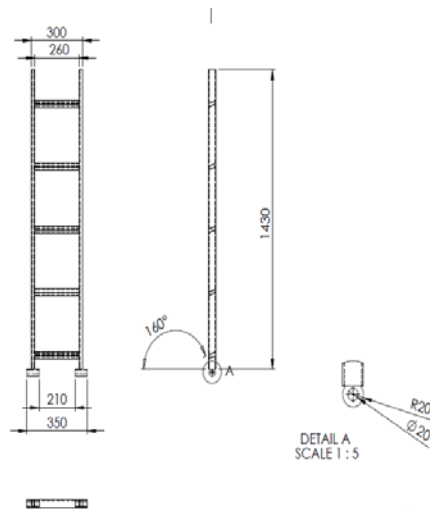

Table 2 shows the details of front engine used in NECT kiss an all in one a multi-purpose agricultural equipment, the engine used was built by Bajaj auto rickshaw Re Company and model was given by electronic start. It also gives a detailed description of over all length, type of electrical system used, type of transmission system used etc; the resemblance of NCET kissan all in one is all most similar to the Bajaj two stroke front engine auto rickshaws.
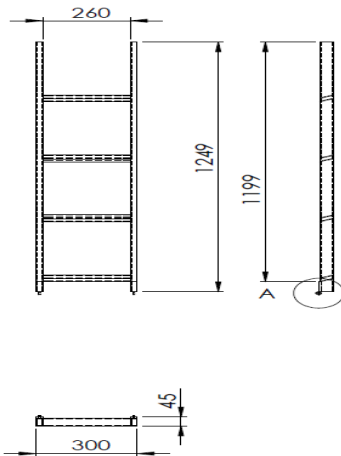
Iv.Ladder
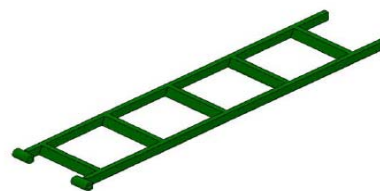
**Fig 1 first part of ladder**

The ladder has been divided in to three parts, and hence named as 1,2,3 parts where in which the first part is been fixed to vehicle chassis with the help of 14 mm bolts and nuts the one end of the ladder is been welded by the help bush so that the it can be easily tilted from 90^0

to 180^0 the dimensions has been shown in the figure 5.5 .

Fig 2 second part of ladder

      The second part of the ladder rests on the main frame of good carrying container this part of ladder is attached to the first part of ladder by means of Lowry inches so that it can be tilted easily and proper clamping mechanism is also been used to lock it when it is placed one on the other the required dimensions is shown in the figure 2
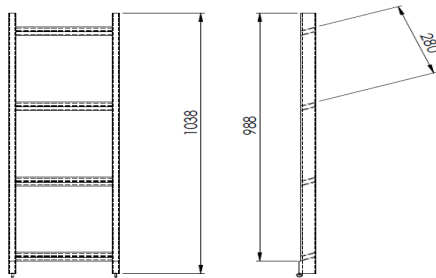

Fig 3 third part of ladder

The third part of the ladder is free to rests on the main frame of good carrying container this

part of ladder is attached to the second part of ladder by means of Lowry inches so that it can be tilted easily and proper clamping mechanism is also been used to lock it when it is placed one on the other the required dimensions is shown in the figure 3

V.Ploughing assembly.
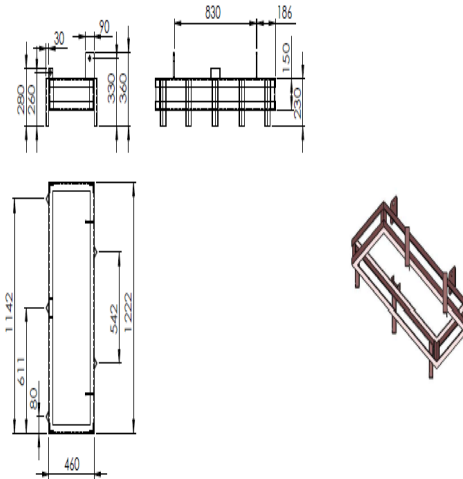
Fig 4 main frame of ploughing assembly

      Fig shows the main frame of ploughing assembly where the blades can be accommodated, the total numbers of blades that can accommodate are 5 blades which are in zigzag form, and it is placed so that when they perform their job they dig the soil in straight line format. It is also been attached by to plates consisting of holes so that they can be easily attached to the vehicle by means of shaft and lock them by using clipping mechanism.
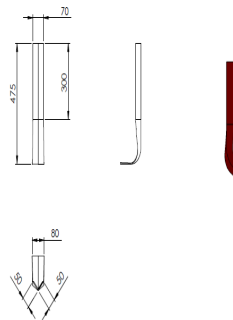

Fig 5 blades used in ploughing assembly

Figure shows the blades which are used in ploughing assembly these are manufactured by using cast iron and process of manufacturing is by forging. for analysis purpose the load coming on to the plates is difficult to assume it is totally dependent on type of soil, hence the soil changes from one part of land over the other part hence it is assumed and 90 kg's of load was putted on each blades and it is proved to safe when tested in fem analysis.
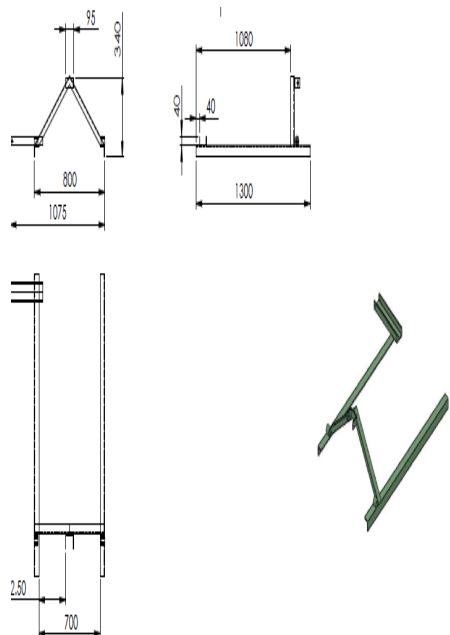
VI. Engine mounting
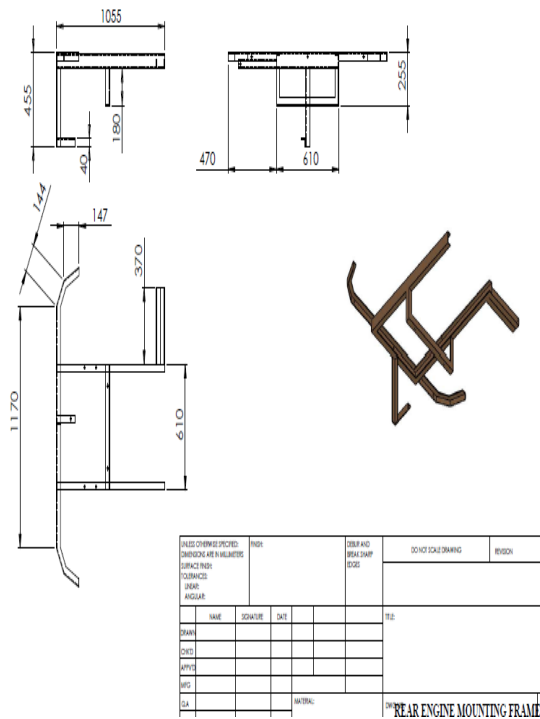
Fig 6 rear engine mounting frame

Figure shows the rear engine mounting frame which has welded at the rear part NCET kissan all in one agricultural equipment the fuel tank and exhaust manifolds are also been placed at appropriate positions.

VIII. Extended chassis

Fig 7 extension chassis frame

The above figure shows the extension part of the chassis which is drawn from main part of the chassis this is provided to mount the goods carrying container ,pesticides spraying pump, ladder and rear engine

VII. Goods carrying container
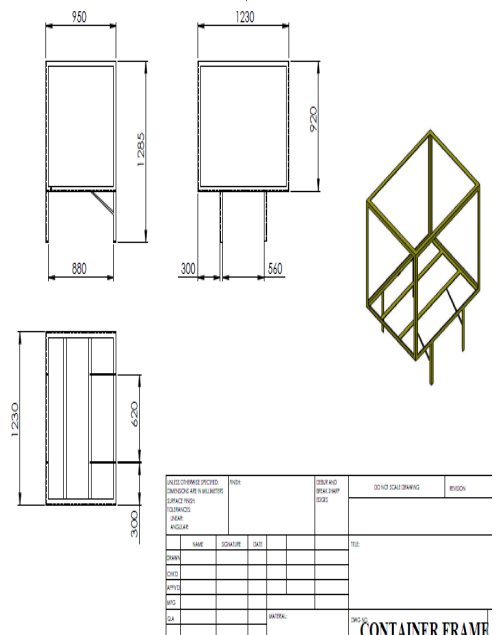
Fig 8 goods carrying container frame

The goods carrying container is attached to the rear part of the NCET kissan all in one the it consists of two doors on its front part, the entire container can be tilted and rotated from

900 to 1800 .and there is a provision of remove entire assembly by means of bolts and nuts.

IX. Goods carrying container mounting

Fig 9, goods carrying container mounting frame
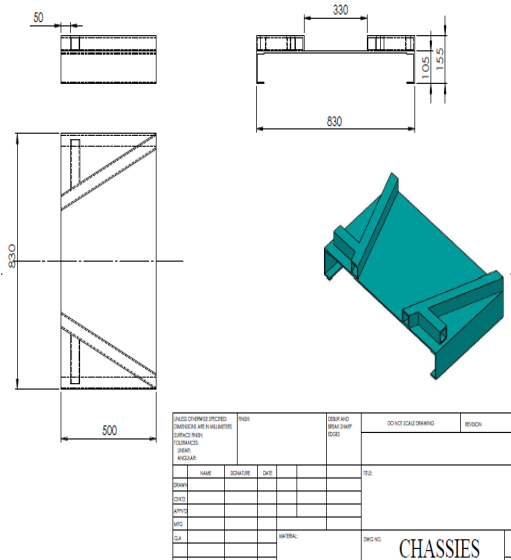
The goods carrying container is attached to chassis by means of mounting frame, this frame also covers the front engine and this is responsible for connecting and takes the loads from shock absorber.

X. Cabin
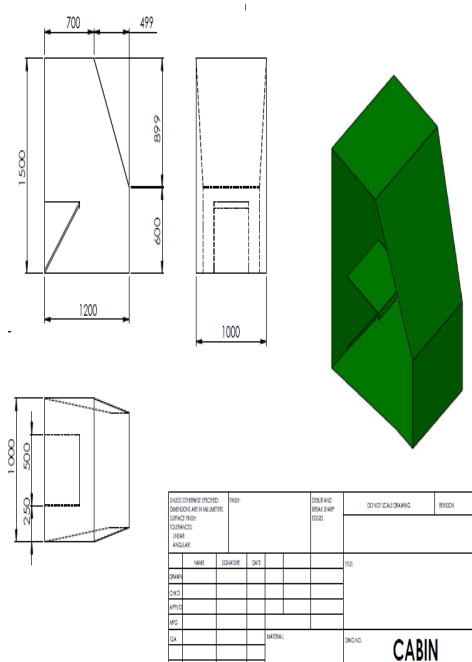
Fig 10 Cabin frame

This is used to safe guard the driver it is made up of mild steel sheet and it is the place where are controls of vehicle which guide the stability of vehicle is placed.

XI. Inter cultivator blades
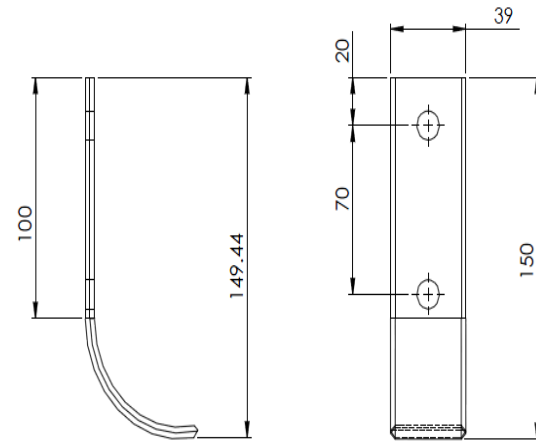
Fig 11 Inter cultivator blades

These blades are also called as tins, the total number of blades used are in two ways 16 blades and 8 blades depending on the type of soils the user can select among these two any one .the drive to this blades are given by an rear engine which can be controlled from driver cabin it self, 4 gears are provided to vary the speed and load carrying capacity.

XII.Pesticide spraying pump

Fig 11 pesticides spraying pump used in NCET kissan all in one.

Specifications

PLUNGER NO.*DIA*STROKE	2 PLUNGERS*Φ30MM*20
PRESSURE	21-45KG/CM²
OUTPUT	35-45L/MIN
SPEED	800-1200 R.P.M
DIMENSION	420MM×320MM×340MM
POWER	5-6.5 PS

Table 3 shows the technical specification of pesticides spraying pump NCET kissan all in one

XIII.Photos

XIV.Conclusion

NCET kissan all in one, multipurpose agricultural equipment, can be successfully used for farming due to following reasons

1. Faster operations
2. Low cost of operations and low investments
3. Light in weight, low cost durable with minimum repairs which saves time during operations
4. All cultural operations (inter-cultivating, ploughing, laddering goods carrying etc)for year round cultivation done with the help of NCET kissan all in one
5. Slipping of tires was very common problem when moisture content was more, Hence farming is recommended to be done in 10-15 percent moisture content lands.
6. Ladder can be tilted from 90^0 to 200^0 ,but best load withstanding range was noticed at 120^0.position of ladder
7. Ploughing was difficult to be done in newly cultivating farms. But it is recommended to use once after cultivating it from the tractor.
8. Maximum of 800 kg's load can be pulled, but it is recommended for carrying 500 kg's of load for better life span of engine
9. From the survey , farmers told that they use tractor minimum of 4 times and maximum of 7 times for one crop rotations, for which they were paying 700rs /hector (for one time) hence if farmer goes for one time with tractor is sufficient, else all other work he can do from NCET kissan all in one.

10. The cost of equipment was 120000,which can be still reduced when produced in mass production
11. The maximum speed ranges 40 km/hrs, this is build to take more load rather than speed hence it is adequate to run the vehicle at 25 km/hr to commutate both time and durability.

XV. REFERENCES

[1] D.L.PETERSON, H.W.HOGMIRE "Tunnel sprayer for dwarf fruit trees" , 1994 American society of agricultural engineers ,Vol,37(3):709-715

[2] V.K CHANDEGARA "design and developing of bullock drawn multi-purpose implement for sandy loam soil", Journal of agricultural engineering, Vol, 40(4): October December, 2003

[3] OMOTADE SEGUN ADEDEJI AND F.N.AJUEBOR "performance evaluation of motorized groundnut Sheller", Journal of agricultural engineering, Vol, 39(2): April June, 2002

[4] AHMAD MOHSENIMANESH "Modeling of pneumatic tractor tyre interaction with multi-layered soil", science direct Bio systems engineering 104(2009)191-198
A.TORREGROSA, E.ORTI, B.MARTIN And C.ORTIZ "Mechanical harvesting of oranges and mandarins in Spain", science direct Bio systems engineering 104(2009)18-24

[5] J.S MAHA, A.S BAL and G.S MANES "Performance evaluation of commercial sunflower threshers and their role in Punjab", Journal of agricultural engineering, Vol, 40(1): January. March, 2003

[6] M.DURAN, J.PUIG, G.ARBAT, J.BARRAGAN, F.RAMIREZ"Performance and backwashing efficiency of disc and screen filters in micro irrigation systems", science direct Bio systems engineering 103(2009)35-42

[7] GLUSEPPE ZIMBALATTI, ANDREA R.PROTO "Cable logging opportunities for firewood in Calabria forests" Bio systems Engineering 102 (2009) 63-68

[8] ERGON DOGAN, HALIL LIRNAK, ZEKI DOGAN " Effect of varying the distance of collectors below a sprinkler head and travel speed on measurements of mean water depth and uniformity for a linear move irrigation sprinkler system" Bio system Engineering 99 (2008) 190 -195

[9] V.K. TEWARI, K.N.DEWANGAN "Effect of vibration isolators in reduction of work stress during field operation of hand tractor" Biosysytems Engineering 103 (2009) 146-158

MECHANICAL BEHAVIOUR OF GROUNDNUT SHELL POWDER/ CALCIUM CARBONATE /VINYL ESTER COMPOSITE

R. Pragatheeswaran[1], S. Senthil Kumaran[2]

[1]PG Student, [2]Associate professor, College of Engineering, Guindy, Anna University

Abstract— In recent years, natural fiber along with mineral fillers is used to fabricate hybrid composite which shows improved mechanical properties. In this study the effect of calcium carbonate on the mechanical properties of groundnut shell powder based composite was investigated. To meet this objective, groundnut shell powder(GNP) and calcium carbonate(CC) reinforced vinyl ester(VE) were prepared by hand lay-up process. The effects of calcium carbonate on tensile and flexural properties of the composites were investigated. The test result shows that increase in calcium carbonate increases the tensile and flexural properties of composites.

Index Terms— Groundnut shell powder, Calcium Carbonate, Vinyl ester, Natural Fiber Composite

I. INTRODUCTION

Natural fibers have become alternative reinforcement for synthetic fibers in polymer composites, due to their advantages like low density, less tool wear during processing, low cost, non-toxic, easy to process, environmental friendly, and biodegradability[1,8].

The natural fiber-containing composites are more environmentally friendly, and are used in various applications like automobiles, aerospace, railway coaches, military applications, building and construction industries and ceiling paneling, partition boards, packaging, consumer products, etc [2].

Several studies have been carried out on the composites made of groundnut, calcium carbonate and vinyl ester

G.C. Onuegbu et al(2013) [3] investigated the mechanical properties of polypropylene composites with ground nut husk powder at different particle sizes and found that the presence of ground nut husk improved the tensile strength, modulus, flexural strength and impact strength of the composites.

Behzad Kord (2011) [4] studied the effect of calcium carbonate as mineral filler on the physical and mechanical properties of wood based composites and found that the mineral filler loading had significant effects on the mechanical properties of wood based composites Vasanta V Cholachagudda et al (2013) [5] found that coir fiber as the major reinforcement and rice husk as an additional fiber improves the mechanical property of polymer composites were prepared by hand lay-up process according to ASTM standards, he also found that there is an increase in tensile and flexural.

II. MATERIALS AND PROCESSING

Lignin binds individual fiber cells together, the

lignin content of groundnut shell fiber is much greater than that of banana, baggase, rice husk, jute, hemp, kenaf and sisal fibers and the hemicellulose influence moisture absorption of composites, the hemicellulose content of groundnut shell is less than rice husk, banana, wood, baggase and kenaf fibers[6]. Groundnut shell treated properly to remove impurities and it crushed to powder. Groundnut shell powder and calcium carbonate are mixed in different composition.

Table.1. shows the Chemical composition of various natural resources [6]

Species	Cellulose (wt%)	Hemi cellulose (wt%)	Lignin (wt%)
Pine (softwood)	40-45	25-30	26-34
Maple (hardwood)	45-50	22-30	22-30
Banana	63-64	19	5
Coir	32-43	0.15-0.25	40-45
Sisal	63-64	12	10-14
Jute	61-71.5	12-20.4	11.8-13
Kenaf	31-39	21.5	15-19
Hemp	70.2-74.4	17.9-22.4	3.7-5.7
Bagasse	40-46	24.5-29	12.5-20
Groundnut shell	**35.7**	**18.7**	**30.2**
Rice husk	31.3	24.3	14.3
Pineapple	81	-	12.7

Table.2. shows the volume and mass fraction of reinforcement and polymer used in the work.

S.No	% of volume fraction			%mass (gram)		Volume (ml)
	GNP	CC	VE	GNP	CC	VE
1	35	0	65	21.546	0	175.5
2	30	5	65	18.468	36.585	175.5
3	25	10	65	15.39	73.17	175.5
4	20	15	65	12.312	109.755	175.5

(1) (2) (3) (4)

Figure.1. Shows the hand lay-up technique
(1) Placing the bottom mould plate with silicon rubber
(2) Adding catalyst, accelerator, promoter to resin
(3) Mixing resin to the fiber
(4) Closing with the top mould plate

The composite fibre is prepared by hand lay-up technique. A mould with the dimension of 300 mm × 300mm × 3mm was used to prepare the composite specimen[7]. Measured quantities of groundnut shell powder, calcium carbonate and vinyl ester resin were taken in a glass beaker and stirred thoroughly to get homogeneous mixture. Methyl Ethyl Ketone Peroxide is used as a catalyst to support the moulding process. Cobalt Naphthenate is used as an accelerator to speed up the reaction[9]. Dimethyl Acetamide is used as promoter to increase adhesion between a polymer and reinforcement. After adding the suitable quantity of resin, catalyst, accelerator and promoter, the mixture was again stirred for 10 minutes and thoroughly mixed mixture was placed in the mould and compressed uniformly. This set up allowed for curing and then the composite specimen was taken out from the mould.

III. CUTTING OF LAMINATES INTO SAMPLES OF DESIRED DIMENSIONS

A Wire Hacksaw blade was used to cut each laminate into smaller pieces, in accordance with ASTM standard.

The tensile test was generally performed on flat composite sample. The length of the test specimen was as per ASTM D638. The dimension of the specimen is 250 mm x 25 mm x 3 mm.

Flexural test is a 3-point bend test, which generally promotes failure by inter-laminar shear. This test is conducted as per ASTM standard D790 using Universal Testing Machine. The dimension of the specimen is 20mm x 150mm x 5mm.

IV. EXPERIMENTAL RESULTS

A. Tensile Test

The tensile strength of a material is the

maximum amount of tensile stress that it can take before failure. The commonly used specimen for tensile test is the flat type. During the test a uniaxial load is applied through both the ends of the specimen. The results are tabulated in the table.3.

B. Flexural Test

Flexural strength is defined as a material's ability to resist deformation under load. It is a 3-point bend test, which generally promotes failure by inter-laminar shear. The results are tabulated in the table.4.

Table.3. shows tensile load of specimen

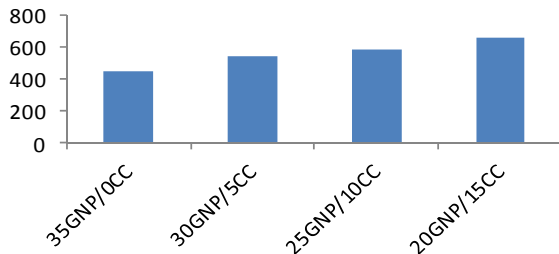| Sample no.	Percentage of volume fraction			Maximum load (N)
	Ground nut powder	Calcium carbonate	Vinyl ester	
1	35	0	65	443
2	30	5	65	535
3	25	10	65	580
4	20	15	65	650

TENSILE LOAD (N)

Figure.2. shows graph of tensile load of specimens

Table.4.shows flexural load of specimen

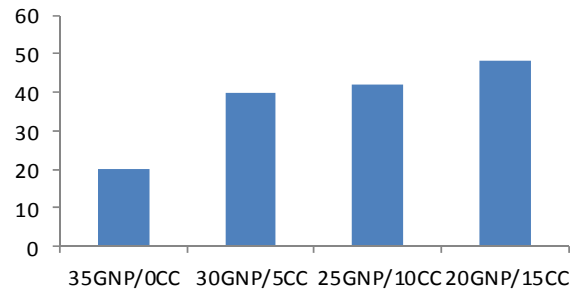| Sample no.	Percentage of volume fraction			Maximum load (N)
	Ground nut powder	Calcium carbonate	Vinyl ester	
1	35	0	65	20
2	30	5	65	40
3	25	10	65	42
4	20	15	65	48

FLEXURAL LOAD(N)

Figure.3.shows graph of flexural load of specimens

V. CONCLUSION

A new class of natural fiber based polymer composites groundnut shell powder and calcium carbonate reinforcement in the vinyl ester polymer is developed.

The experimental investigation on mechanical properties ie Tensile strength and flexural strength, groundnut shell powder/ calcium carbonate /vinyl ester composite ,material is greatly influenced by the groundnut shell powder/ calcium carbonate composition.

The maximum tensile load is obtained for the composite prepared With 20%GNP/15%CC. The tensile load graph (See Figure.2) shows an increase of calcium carbonate volume, increases the tensile load.

The maximum flexural load is obtained for the composite prepared with 20%GNP/15%CC. The flexural load graph (See Figure.3) shows an increase of calcium carbonate volume, increases the flexural load.

REFERENCES

[1] S.V.Joshia, L.T. Drzal, A.K.Mohanty, S.Arorac "Are natural fiber composites environmentally superior to glass fiber reinforced composites?", Composites Part A: Applied Science and Manufacturing, Vol.35(3), pp371-376, 2004

[2] D. Chandramohan,K.Marimuthu "A review on natural fibers", International Journal of

Research and Reviews in Applied Sciences, Vol.8(2),2011

[3] G.C. Onuegbu, S.C. Nwanonenyi, M.U.Obidiegwu "The Effect of Pulverised Ground Nut Husk on Some Mechanical Properties of Polypropylene Composites", International Journal of Engineering Science Invention, Vol.2(6), pp.79-83, 2013.

[4] Behzad Kord "Effect Of Calcium Carbonate As Mineral Filler On The Physical And Mechanical Properties Of Wood Based Composites", World Applied Science Journal, Vol. 13(1) pp 129-132, 2011.

[5] Vasanta V Cholachagudda , Udayakumar.P.A , Ramalingaiah "Mechanical characterisation of coir and rice husk reinforced hybrid polymer composite", International Journal of Innovative Research in Science, Engineering and Technology ,Vol. 2(8),2013.

[6] G. U. Raju, V. N. Gaitonde, S. Kumarappa, "Experimental Study on Optimization of Thermal Properties of Groundnut Shell Particle Reinforced Polymer Composites", International Journal of Emerging Sciences, Vol .2(3), pp 433-454, 2012.

[7] S.Muthukumar, K.Lingadurai "Investigating the mechanical behaviour of coconut shell and groundnut shell reinforced polymer composite", Global Journal Of Engineering Science And Researches, Vol.1(3) pp 2348 – 8034, 2014.

[8] N.P.G. Suardana, Yingjun Piao, Jae Kyoo Lim "Mechanical properties of hemp fibers and hemp/pp composites: effects of chemical surface treatment" Materials Physics and Mechanics , 2011.

[9] Afroz mehar, S.Irfan Sadaq, Sameer Mohammed, "Experimental Study and the Effect of Alkali Treatment with Time on Jute Polyester Composites", International Journal of Engineering Research, Vol.2(2), pp : 23-28, 2013.

SIMULATION OF AIR-STEAM GASIFICATION
OF RICE HUSK USING ASPEN PLUS

[1]Arun K. Mohandas, [2]Rupesh S, [3]C. Muraleedharan, [4]P. Arun

[1,2,3,4]Department of Mechanical Engineering, National Institute of Technology Calicut

Abstract—A thermodynamic equilibrium model for air-steam gasification of rice husk is developed using Aspen Plus (Advanced System for Process Engineering Plus) process simulator. The model is based on Gibbs free energy minimisation and tar formation is incorporated using FORTRAN subroutine. The prediction accuracy of the developed model is determined by comparing the model predicted syngas composition with experimental results and found to be in fair agreement. Effect of key operating parameters on syngas composition, gas yield and first law efficiency is analysed using the developed model .For an equivalence ratio of 0.25, steam to biomass ratio of 1 and temperature of 1000 K, hydrogen mole fraction, first law efficiency and heating value of syngas are found to be 23.78 %, 76.14 % and 5.038 MJ/Nm^3, respectively.

Index Terms—Gasification, equilibrium model, Aspen Plus, syngas.

I. INTRODUCTION

Biomass is one among the most promising renewable energy resources and its utilisation through gasification is in line with the requirements of sustainable development. Biomass gasification is a complex process consisting of different steps, namely drying, pyrolysis, combustion and gasification of pyrolysis products.

Mathematical models have been used extensively to investigate biomass gasification due to high costs and difficulties associated with experimentation.

Among the methods available for modelling gasification, thermodynamic equilibrium model (TEM) is one of the simpler approaches and can be used as a preliminary tool to analyse the effect of feedstock and process parameters on gasification process. Thermodynamic equilibrium modelling can be achieved through two approaches namely, stoichiometric and non-stoichiometric [1]. Non-stoichiometric equilibrium modelling is useful when temperature and pressure are known and reaction stoichiometry is unknown. However non-stoichiometric equilibrium modelling employing Gibbs free energy minimisation is relatively complex. Aspen Plus process simulator [2] provides an easier alternative for simulating non-stoichiometric models.

The Aspen Plus process simulator has been used extensively to simulate several complex processes such as coal conversion and petroleum refining using well written flexible Fortran subroutines [3]. Doherty *et al*. [4] simulated a circulating fluidised bed gasifier using Aspen Plus and studied the effect of preheating of air on gasifier performance and

composition of syngas. Air gasification of olive kernel in a pilot scale bubbling fluidised bed gasifier was simulated by Michailos and Zabaniotou [5] in Aspen Plus by using a combination of two approaches-Gibbs free energy minimisation and reaction kinetics. Mathieu and Dubuisson [6] simulated wood gasification and concluded that air preheating has no significant impact on efficiency beyond a certain critical air temperature. Mansaray *et al.* [7] developed two models to simulate the performance of a dual-distributor-type fluidised bed gasifier where the first model used an overall equilibrium approach, and the hydrodynamic complexities of the reactor were incorporated in the second one. Nikoo*et al.* [8] modelled the reactions taking place in the bed and freeboard of a fluidised bed reactor separately by adopting governing hydrodynamic equations for a bubbling bed and kinetic expressions for the char combustion. Gasification of wood in a downdraft gasifier was simulated by Paviet*et al.* [9] to predict the composition of flaming pyrolysis gas and producer gas. Kumar *et al*. [10] simulated corn stover and distiller grains gasification using Aspen Plus and predicted the flow rate and composition of product gas.

The present work deals with the simulation of air-steam gasification of rice husk in a fluidised bed gasifier using Aspen Plus software, based on Gibbs free energy minimisation.

II. MODELLING APPROACH

A. Assumptions

The following assumptions are made for developing the model:

(i) Gasifier is a steady state system with uniform temperature and pressure throughout.

(ii) The residence time of the gases in the gasifier is high enough to establish thermodynamic and chemical equilibria.

(iii) All the gases behave ideally.

(iv) Gases except H_2, CO, CO_2, CH_4, and N_2 are considered   asdilute.

(v) N_2 is inert in the entire process.

(vi) Biomass is made up of Carbon, Hydrogen and Oxygen.

(vii) Steam is supplied under superheated condition of 1 bar and 300 ^{o}C.

(viii) All elements in biomass except Sulphur take part in the   chemical reactions.

(ix) Tar is modelled as benzene.

B. Aspen Plus Model

The different stages considered in Aspen Plus simulation are decomposition of the feed, gasification reactions and gas solid separation.

The Aspen Plus yield reactor (RYield) is normally used when reaction stoichiometry is unknown but yield distribution is known. Biomass is given as an input material stream to the RYield reactor which decomposes it into components including Hydrogen, Oxygen, Sulphur, Nitrogen and ash based on the ultimate analysis.

The Gibbs reactor (RGibbs) is used when reaction stoichiometry is unknown, but the reactor temperature and pressure are known. It can model single phase chemical equilibrium or simultaneous phase and chemical equilibria. The components of biomass are fed into the RGibbs along with the gasifying agents, air and steam. The Gibbs reactor predicts the constituents of syngas through Gibbs free energy minimisation.

The Gibbs reactor is followed by a separation column to separate gases and solids.

All the components are integrated to model the gasification process and the process flow sheet is shown in Fig. 1.

Rice husk, the feed stock used is defined as a nonconventional solid and is specified by its proximate and ultimate analyses. The stream class used for modelling is MCINCPSD as it includes the substreams mixed, conventional solids and nonconventional solids. All the gases are taken as mixed substreams, char as conventional solid substream, biomass and ash as nonconventional solid substreams.
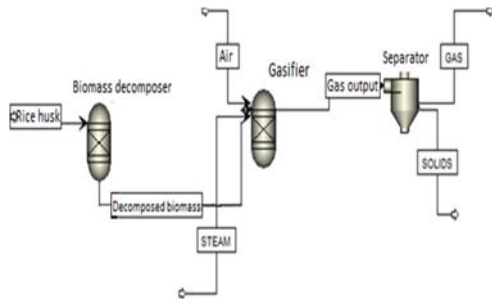
Fig. 1 Process Flowsheet

C. Model Validation

The accuracy of the model is checked by comparing the gas composition predicted by the model with the experimental results of Campoy *et al.* [11]. The comparison is shown in Fig. 2.

D. Model Application

The developed model is used to analyse the effect of temperature, steam to biomass ratio (SBR) and equivalence ratio (ER) on syngas composition, gas yield and first law efficiency. Lower heating value of the dry product gas is estimated from the gas composition and is expressed in volume basis as [12],

$$LHV = 10.79\ Y_{H_2} + 12.26 Y_{CO} + 35.81 Y_{CH_4}$$
$$(1)$$

The flow rate of dry synthesis gas was calculated using the relation [12],

$$V_{dg} = \frac{V_m \text{x} (m_{N_a} + m_{N_b})}{Y_N \acute{M}_N} \qquad (2)$$

Gasification efficiency of the process is given by

$$\eta_{gas} = \frac{\text{Energy content in the product gas}}{\text{Energy content in biomass+Energy content in steam}}$$
$$(3)$$

Table. 1 Proximate and ultimate analyses of rice husk [13]

Proximate analysis (wt. %)		Ultimate analysis (wt. %)	
Moisture	12	C	34.35
Volatile Matter	58	H	5.22
Ash	18	O	57.66
Fixed Carbon	12	N	2.43
		S	0.31

III. RESULTS AND DISCUSSION

A. Effect of ER, SBR and Temperature on gas composition

The effects of equivalence ratio, steam to biomass ratio and temperature on product gas composition are shown in the Figs. 3-5. It is seen that the volume fraction of carbon dioxide increases while that of all other gaseous species decreases with increase in ER. The shifting of the process towards combustion with increase in air flow rate is the reason for this. Similar variations were reported by Puig-Arnavat *et al.* [14] and Rupesh *et al.* [15].
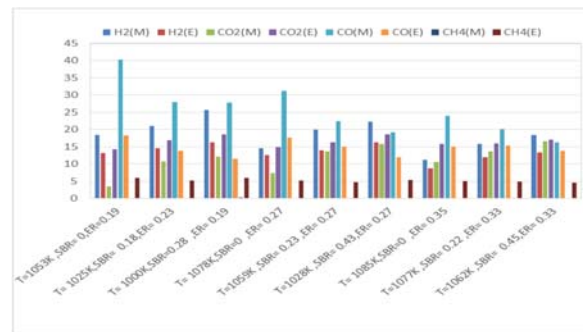

Fig. 2 Comparison between experimental and model results. E: Experimental result; M: model results.

Fig. 4 depicts the variation in product gas composition with steam to biomass ratio. The hydrogen concentration increases with SBR but the rate of increase declines gradually.
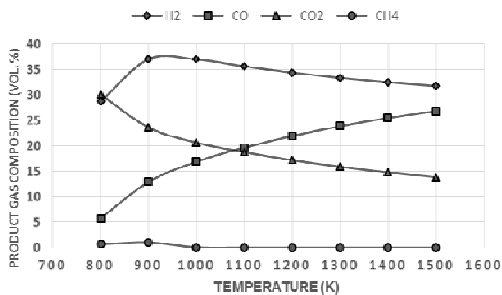

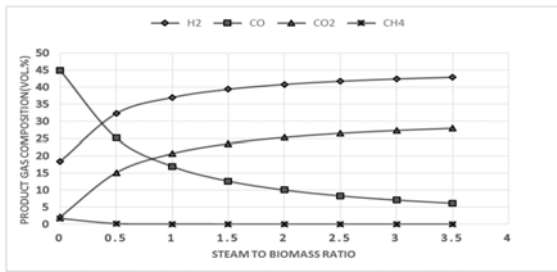Fig. 3 Variation of syngas composition with temperature

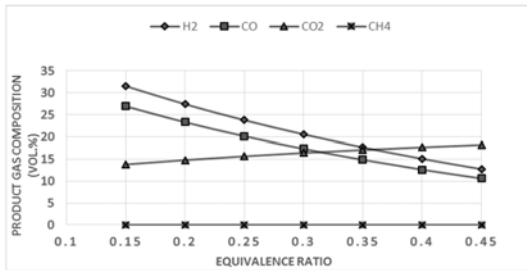Fig. 4 Variation of syngas composition with SBR

Fig. 5 Variation of product gas composition with ER

The combined effect of water gas, steam methane reforming and water gas shift reactions is responsible for this increase. It can also be noted that with steam addition the mole fraction of carbon dioxide increases while that of carbon monoxide decreases. The exothermic nature of water gas shift reaction is responsible for the rapid increase in CO_2 at lower temperatures.

It is also found that hydrogen concentration initially increases with reactor temperature up to a maximum value and then shows a gradual decrease similar to the variation reported by Lv *et al.* [16]. This is due to the exothermic nature of the water gas shift reaction.

At higher temperatures the reaction proceeds in the reverse direction as per Le-Chatelier's principle which results in a decrease in Hydrogen concentration. The endothermic char gasification reaction, water gas reaction, methane reformation and the reversal of water gas shift reaction contribute to the increase in carbon monoxide concentration with temperature. The yield of carbon dioxide and methane are found to decrease with temperature. Methane concentration decreases as the endothermic steam methane reforming proceeds in the forward direction and the exothermic methanation reaction proceeds in the reverse direction.

B. Effect of ER, SBR, and Temperature on Efficiency

The variation of efficiency with process parameters is shown in Figs. 6-8. It is observed that the efficiency initially increases as steam is supplied and then decreases with increase in steam to biomass ratio. This decrease in efficiency is due to the increased energy input in the form of steam. As the equivalence ratio increases the LHV of the product gas decreases, which again results in a decrease in efficiency. For a steam to biomass ratio of 1 and equivalence ratio 0.25 the maximum efficiency of 77.83% is achieved at 1500 K.
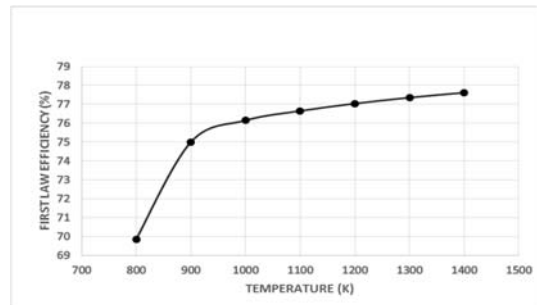

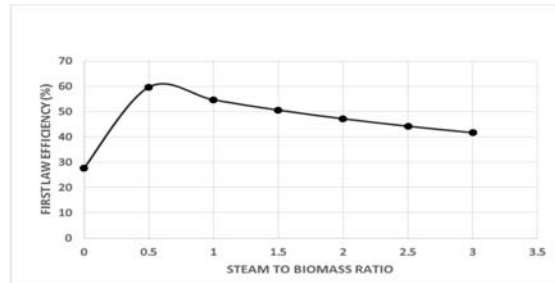Fig. 6 Variation of first law efficiency with temperature

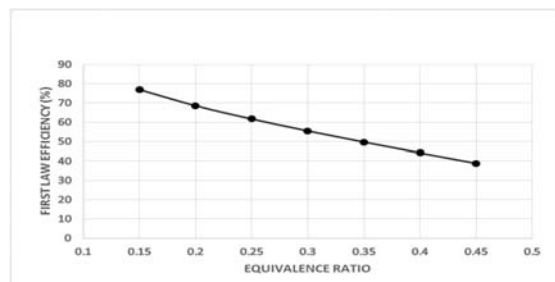Fig. 7 Variation of first law efficiency with SBR

Fig. 8 Variation of first law efficiency with ER

IV. CONCLUSION

A one compartment Aspen Plus model was developed to simulate air-steam gasification of rice-husk in a fluidised bed gasifier and the

effect of process parameters on gasifier yield and efficiency was investigated. For an SBR of unity and ER of 0.25, the maximum hydrogen yield was found to be 37.05 % at 1000 K. A two compartment model incorporating reaction kinetics may give better results.

REFERENCES

[1] P. Basu, Biomass Gasification and Pyrolysis: Practical Design and Theory, Academic Press, London, UK, 1st edition, 2010.

[2] Aspen Technology, Inc., ASPEN PLUS User Models, Cambridge: Aspentech,2006.

[3] C. Franco, F. Pinto, I. Gulyurtlu and I. Cabrita, "The study of reactions influencing the biomass steam gasification process," Fuel, Vol. 82, pp. 835-842, 2003.

[4] W. Doherty, A. Reynolds, D. Kennedy. Simulation of a Circulating Fluidised Bed Biomass Gasifier Using ASPEN Plus – A Performance Analysis, in A. Ziebik, Z. Kolenda, and W. Stanek (eds). Proc. 21st International Conference on Efficiency, Cost, Optimization, Simulation and Environmental Impact of Energy Systems, Krakow, Poland, 2008, pp. 1241-1248.

[5] Stavros Michailos, Anastasia Zabaniotou, Simulation of Olive Kernel Gasification in a Bubbling Fluidized Bed Pilot Scale Reactor, Energy Conversion and Management, Vol. 43,2002, pp. 1291–1299.

[6] Mathieu P., Dubuisson R. Performance analysis of a biomass gasifier. Energy Conversion and Management 2002,Vol. 43, pp. 1291-9.

[7] K. G. Mansaray, A. M. Al-Taweel, A. E. Ghaly, F. Ham- dullahpur and V. I. Ugursal, "Mathematical Modelling of a Fluidized Bed Rice Husk Gasifier," Energy Sources, Vol. 22, No. 1, 2000, pp. 83-98.

[8] Mehrdokht B. Nikoo, Nader Mahinpey, Simulation of biomass gasification in fluidized bed reactor using ASPEN PLUS, Biomass and Bioenergy, Vol.32, 2008, pp.1245-1254.

[9] Frederic Paviet, FlorentChazarenc, MohandTazerout, Thermo Chemical Equilibrium Modelling of a Biomass Gasifying Process Using ASPEN PLUS, International Journal of Chemical Reactor Engineering, Vol. 7, 2009, Article A40.

[10] Kumar, A.; Noureddini, H.; Demirel, Y.; Jones, D.D.; Hanna, M.A. Simulation of corn stover and distillers grains gasification with Aspen Plus, Trans. ASABE 2009, 52, pp. 1989–1995.

[11] M. Campoy, A. G´omez-Barea, A. L. Villanueva, and P. Ollero,"Air-steam gasification of biomass in a fluidized bed under simulated autothermal and adiabatic conditions," Industrial and Engineering Chemistry Research, vol. 47, no. 16, pp. 5957–5965,2008.

[12] S. Kaewluan and S. Pipatmanomai, "Potential of synthesis gas production from rubber wood chip gasification in a bubbling fluidised bed gasifier," Energy Conversion and Management, vol.52, no. 1, pp. 75–84, 2011.

[13] Sajith, U.K., Rupesh, S., Muraleedharan, C., Arun, P.: Characterisation of Biomass for Gasification, National conference on Latest Trends in Mechanical Engineering, Palakkad. March 2014.

[14] M. Puig-Arnavat, J. C. Bruno, and A. Coronas, "Modified thermodynamic equilibrium model for biomass gasification: a study of the influence of operating conditions," Energy & Fuels, vol. 26, no. 2, pp. 1385–1394, 2012.

[15] Rupesh, S., Muraleedharan, C., Arun P.: Analysis of Hydrogen Generation through Thermo-chemical Gasification of Coconut Shell Using Thermodynamic Equilibrium Model Considering Char and Tar. International Scholarly Research Notices. 2014, 1-9, 2014.

[16] P.M. Lv, Z. H. Xiong, J. Chang, C. Z.Wu,Y.Chen, and J. X. Zhu, "An experimental study on biomass air-steam gasification in a fluidized bed," Bioresource Technology, vol. 95, no. 1, pp. 95–101,2004.

[9] Matteo Strano. "Technological Representation of Forming Limits for Negative Incremental Forming of Thin Aluminum Sheets". Journal of manufacturing processes, vol. 7/No.2, pp. 122-129, 2005.

[10] G. Ambrogio, I. Costantino, L. De Napoli, L. Filice, L. Fratini, M. Muzzupappa. "Influence of some relevant process parameters on the dimensional accuracy in incremental forming: a numerical and experimental investigation". Journal of Materials Processing Technology, vol. 153–154, pp. 501-507, 2004.

[11] G. Ambrogio, V. Cozza, L. Filice, F. Micari. "An analytical model for improving precision in single point incremental forming". Journal of Materials Processing Technology, vol. 191, pp. 92–95, 2007.

[12] Myoung-Sup Shim, Jong-Jin park. "The formability of aluminum sheet in incremental forming". Journal of materials processing Technology, vol. 113, pp. 654-658, 2001.

[13] M. Durante, A. Formisano, A. Langella, F. Memola Capece Minutolo. "The influence of tool rotation on an incremental forming process". Journal of Materials Processing Technology, vol. 209, pp. 4621–4626, 2009.

[14] Bozkurt, Yahya. "The optimization of friction stir welding process parameters to achieve maximum tensile strength in polyethylene sheets". Materials & Design, vol. 35, 440-445, 2012.

[15] Bilici, Mustafa Kemal. "Application of Taguchi approach to optimize friction stir spot welding parameters of polypropylene". Materials & Design, vol. 35, pp. 113-119, 2012.

[16] Muthukrishnan, N., and J. Paulo Davim. "Optimization of machining parameters of Al/SiC-MMC with ANOVA and ANN analysis". Journal of materials processing technology vol. 209.1, pp. 225-232, 2009.

NUMERICAL STUDIES ON HIGH PRESSURE RATIO AIRFOILS FOR AXIAL FLOW COMPRESSORS

Aravind G P[1], Nilesh P Salunke[2], Salim A. Channiwala[3]
[1, 2, 3,] Sardar Vallabhbhai National Institute of Technology,

Abstract— The gas turbine engine manufacturers are looking for the efficient engines which can produce higher thrust, and having higher thrust to weight ratio. To achieve these goals, improvement in compressor blade design is essential. Therefore, the goal of the blade design is to achieve the desired flow turning with minimum losses, within the constraint of the blade rows. The new airfoil design include various parameterization, meshing, solving N-S computation and optimization techniques. A CDA airfoil section has been used as base airfoil and then parameterized by Bezier Parsec parameterization method. The optimization of parametric CDA cascade model is carried out by Genetic algorithm coupled with CFD. Parameterization and generation of new airfoil coordinates are made using the programme code prepared in Matlab. Numerical simulation have been carried out by CFD software GAMBIT and FLUENT. Matlab evaluates the airfoil and optimizes the airfoil using Genetic algorithms and checks the objective function in each iteration. The main objective is to get lower value of total pressure loss coefficient at higher pressure ratio without any flow separation.

This would indicates that the airfoil section is capable of producing that pressure ratio without flow separation. This process is repeated till an optimum solution reached. The maximum pressure ratio attained by base airfoil was found out to be 1.4. The process was carried out for finding solutions for higher pressure ratios. The optimal solutions are obtained for higher pressure ratios up to 3.0.

Index Terms— Numerical Simulation, High Pressure Ratio Airfoils**.**

NOMENCLATURES

b	Bezier Parameter
c	Chord
y	Camber/Thickness
k	Curvature
p	Static Pressure
T	Static Temperature
Po	Stagnation Pressure
To	Stagnation Temperature
V	Velocity
U	Peripheral Velocity
C_D	Coefficient of Drag
ΔPo	Total Pressure Loss
r	Radius

β	Blade angle
θ	Camber angle
ω	Total Pressure Loss Coefficient
X_{cg} ,Y_{cg}	Center of Gravity of airfoil
Cp	Coefficient of Pressure
γ	Stagger angle

I. INTRODUCTION

The study of turbomachinery has gone through several historical stages from the 1940s till now. The study in this period has moved from one-dimensional to two-dimensional and three-dimensional flows, from inviscid to viscous flows, and from steady to unsteady flows [1]. The principal type of compressor being used nowadays, in majority of the gas turbine and power plants and especially in aircraft applications, is the axial flow compressor. This dominance is mainly due to the ability of the axial flow compressor to satisfy the basic requirements of the aircraft gas turbine. Transonic axial flow compressors are today widely used in aircraft engines to obtain maximum pressure ratios per single stage. High stage pressure ratios are important because they make it possible to reduce the engine weight and size and, therefore investment and operational costs. Performance of transonic compressors has today reached a high level but engine manufacturers are oriented towards increasing it further [2]. A small increment in efficiency, for instance, can result in huge savings in fuel costs. The increase in gas turbine efficiency mainly dependent on Increase in Pressure Ratio. So in the present work CDA airfoil is parameterized and optimized for higher pressure ratios up to 3.0 with reduction of overall total pressure loss.

II. LITERATURE REVIEW

One of the challenging topics in optimization is the selection of the mathematical representation of airfoil design variables that provides a wide variety of possible airfoil shapes. A new method for airfoil shape parameterization is presented which takes into consideration the characteristics of viscous transonic flow particularly around the trailing edge. Typical practice is to resort to using a series of curves, such as polynomials and Bezier curves, to describe the profile. This typically reduces the number of degrees of freedom to a much smaller, manageable number. The method is then applied to airfoil shape optimization at high Reynolds number turbulent flow conditions using a Genetic Algorithm [3]. The influence of the selection of the parameterization on the optimization has received relatively little consideration to date. A new airfoil parameterization, Bezier-PARSEC, that was developed to extend and improve the typical Bezier parameterization found in use. This parameterization was found to fit the known shape of a wide range of existing airfoil profiles as well as resulting in accelerated convergence. [4], [5]. Another innovative method for airfoil geometry optimization is based on the coupling of a PARSEC parameterization for airfoil shape and a genetic algorithms (GA) optimization method to find Nash equilibria (NE). While the PARSEC airfoil parameterization method has the capability to faithfully describe an airfoil geometry using typical engineering parameters, on the other hand the Nash game theoretical approach allows each player to decide, with a more physical correspondence between geometric parameters and objective function, in which direction the airfoil shape should be modified[6]. Lars Sommer [7] introduces a new curvature based design parameterization of two-dimensional high pressure compressor blade sections to be used in a multi-criteria aerodynamic design optimization process. The suction side of the airfoil section is represented by its curvature distribution which is described by a B-spline curve. The coordinates are then derived by numerical integration. The camber line as well as pressure side are obtained by adding a thickness distribution perpendicularly to the camber line. Yongsheng Lian [8] reviewed the recent progress in design optimization using evolutionary algorithms to solve real-world aerodynamic problems. Evolutionary algorithms (EAs) are useful tools in design optimization. Due to their simplicity, ease of use, and suitability for multi-objective design

optimization problems, EAs have been applied to design optimization problems from various areas. Sergey Peigin [9] suggested a new approach to the constrained design of aerodynamic shapes. The approach employs Genetic Algorithms (GAs) as an optimization tool in combination with a Reduced-Order Models (ROM) method based on linked local data bases obtained by full Navier–Stokes computations. Naixing Chen [10] describes an optimization methodology for aerodynamic design of turbomachinery combined with a rapid 3D blade and grid generator (RAPID3DGRID), a N.S. solver, a blade parameterization method (BPM), a gradient-based parameterization-analyzing method (GPAM), a response surface method (RSM) with zooming algorithm and a simple gradient method. Syam [11] suggested the Bezier-PARSEC method for camber and thickness distribution of CDA airfoil and Genetic Algorithm for optimization. T Sonoda [12] introduced two different numerical optimization methods; the evolution strategy (ES) and the multi-objective genetic algorithm (MOGA), which were adopted for the design process to minimize the total pressure loss and the deviation angle at the design point at low Reynolds number condition. Akira Oyama [13] developed a reliable and efficient aerodynamic design optimization tool using evolutionary algorithm for transonic compressor blades.

III. PARAMETERIZATION AND OPTIMIZATION

Here we are introducing the method used for the parameterization of CD Airfoil and the MATLAB Genetic Algorithm (GA) toolbox used for Optimization. The mainly used parameterization methods are briefly presented herein.

A. Bezier Curves [3]

One of the most popular methods for airfoil shape representation is the Bezier curve method that introduces control points around the geometry. These points are then used to define the airfoil shape. A Bezier curve of degree n is uniquely defined by n +1 vertex points of a polygon. These vertices are called the control points of the nth order Bezier curve. The general expression for an nth order Bezier curve is given below:

$$P(u) =$$
$$\sum_{t=0}^{n} P_i \left(\frac{n!}{i!(n-1)!} \right) u^i (1u)^{n-i} \qquad (1)$$

Where Pi = i^{th} control point. The parameter u goes from 0 to 1; with 0 at the zeroth control point and unity at the nth control point. The Bezier parameterization is determined by its control points which are physical points in the plane. However the other control points need not be on the curve even though they determine the shape of the curve. The number of design variables is often so high that the computational time of the whole process becomes unaffordable. Fainekos and Giannakoglou [14] used the Bezier curve to define the airfoil shape in inverse design of turbomachinery blade airfoils. In their research, Fainekos and Giannakoglou [14] fixed the leading edge and trailing edge control points and also abscissas of the rest of the control points. Song and Keane [15] compared the Bezier curve method with original basis functions in generating airfoils and concluded that the Bezier curve produces better shapes in terms of accuracy but at a higher computational time. In addition, special curvature distributions that are required to achieve a desirable pressure distribution are not evident in this method.

B. PARSEC method [3]

Another common method for airfoil shape parameterization is PARSEC which has been successfully applied to many airfoil design problems. This technique has been developed to control important aerodynamic features by using the finite number of design parameters. In this method there are basic eleven parameters that are used in PARSEC method including leading edge radius (r_{LE}), upper and lower crest locations (X_{UP} , Z_{UP} , X_{LO} , Z_{LO}) and curvatures (Z_{xxUP} Z_{xxLO}), trailing edge coordinate(Z_{TE}) and direction(α_{TE}), trailing edge wedge angle(β_{TE}) and thickness(ΔZ_{TE}). A linear combination of shape functions is used to present the airfoil shape in this method.

$$Z_K = \sum_{n=1}^{6} a_{n,k} X_K^{(n-1)/2} \tag{2}$$

The coefficients a_n are determined from defined geometric parameters. The airfoil is divided into upper and lower surfaces and the coefficients a_n are determined using the information of the points in each section. The subscript k changes from 1 to 2 in order to consider the length of the upper and lower surfaces, respectively.

C. Bezier PARSEC Parameterization [4]

Derksen and Rogalsky [4] have introduced the Bezier–PARSEC parameterization. This approach will use the advantages of both the Bezier and PARSEC parameterization and avoid the disadvantages of both to represent the airfoil and provide enough flexibility over geometrical and aerodynamic parameters. Their approach is further subdivided into two parameterization methods viz. BP3333 and BP3434. In both the methods, Bezier control points are determined in terms of the PARSEC parameters of an airfoil. The camber-thickness formulation of the Bezier curves is more directly related to the flow than is the upper curve-lower curve formulation for PARSEC, while the PARSEC parameters are more aerodynamically oriented than the Bezier parameters. The BP parameterization uses the PARSEC variables as parameters, which in turn define four separate Bezier curves. These curves describe the leading and trailing portions of the camber line, and the leading and trailing portion of the thickness distributions. While the Bezier parameterization joins the leading and trailing curves with first-order continuity.

The BP parameterization uses second-order continuity. The parameters are:

Leading edge radius – rle,
Trailing camber line angle – ate,
Trailing wedge angle – bte,
Trailing edge vertical displacement – zte,
Leading edge direction -gle,
Location of the camber crest –xc, yc,
Curvature of the camber crest – kc,
Position of the thickness crest – xt, yt,
Curvature of the thickness crest –kt ,
the half thickness of the trailing edge –dzte, and several Bezier variables, b0, b2,b8, b15 and b17.

This type of parameterization improves the robustness and convergence speed for aerodynamic optimization, which makes it more suitable for optimization using Genetic algorithms.

D. Optimization of Base CDA using GA [11]

Total pressure loss as objective function for optimization since it is more significant in the compressor blade efficiency. And the optimization is carried out for compressor cascade at high subsonic velocities. The optimization is meant for finding a profile section with minimal loss for the compressor blade. In this investigation we selected a CDA cascade, third stage of a compressor for the optimization. Before starting the optimization process we used to analyze the base cascade to predict the performance. The analysis is carried out numerically in CFD softwares, Gambit for modeling and meshing and Fluent for analysis. The optimization of cascade has mainly five steps as shown on the optimization flow chart. All the process is carried out using Matlab code. The design parameters are selected from the parameters obtained from the BP334. This new parameters are generated at each iteration by the GA based on the constraints and the objective function. We selected 15 parameters of BP3434 for optimizing the cascade. The first step is terminated with the generation of the new parameters by GA. The next step is to generate the airfoil section from these parameters. In the third step CFD software Gambit is called in Matlab in batch mode for the cascade modeling and meshing using reading the Gambit journal file in Matlab. After the completion and generation of the mesh file as a fourth step Fluent is called in Matlab using the system command and reads the Fluent journal file, which includes all the commands for the analysis. By the execution of the Fluent we will get all the inlet and outlet parameters such as total pressures, total temperatures, static pressures, Mach numbers, etc. Also we will get the flow parameters over the cascade i.e. Mach number, static pressure, etc. The objective function is selected as total pressure loss coefficient for this optimization which calculated from the results of Fluent analysis. At

each iteration GA checks the value of the loss coefficient for the next generation of next population of parameters. The process ends when the loss coefficient is minimized. Genetic Algorithm (GA) is used as an optimization algorithm because of its global optimization nature and speed of convergence. The objective function used for GA is total pressure loss coefficient. We selected the constraint as Chord length of the Cascade and is fixed as 46.46 mm and set the number of generation as 100 with a crossover fraction of 0.8. After calculating and checking the value of loss coefficient GA generates the new population based on the crossover, selection and mutation with a constraint fixed chord length.

After the convergence of the optimization algorithm for a generation of 100 we obtained the airfoil section which has minimized the objective function. The table 1 shows the newly generated profile has optimal total pressure loss coefficient compared to the base profile.

Table 1: Comparison of Base and Optimized Airfoil [11]

Airfoil Sections	Total pressure		Pressure loss coefficient
	Inlet	Outlet	
Base Airfoil	33800	335150	0.0427
Optimized Airfoil	33800	335370	0.0394

This process was repeated for various pressure ratios ranging from 1.1 to higher pressure ratios and it was found that there was a drag reversal after a pressure ratio of 1.4. The negative drag indicates the reversal of flow hence we derived a conclusion that a pressure ratio greater than 1.4 cannot be achieved from the above airfoil for the given set of conditions and there is a need to optimize the airfoil further to gain higher pressure ratios.

E. Optimization of CDA for Higher Pressure Ratios up to 2.4 [16] [17]

The following boundary conditions were applied:

Solver: Green Gauss node based, 2d, steady, implicit, density based
Model: Spalart-Allmarus
Convergence Criteria: 0.001
Fluid: Air with ideal gas density and Sutherland viscosity
Discretization: Flow: Second order upwind
Modified turbulent viscosity: Second order upwind
Inlet Total Pressure P_{O1} = 338000 Pa
Inlet Total Temperature T_{O1} = 426K

Boundary conditions:

Table 2: Boundary Conditions for Higher PR [16] [17]

Pressure Ratio	Inlet Mach No.	P_1 (Pa)	T_{02} (K)	P_2 (Pa)
1.5	0.75	232737.6	478.3231	349106.5
1.6	0.75	232737.6	487.225	372380.2
1.7	0.75	232737.6	495.7379	395654
1.8	0.75	232737.6	503.9003	418927.8
1.9	0.75	232737.6	511.7449	442201.5
2.0	0.75	232737.6	519.2998	465475.3
2.2	1.2	139383.4	533.6354	306643.62
2.4	1.4	106213.4	547.0681	254912.62

The table 3 shows the total pressure loss coefficient obtained up to 2.4 pressure ratios

Table 3: Pressure loss coefficient comparison up to 2.4 PR [17]

Pressure Ratio	CDA Base Airfoil	Optimized Airfoils
	Pressure Loss Coefficient	Pressure Loss Coefficient
1.5	----	0.007903
1.6	----	0.006527
1.7	----	0.009531
1.8	----	0.005681
1.9	----	0.004332
2.0	----	0.017324
2.2	----	0.008038
2.4	----	0.015610

IV. SIMULATION RESULTS OF HIGHER PRESSURE RATIOS MORE THAN 2.4

Further optimization of the airfoil and up to how much pressure ratio will be possible is found out

in this work. We obtained a pressure ratio of 3.0 without any flow separation for a Mach number of 1.4. Beyond that further optimization is not possible with this method.

**Table 4: Boundary conditions for Higher PR up to 3.1**

Pressure Ratio	Inlet Mach No	P_1 (Pa)	T_{02} (K)	P_2 (Pa)
2.6	1.4	106213.4	559.7233	276154.9
2.8	1.4	106213.4	571.7011	297397.6
3.0	1.4	106213.4	583.0824	318640.2

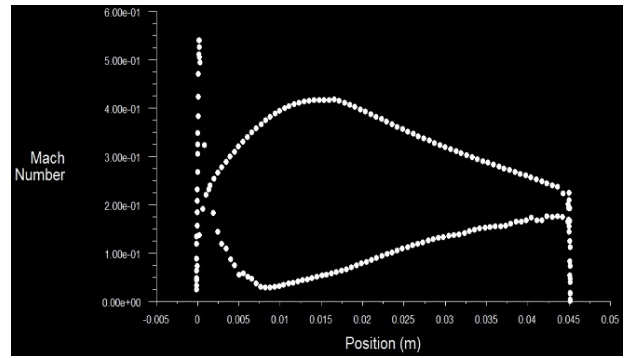The boundary conditions for pressure ratios up to 3.0 is as shown in table 4.

Distribution of Mach number of Optimized airfoils are given below.
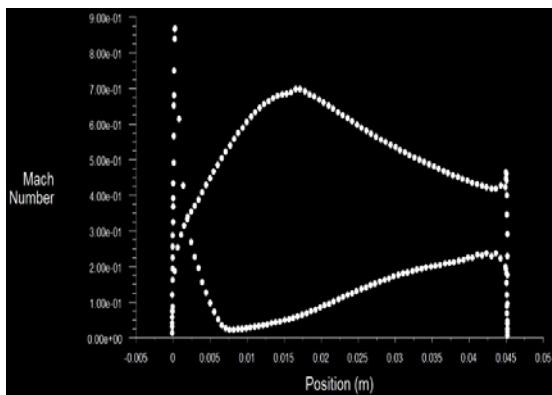
Figure 1: Mach number plot for optimized 2.6 PR airfoil
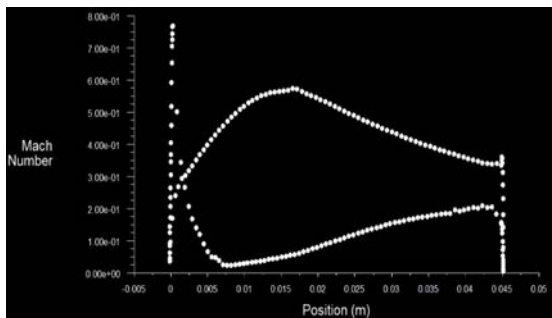
Figure 2: Mach number plot for optimized 2.8 PR airfoil

Figure 3: Mach number pot for optimized 3.0 PR airfoil

The newly optimized airfoils can perform better at higher pressure ratios up to 3.0. The optimized blades have shown perfect velocity and pressure distribution as of CDA. In the above plots we can see the exit Mach number is reducing as the pressure ratio increases.

Table 5: Pressure Loss Coefficient Comparison for PR up to 3.0

Pressure Ratio	CDA Base Airfoil	Optimized Airfoils
	Pressure Loss Coefficient	Pressure Loss Coefficient
2.6	----	0.006009
2.8	----	0.001717
3.0	----	0.007102

V. VALIDATION OF SIMULATION RESULTS

The optimized airfoil showed close CDA characteristics which confirm its good behaviour at higher pressure ratios. The suction peak is low at higher pressure ratios as expected and uniform diffusion is there till the trailing edge. The pressure on the lower surface increases uniformly till trailing edge. It is also observed that as the pressure ratio increases the peak Mach number decreases. For given pressure ratios, on upper surface, the Mach number first increases to a value of peak Mach number and thereafter it reduces continuously. On lower surface, Mach number first reduces and then increases gradually. It signifies that over upper surface, fluid is accelerated first and then it decelerates constantly to match the flow conditions at the trailing edge. These all are the typical characteristics of a controlled diffusion airfoil. Hence our optimized airfoils exhibit the characteristics of a CDA airfoil.

VI. CONCLUSION

- The parameterization and GA optimization method is capable of finding efficient and optimum airfoils in fewer number of generations.
- The development of a combined Bezier-PARSEC (BP) parameterization utilize the advantages of both the Bezier and PARSEC parameterizations.
- Coupling of Bezier-PARSEC parameterization with GA and CFD together, offers an optimal cascade profile with a reasonable total pressure loss co efficient reduction with efficient flow pattern over the cascade.
- The base CDA airfoil can offer maximum pressure ratio of 1.4, beyond which a converged solution is not obtained indicating that it cannot gain pressure ratios higher than 1.4.
- The blade optimization with Bezier PARSEC Parameterization has offered most optimized results. The newly optimized blades can perform better at higher pressure ratios up to 3.0. The optimized blades have shown perfect velocity and pressure distribution as of CDA. Up to 3.0 PR and Mach 1.4 we can use these optimized airfoils without any flow separation.

REFERENCES

1. Naixing Chen., Aerothermodynamics of Turbomachinery Analysis and Design, 1st Edition, John Wiley & Sons,Singapore,2010,chap.14.
2. Saravanamuttoo H.I.H, Rogers G. F. C, Henry Cohen., Gas Turbine Theory, 6th Edition, Prentice Hall, USA, 2008.chap.5
3. Ava Shahrokhi, Alireza Jahangirian, "Airfoil shape parameterization for optimum Navier–Stokes design with genetic algorithm", Aerospace science and technology, 11(2007) 443-450
4. R.W. Derksen, Tim Rogalsky, "Bezier-PARSEC: An optimized aerofoil parameterization for design", Advances in Engineering Software 41 (2010) 923–930.
5. Athar Kharal, Ayman Saleem, "Neural networks based airfoil generation for a given Cp using Bezier–PARSEC Parameterization", Aerospace Science and Technology 23 (2012) 330–344.
6. Pierluigi Della Vecchia, Elia Daniele, Egidio D'Amato, "An airfoil shape optimization technique coupling PARSEC parameterization and evolutionary algorithm", Aerospace Science and Technology 32 (2014) 103–110.
7. Lars Sommer, Dieter Bestle, "Curvature driven two-dimensional multi-objective optimization of compressor blade sections", Aerospace Science and Technology 15 (2011) 334–342.
8. Yongsheng Lian, Akira Oyama, Meng-Sing Liou, "Progress in design optimization using evolutionary algorithms for aerodynamic problems", Progress in Aerospace Sciences 46 (2010) 199–223
9. Sergey Peigin, Boris Epstein, "Robust optimization of 2D airfoils driven by full Navier–Stokes computations", Computers & Fluids 33 (2004) 1175–1200.
10. Naixing Chen, Hongwu Zhang, Yanji Xu, Weiguang Huang, "Blade Parameterization and Aerodynamic Design Optimization for a 3D Transonic Compressor Rotor", Proceedings of the 8th International Symposium on Experimental and Computational Aerothermodynamics of Internal Flows Lyon, July 2007, Paper reference: ISAIF8-0021
11. Syam, Channiwala S A, "Optimization of CDA cascade using Parameterization and Genetic Algorithm coupled with CFD", 2nd International Conference on Mechanical, Automotive and Aerospace Engineering, ICMAAE 2013.
12. T Sonoda, Y Yamaguchi, T Arima, M Olhofer, B Senghoff and H A Schreiber, "Advanced High Turning Compressor Airfoils for Low Reynolds Number Conditions, Part 1: Design and Optimization", Proceedings of ASME Turbo Expo 2003, GT 2003-38458.

13. Akira Oyama, Meng sing Liou, Shigeru Obayashi, "Transonic Axial Flow Blade Shape Optimization using Evolutionary Algorithm and 3D Navier Stokes Solver", AIAA Journal of Propulsion and power, 2002-5642.

14. Fainekos and Giannakoglou, Inverse Problems in Science and Engineering, 4th Edition, Taylor & Francis, UK, 2004 chap 4.

15. Song W, Keane A, A Study of Shape Parameterization Methods for Airfoil Optimisation, 10th AIAA/ISSMO Multidisciplinary Analysis and Optimization Conference, 2004-4482.

16. Vilash Rajendra Shingare, A study on High Pressure Ratio Airfoils for Axial Flow compressors, Mtech Thesis, S. V. National Institute of Technology, Surat, 2012.

17. Rajesh N, High Pressure Ratio Blade Design by Parameterization and Optimization, MTech Thesis S. V. National Institute of Technology, (2014).

18. MATLAB User Guide Genetic Algorithm and Direct Search Toolbox User's Guide Copyright, Mathworks, 2004.

DIGITAL SIMULATION OF PRODUCER GAS FIRED SI ENGINE

Rahul P. Nagpure[1], Parth D. Shah[2], Salim A. Channiwala[3]
[1, 2, 3]Sardar Vallabhbhai National Institute of Technology

Abstract—Engine emissions becoming stringent, gaseous fuels are gaining prominence as cleaner fuels like LPG and CNG both for stationary and automotive applications. But scarcity of those fuels arises big question for future. Producer gas obtained from biomass gasification can be good alternative for non-renewable fuels especially in developing country like India, where biomass is available in huge quantity. In the present study simulation based on actual thermodynamic cycle analysis is performed to assess the performance of 118 cc S.I. engine. All the four basic processes taking place in an S.I. engine are analyzed and the values of pressure and temperature at every 2° of crank rotation are found out with the aid of certain assumptions. The model involves good deal of calculations and iterations and hence, it is coded in 'c'. The simulation result is validated with the technical specifications provided in the technical manual of the engine. Digital simulation shows with producer gas as a fuel power and thermal efficiency relatively de-rated by 11.54 % and 5.72 % respectively, compared to gasoline.

Index Terms— Digital Simulation, Producer Gas Fuel.

NOMENCLATURES

ATDC   After Top Dead Centre
BTDC   Before Top Dead Centre
BMt   Billion Metric tones
CA   Crank Angle
cc   Cubic Centimeters
C_h Convection Heat-Transfer
C_h Convective Heat-Transfer Co-Efficient
C_k Thermal Conductivity
C_m Mean Piston Velocity
CNG   Compressed Natural Gas
CPG   Compressed Producer Gas
CR   Compression Ratio
D   Cylinder Bore
GHG   Greenhouse Gases
h   Steady Turbulent Heat-Transfer
HC   Hydro-Carbons
IA   Ignition Advance
L   Cylinder Stroke Length
LNG   Liquefied Natural Gas
Mtoe   Million Tons of Oil Equivalent
NO_X Nitruc Oxides
Nu   Nusselt Number
Re   Reynolds Number
S.I.   Spark Ignition
V_s Displacement/Swept Volume
W_{mv} Mean Gas Velocity
μ_{cy} Viscosity of Cylinder Gas

I. INTRODUCTION

In the year 2013, India's net imports are nearly 144.3 million tons of crude oil, 16 Mtoe of LNG and 95 Mtoe coal totaling to 255.3 Mtoe of

primary energy which is equal to 42.9% of total primary energy consumption [1]. India imports nearly 75% of its 4.3 million barrels per day crude oil needs but exports nearly 1.25 million barrels per day of refined petroleum products which is nearly 30% of its total production of refined products [2]. The growth of electricity generation in India has been hindered by domestic coal shortages and as a consequence, India's coal imports for electricity generation increased by 18 % in 2010. The electricity sector in India had an installed capacity of 249.488 GW as of end June 2014 [3]. World CO_2 (GHG) emission will grow from 31 BMt in 2010 to 45 BMt in 2040, which is mainly responsible for global warming. This data shows there is desperate need of new renewable energy resource. India has biomass capacity of 66000 MW [2] in form of resources such as rice husk, crop stalks, small wood chips, and other agro-residues. Biomass can be gasified in gasifiers and used as alternative fuel for current depleting fuels.

II. LITERATURE REVIEW

Gasoline has the fastest flame propagation development followed by LPG and CNG, CPG. CPG burns with blue flame compared to violent combustion of gasoline. Presence of H_2 causes fast burning rates initially, which slows down due to low burning speed of CO after H_2 has burnt [4]. CNG having higher efficiency and lower CO, CO_2, HC emission compared to gasoline and LPG but produces more NOx emission [5], [6]. But these fuels are on the verge of depletion. Shashikantha [7] reported that Producer gas with low energy density (5 MJ/kg) but reasonably high mixture energy density (2.12 MJ/kg) can replace these gases with almost same thermal efficiency of 28–32 %. but power derating of up to 30 %. Presence of Hydrogen does not give any pre-ignition problem due to gas being dilute. Producer Gas efficiency increases with increase in CR 30.7 % at CR of 17 and reduces to 27.4 % at CR of 10 [8]. Ignition advance should be retarded for increase in CR. Producer gas can be used up to CR of 17 without formation of knock [8], [9]. It reduces

CO emissions considerably but NO_X and CO_2 will be increased. Hydrogen content in gas increases thermal efficiency but it is limited by process of gasification.

Dual-fuel mode operation requires less modifications giving good performance with diesel as pilot fuel used to generate spark. Supercharging in dual fuel mode improves performance of engine. Brake Thermal efficiency with supercharged producer gas-diesel is 15 % more than premixed producer gas-diesel engine [10]. Diesel can be replaced by biofuels like Honge-Oil making the fuel complete renewable. This dual fuel mode operation in CI engine shows maximum efficiency 20 % with reduction in all emissions. Tri-generation can be best option to utilize maximum part of biomass energy in higher generation systems [11].

III. SIMULATION OF ACTUAL CYCLE

The various models and equations used in simulation are briefly presented herein.

A. Model for Heat Transfer

Woschni's equation was used which is based on the similarity law of steady turbulent heat transfer [13], [14].

$$h = 0.820 * D^{-0.2} * p^{0.8} * W_{mv}^{0.8} * T^{-0.53} \ (kW/m^2.K) \tag{1}$$

The reference velocity W_{mv} in the above formula represent the mean gas velocity affecting heat transfer and is given for each process. D is the cylinder bore taken as the characteristic length,

$$W_{mv} = \left[C_1 * C_m + C_2 * \left(\frac{V_S * T_1}{p * v_1} \right) * (p - p_0) \right] \tag{2}$$

For the gas exchange processes, $C_1 = 6.18$ & $C_2 = 0$,

For the compression processes, $C_1 = 2.28$ & $C_2 = 0$,

For the combustion & expansion processes, $C_1 = 2.28$ & $C_2 = 3.24*10-3$

Here p_0 is the pressure in the MPa obtained for motoring and V_s is the displacement volume in m^3 and the coefficient C_m is the mean piston speed. The subscript 1 denotes a specified time when the pressure and the temperature are known.

In the Suction and Exhaust process Woschni's heat-transfer model was used during the simulation.

Anand [15], separates out the convection and radiations terms. Typical approach to the heat transfer theory proposed by Anand is his expression for the Nusselt number 'Nu' leading to a conventional derivation of the convection heat transfer coefficient C_h.

Anand recommends the following expression to connect the Reynolds and Nusselt number:

$Nu = b*Re^{0.7}$

(3)

Where, b = 0.26, for the two stroke engines and

b = 0.49, for the four stroke engines.
The Reynolds number is calculated as,

$$Re = \frac{\rho_{cylinder}*C_m*D}{\mu_{cylinder}}$$

(4)

The viscosity should be that of the cylinder gas,

$\mu_{cy} = 7.457*10^{-6} + 4.1547*10^{-8}*T - 7.4793*10^{-12}*T^2$ (5)

The mean piston velocity C_m is found from the dimensions of the cylinder stroke, L and the engine speed, N in rev/min.

$$C_m = \frac{2*L*N}{60}$$

(6)

The convectional heat transfer coefficient can be extracted from the Nusselt number, as

$$C_h = \frac{C_k*Nu}{D}$$

(7)

The parameter C_k is the thermal conductivity of the cylinder gas and can be assumed to be identical with that of air at the instantaneous cylinder temperature.

$C_k = 6.1944*10^{-3} + 7.3814*10^{-5}*T - 1.2491*10^{-8}*T^2$ (8)

In the compression and expansion process this heat-transfer model is adopted.

B. Model for Combustion [13]

Wiebe function was used to find out the mass fraction burnt during the combustion process.

$$X_b = 1 - \exp\left[-a*\left(\frac{\theta-\theta_s}{\Delta\theta_c}\right)^{m+1}\right]$$

(9)

Where, X_b is the mass fraction burned, "a" is an efficiency parameter and "m" is a slope parameter.

C. Input Data [16]

For the simulation purpose Honda GX-120 engine had been selected. Its specifications are as follows:

Engine Type   : Air Cooled 4-s petrol engine
Bore * Stroke   : 60 * 42 mm
Swept Volume   : 118 cc
Comp. Ratio   : 8.5:1
Max. Net Torque : 7.3 Nm@2500 rpm
Net Power   : 2.6 kW@3600 rpm
No. of Cylinders : 1
Producer gas composition on volume basis: CO=24.6 %, H_2=21.9 %, CO_2=8.17 %, H_2O^g=7.75 %, N_2=37.53 %.

IV. SIMULATION RESULTS

1. Suction Stroke:

Fig. 1 shows during suction stroke pressure falls rapidly (from initial 0.93 bar) after start of piston downward acceleration up to 50^0 CA, because of low valve lift and lower curtain area allowing less air-fuel mixture coming in cylinder. The cylinder pressure falls to 0.58 bar at   50° CA. However, thereafter a gradual pressure building is

observed due to increased availability of mass flow with higher range due to valve lift and curtain area is sufficiently high to allow gases to pass inside and increase the inner pressure. Peak mass inflow found at 90^0 CA. Suction happens till final pressure reaches atmospheric pressure (1.013 bar). As shown in fig 2 temperature obviously will reduce with increased availability of mass flow with increasing crank angle. The mass-θ curve in fig. 3 clearly shows gradual rise in mass flow during initial valve lift and thereby explain the trend of P-θ curve too. Thus, the basic results of suction process are as per logical trend observed in actual I.C. engines and this validates the model used in present case.
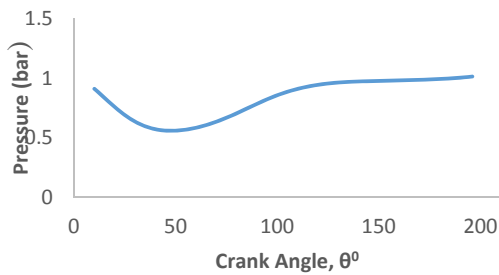

**Fig**.1 P-θ Curve for Suction Stroke
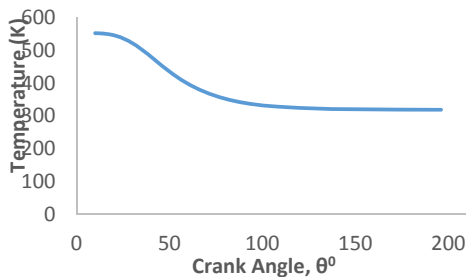
Fig.2 T-θ Curve for Suction Stroke
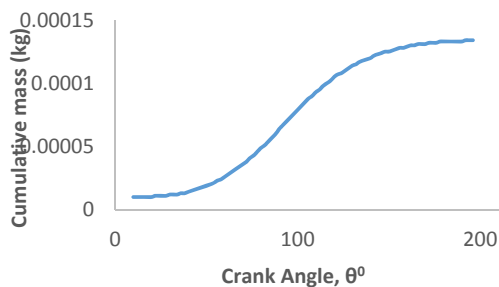
Fig.3 Mass-θ Curve for Suction Stroke

2. Compression stroke:

After suction charge is sealed and compressed with gradual rise of pressure up to 290^0 CA and stiff rise in pressure after 290^0 CA till the final pressure of 14.7 bar as shown in fig.4 and temperature 657 K as shown in fig. 5 at 336^0 CA. Specific heats found to be increasing and compression index gamma reducing at higher temperature. More heat loss occurs as inside temperature increases.
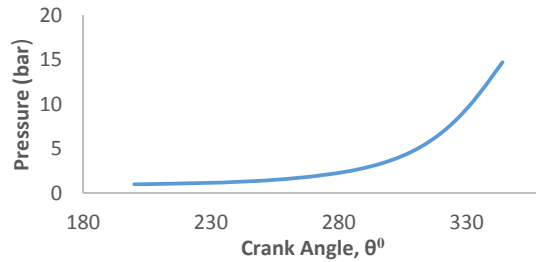
Fig.4 P-θ Curve for Compression Stroke
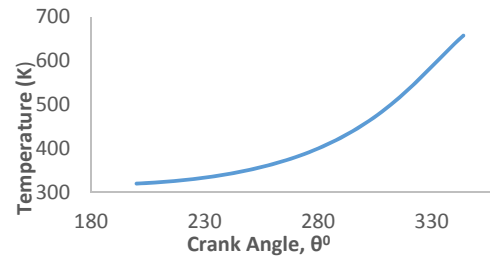
Fig.5 T-θ Curve for Compression Stroke

3. Combustion Process:

Ignition occurs after end of compression 16^0 BTDC causing release of heat from combustion of charge produces peak pressure 38 bar at 372^0 CA as shown in fig.6. The rate of heat addition under these circumstances is more than the heat losses. As a result the temperature continues to rise and reaches to its peak value 1809 K at 379^0 CA as shown in fig.7. Mass burning curve in fig.8 shows higher mass burning rate found during high pressure and temperature formation. At 370^0 CA, 75% of mass has been burnt releasing huge amount of heat to produce peak pressure and temperature. Heat losses found more in this process.
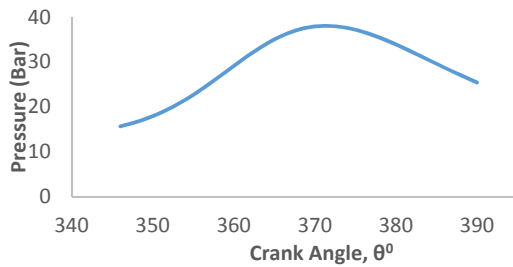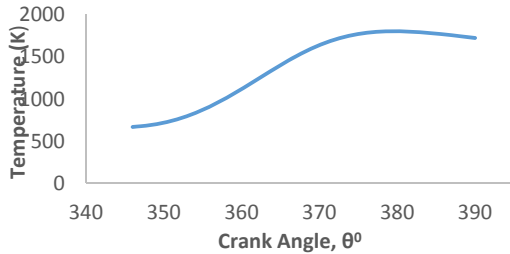
Fig.6 **P-θ Curve for Combustion Process**
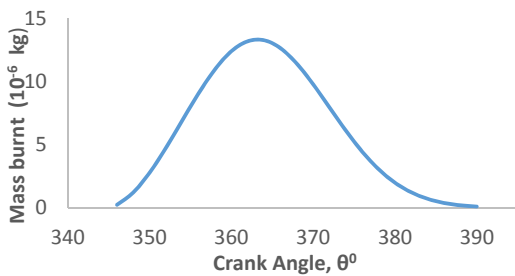

Fig.7 **T-θ Curve for Combustion Process**

Fig.8 Mass burnt-θ Curve for Combustion Process

4. Expansion Stroke:

Combustion products with very high temperature get expanded due to increase in cylinder volume, which in turn reduce the pressure inside the cylinder drastically. At the end of combustion process the pressure inside the cylinder is 25.42 bar as shown in fig.9. This gives higher energy extraction. At the end of expansion process, pressure reduces to 3.5 bar at 510° CA, whereas temperature reaches to 990 K as shown in fig.10. P-θ Curve for expansion stroke shows initial stiff curve of pressure reduction up to 440⁰ CA and then gradual expansion i.e. most of power will be transmitted before 440⁰ CA.
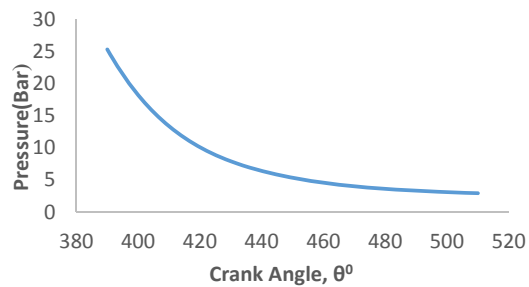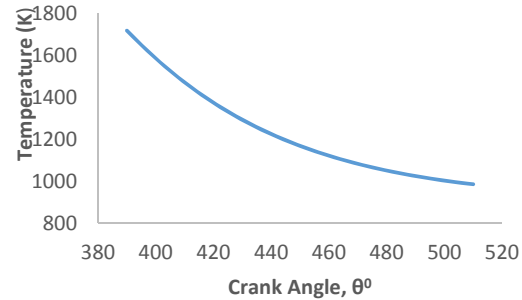

Fig.9 P-θ Curve for Expansion Stroke

Fig.10 T-θ Curve for Expansion Stroke

5. Exhaust Stroke:

During exhaust stroke, pressure falls to 1.02 bar at 610° CA and then rises up to 1.8 bar at the end of exhaust process shown in fig. 11. After 640° CA slow pressure building inside the cylinder is observed due to throttling effect. The temperature obviously will reduce with high temperature burnt mass leaving to the atmosphere with increasing crank angle as shown in fig. 12. It is observed from the T-θ curve that, like pressure, there is not any rise of temperature during the later stage of exhaust process.
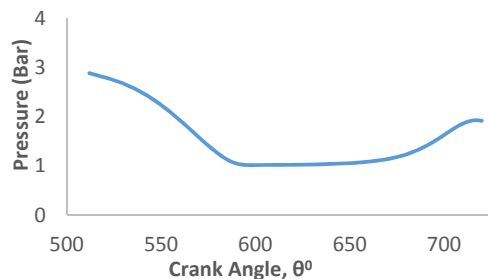

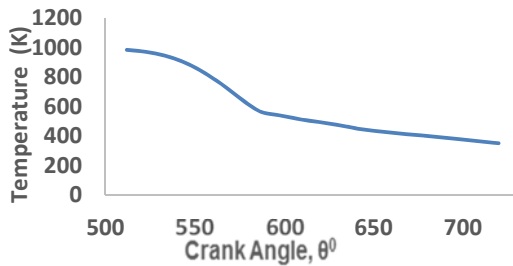**Fig.11 P-θ Curve for Exhaust Stroke**

Fig.12 T-θ Curve for Exhaust Stroke

6. Full Cycle

Fig. 13 shows the variation of pressure with volume for the full cycle. Area under the curve gives the work done and thereby power output of engine. The indicated power calculated by data obtained from the simulation is 2.3 kW @3600 rpm for the Producer gas as a fuel. Thermal efficiency found to be 28.19 % with Specific fuel consumption 2.62 kg/kWh and mean effective pressure found to be 6.7 bar. Fig. 14 T-θ in fig. 14 shows high temperature region where heat loss from cylinder will be more.
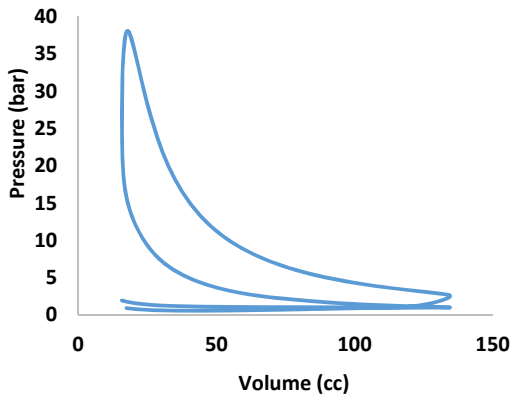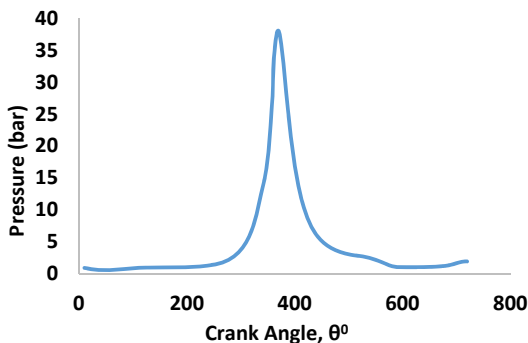

Fig.13 P-θ Curve for full Cycle
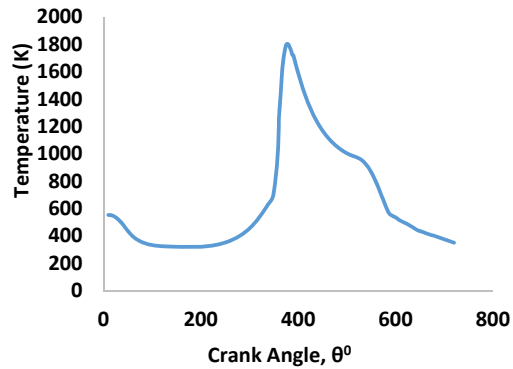

Fig.14 T-θ Curve for full Cycle

Fig.15 P-V Curve for full Cycle

V. VALIDATION OF SIMULATION RESULTS

As per the specifications given in the manual of Honda GX-120 engine the net power is 2.6 kW @3600 rpm for the gasoline. The indicated power calculated by data obtained from the simulation is 2.3 kW @3600 rpm with thermal efficiency 28.19 % for the Producer gas as a fuel, which shows the relatively reduction in power and thermal efficiency 11.538 % and 5.71 % respectively as compared to gasoline. The literature clearly indicates that the engine offers 15-30 % power de-rating and 3-10 % reduction in thermal efficiency as that of gasoline [7], [9] and thus looking to this fact present simulation may be treated as adequately validated.

VI. CONCLUSION

- Peak pressure and temperature produced in combustion is 38 bar and 1809 K.
- The indicated power calculated by data obtained from the simulation is 2.3 kW @ 3600 rpm. These simulation results are quite in tune with Honda GX-120 engine power output considering the fact that there exist the relative de-rating of engine by 15-30 % with Producer gas as a fuel.
- Thermal efficiency found to be 28.19 % which is relatively de-rated by 5.7 % compared to gasoline as fuel.

REFERENCES

1. http://en.wikipedia.org/wiki/Electricity_sector_in_India.
2. www.mospi.gov.in
3. http://www.mnre.gov.in/

MATHEMATICAL MODELING ON DROPWISE CONDENSATION

[1]Mr.Shivaji S.Parihar, [2]Prof. Prashnat T.Borlepwar

[1,2]Mechanical Department,Maharashtra Institute Of Technology,Aurangabad, M.S. India

Abstract:-The phenomenon of dropwise condensation, in which the condensate forms into drops rather than covering the entire cooling surface with a continuous film.Dropwise condensation produces heat transfer coefficients as much as 2 to 10 times greater than those produced by film wise condensation. Hence dropwise condensation is always desirable as it is more effective method of heat transfer than filmwise condensation.Dropwise condensation can be promoted by applying (i) Suitable organic promoter (ii) Thin layer of special metal (iii) Coating with polymer film on condenser surface. Due to successful application of dropwise condensation in small scale industry compound metal films are considerable.Special treatment like chrome plating on condenser surface is required for dropwise condensation.Higly polished surfaces also practice dropwise condensation.A overall heat transfer coefficient model is to be developed for dropwise condensation based on following two parameters.

    (i)   Plating thickness of condenser surface
    (ii)   Surface finishing of plated material.

Correlations for variation of the overall heat transfer coefficient with above two parameters are to be calculated by keeping one as constant and other as a variable. Under Dropwise condensation laboratory conditions, some permanent-type coatings, e.g.,gold, silver,teflon have been found to be effective dropwise condensation promoters. However, the effective lives of some of these promoters have been short, possibly due to surface removal of the coating in service. Furthermore, the effectiveness of permanent type promoters in maintaining dropwise condensation is limited by their low thermal conductivity and the coating thickness.In effect of Condenser Surface with morer polish increased life of brass surface promoted as much as upto 4 times for finishes with numbers 3-0000 grades of emery paper.In experiments it is also noted that very clean and smooth surface actually caused filmwise condensation at first which later changes to dropwise condensation.

Keywords: Overall heat transfer coefficient, Plating Thickness, Surface finish**.**

I. INTRODUCTION

Whenever a saturated vapour comes in contact with lower temperature surface condensation occurs.There are mainly two mode of condensation processes known as film wise condensation and dropwise condensation. If condensate tends to wet the surface and there by forms a liquid film, then processes of condensation is known as film wise condensation & on the other hand if condensate does not tends to wet the surface, the condensate forms the droplets on the surface and every time fresh surface is exposed to the vapour. By specially treating the condensing surface the contact angle can be changed & the surface become 'non – wettable'.Very high heat transfer rate are reported in dropwise processes due to the good contact between the vapour and surface.[1] Condensation is the change of phase from the vapour state to the liquid or solid state.Condensation plays a major role in the heat rejection parts which generally involve pure substances. The random nucleation, growth and departure of droplets results in a certain size distribution of droplets on the condenser surface.[2] The drop size distribution and the heat transfer through the individual droplets must

be known in order to calculate the heat flux with dropwise condensation. Dropwise condensation has been obtained on these types of surface by one of three methods i) Coating the surface with certain chemical substances called promoters ii) Coating the surface with a solid hydrophobic non-metallic material iii) Coating the surface with a noble metal.The thickness of the promoter layer on the condensation surface also affects the type of condensation, if the layer is too thin filmwise condensation occurs whereas excessive amounts of promoter increases the wettability of the surface.[3]

II DROPWISE CONDENSATION

Fig.1 Dropwise Condensation

Dropwise condensation occur when saturated pure vapour comes in contact with the cold surface such has copper tube. When considering surface is contaminated with substance which prevents condensate from the wetting surface ,the vapour will condense in drops instead of a continuous film.Though dropwise condensation would be preferred to filmwise condensation yet it is extremely difficult to achieve or maintain it for long time because most surfaces becomes wetted after being exposed to condensing vapour over a period of time .Dropwise condensation can be obtained under control conditions with the help of certain additives to the condensate and various surfaces coatings but it is commercial viability has not yet been approved for this reason the condensing equipment in use is designed on the basis of filmwise &dropwise condensation.[4]The vapour starts condensing on a surface when the vapour saturation temperature is more than the surface temperature,.the temperature of the condensate formed on the surface is less than its saturation temperature and it becomes sub-cooled, more vapour will condensate on the exposed surface or on the previously formed condensate as the

temperature of the previous condensate is less than the saturation temperature of vapour.[6]

A) Effect of plating thickness :-

Experimentation to study the behavior of a 0.00025-inch thick film of teflon to promotion of dropwise condensation on a 112- inch 0.D. Aluminium tube. The tube was mounted horizontally and both the dropwise and filmwise condensations were studied. It is found that curves of heat transfer coefficients versus vapor to surface temperature drop in dropwise and filmwise condensation lowered as the temperature drop become large. This was caused by the rapid formation of drops which rend to blanket the condenser surface with liquid at high heat fluxes. It is also found that highest heat transfer coefficients were obtained with thinnest teflon film because of the high thermal resistance of teflon. A teflon film thickness of 0.00025-inch provided 12.5 times as thermal resistance as the 0.02-inch thick aluninun wall of the condenser tube and about 3 times more than the condensIng film itself. This shows thar the thickness of the reflon film is an i:nportant parameter and it should be kept at a minimum to imorove the overall perforrance of the tef lon coated condenser tubes. [7]

B) Effect of Surface Roughness :-

Experimentation on dropwise condensation shows that highly polished surfaces produces dropwise condensation in absence of oil or fatty acids. On the other hand filmwise condensation can occur on very rough or very foul surfaces.Polish surface also affect the life of a brass surface..The basic mechanism of maintenance of dropwise condensation in the fact that the condenser surface should be nonwettable to the condensing vapor. All surface treatment, including application

of dropwise preorders, which will cause the surface to become non wettable will be effective in promoting dropwise condensation. Therefore it becomes apparent that the nature of the metal surface and material determines to some extent if a given promoter will be successful in promotion of dropwise condensation The use of different promorers on the same metal surface caused dropwise condensation fordifferent durations in time.It is noted that using- a mixture of oleic acid and light lubricating oil of a promoter on the surfaces of mirror smooth chrome-plated copper

and No 6J emery paper treated stainless steel, the useful promoter life for chrome-plated copper was twice as long as for stainless steel. It is also found that a promoter of some sort was necessary for dropwise condensation that highly polished surface alone will not cause dropwise condensation.[7]

III MATHEMATICAL ANALYSIS

A) Effect of Plating Thickness

In dropwise condensation is modeled including the effect of substrate material. Differentials equations are obtained for temperature distribution in the substrate and the droplet. Since analytical solution of the differential equation system is quite complicated by the known methods, no attempt is made to solve these equations analytically. Instead of solving the differential equations of the drop and the substrate simultaneously, the diffusion equation of the droplet is replaced by the equivalent thermal resistances and these resistances are used as boundary condition for the diffusion equation for the substrate material. Temperature distribution in the substrate material is obtained with finite difference method and the calculations are performed for different substrate materials and for various drop radii. Heat transfer and heat flux are calculated through a single droplet with the use of temperature distribution, then total heat transfer and flux is obtained by integrating the heat transfer through a single drop for the entire drop population. Finally heat transfer coefficient for dropwise condensation is determined by using the total heat flux and average surface temperature of the drop to substrate interface. Previous analytical and theoretical models of dropwise condensation used expressions for the heat transfer through single droplets of specific sizes and then the total heat transfer is determined by integrating over the distribution of sizes. Such an analysis will also be followed here. [6] Following assumptions are made in the analysis of this study :

• The vapor is at uniform temperature.

• Heat transfer from vapor to substrate is carried out only by condensation.

• Substrate material, although it has a finite thickness in typical applications, will be assumed to be a semi-infinite body since its thickness is considerably large for the majority of the droplets on the surface of condensation.

• The area between the droplets can be considered as thermally insulated.

We will first find the heat transfer coefficient inside the condenser under test.for this properties of water are taken at the bulk mean temperature of water e.g. (Twi + Two)/2 where Twi and Two are water inlet & outlet temperature. Following properties are required:

where g = acceleration due to gravity =9.8 m/sec2 =1.27 × 108 m/hr2

L = Length of condenser =160 mm

Overall heat transfer coefficient (U) can be calculated as

$1/U = [1/hi + Di/Do \times 1/ho] \times 4.1868/3600$ KW/ m²-K - ----------------------------------(1)

Where hi = Inside heat transfer coefficient.

ho = Outside heat transfer coefficient.

Di = Inside diam. Of wall.

Do= Outside diam. of wall.

In order to increase U, ho should be increased

$ho = 0.943[\Lambda \times \zeta^2 \times g \times k^3 / (Ts – Tw) \mu \times L]^{0.25}$

Where Λ = Heat of evaporation at B.M.T.(Bulk Mean Temp)

ζ = Density of water at B.M.T.

μ = Dynamic viscosity at B.M.T.

Consider a vertical plate of height L and width b maintained at a constant temperature Ts that is exposed to vapor at the saturation temperature Tsat. The downward direction is taken as the positive x-direction with the origin placed at the top of the plate where condensation initiates, as shown in Figure 2. The surface temperature is below the saturation temperature (Ts<Tsat) and thus the vapor condenses on the surface. The liquid film flows downward under the influence of gravity. The plating thickness δ and thus the mass flow rate of the condensate increases with x as a result of continued condensation on the existing film. Then heat transfer from the vapor to the plate must occur through the film, which offers resistance to heat transfer. Obviously the thicker the plating, the larger its thermal resistance and thus the lower the rate of heat transfer.The analytical relation for the heat transfer coefficient in film

condensation on a vertical plate described above was first developed by Nusselt in 1916. [8]

Then Newton's second law of motion for the volume element shown in Figure 2 in the vertical x-direction can be written as
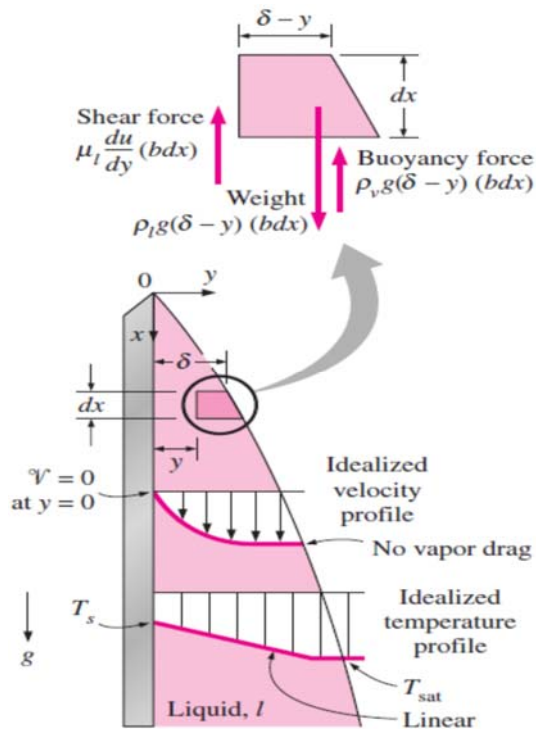
Fig.2 Condensate on vertical plate
Fig.2 The volume element of condensate on a vertical plate considered
In Nusselt's analysis.

$$\sum Fx = ma_x = 0$$

Since the acceleration of the fluid is zero. Noting that the only force acting
downward is the weight of the liquid element, and the forces acting upward are the viscous shear (or fluid friction) force at the left and the buoyancy
force, the force balance on the volume element becomes

$$F_{downward\downarrow} = F_{upward\uparrow}$$

Weight= viscous shear force + Buoyancy force

$$\rho_l g(\delta - y)(bdx) = \mu_l \, du/dy \, (bdx) + \rho_v g(\delta - y)(bdx)$$

Canceling the plate width b and solving for du/dy gives

$$\frac{du}{dy} = g(\rho l - \rho v)g(\delta - y)/\mu l$$

Integrating from y=0 where u=0 (because of the no-slip boundary condition)

To y =y where u=u(y) gives

$$U(y) = \frac{g(\rho l - \rho v)g}{\mu l}$$

$$u(y) = \frac{g(\rho l - \rho v)g}{\mu l}\left(y\delta - \frac{y2}{2}\right) \qquad (2)$$

The mass flow rate of the condensate at a location x, where the boundary layer thickness is δ ,is determined from

$$M(x) \qquad = \int_A \rho l u(y)dA = \int_{y=0}^{\delta} \rho l u(y)bdy$$

(3)

Substituting the u(y) relation from Equation 1 into Eq. 2 gives $\frac{m(x) = gb\rho l(\rho l - \rho v)\delta^3}{3\mu l}$ (4)

Whose derivative with respect to x is

$$\frac{dm}{dx} = \frac{gb\rho l(\rho l - \rho v)\delta^2}{\mu l}\frac{d\delta}{dx} \qquad (5)$$

which represents the rate of condensation of vapor over a vertical distance dx. The rate of heat transfer from the vapor to the plate through the liquid film is simply equal to the heat released as the vapor is condensed and is expressed as

$$dQ = hfg \, dm = k_l \, (bdx) \frac{Tsat - Ts}{\delta} \rightarrow$$

$$\frac{dm}{dx} = \frac{k_l b}{h_{fg}} \frac{Tsat - Ts}{\delta} \qquad (6)$$

Equating Eqs. 4 and 5 for dm· /dx to each other and separating the variables give

$$\delta^3 d\delta = \frac{\mu_l\, k_l (T_{sat} - T_s)}{g\rho_l (\rho_l - \rho_v)\, h_{fg}} dx$$

(7)

Integrating from x=0 where δ =0 (the top of the plate) to x=x where

$$\delta = \delta(x)$$

the liquid film thickness at any location x is determined to be

$$\delta(x) = \left[\frac{4\, \mu l\, kl\, (Tsat - Ts)\, x}{g\rho_l (\rho_l - \rho_v)\, h_{fg}}\right]^{1\backslash 4}$$

(8)

The heat transfer rate from the vapor to the plate at a location x can be
expressed as

$$q_x = h_x (Tsat - Ts) = k_l\, \frac{Tsat - Ts}{\delta} \quad \rightarrow \quad h_x = \frac{kl}{\delta(x)}$$

(9)

Substituting the $\delta(x)$ expression from Eq. 7, the local heat transfer coefficient hxis determined to be

$1/U = [1/hi + Di/Do \times 1/ho + \partial/K] \times 4.1868/3600$ KW/ m²-K   (10)

B) Effect of Surface Roughness :-

In conclusion, we have shown that for relatively low humidity capillary forces are present in the case of smooth surfaces, and surpasses in magnitude any dispersion and electrostatic forces. In addition, an enormous decrease in the capillary force was observed by increasing the roughness amplitude a few nanometers in the range ~1-10 nm. Considering the rapid fall off in the capillary force and the two limits (a smooth limit where the whole surface contribute to the capillary force, and a rough limit where only a single or a few asperities contribute), the crossover regime might in turn depend on the contact angle and any lateral roughness features. Both could be an intersecting direction for further study of this phenomenon in the design MEMS (micro electromechanical systems) if stiction poses a problem. The total adhesion force can be divided into a capillary force and an interfacial tension force due to surface tension acting tangentially to the interface along the contact line with the solid body.The Laplace pressure, while ignoring contributions from surface tension.

$Fup = 4\pi\, \nu\, Rh\, Cos\Theta.$ (11)

Where ν = Liquid vapour pressure,

Rs = Surface roughness,

Θ = contact angle of vapour with condenser surface.

For the contact angle of water onto Au surfaces we obtain for Θ =70°,Rs=50μm, Fup=1.5X10⁴ nN It appears that the smooth limit is reached for the Au/mica film. For the roughest films the values found are up to ten times higher than that of a single asperity, indicating a capillary interaction of a multitude of asperities

For a increase in 100% roughness, capillary force reduces up to 1/10 times applicable only after 60% rise in roughness. [5]This will effect condensation in the same manner. From this result alongwith equation (1) and (11) we can write as

$1/U = Rm/10[1/hi + Di/Do \times 1/ho] \times 4.1868/3600$ KW/ m²-K - ---------------------------------- (I)

Where Rm= Number of times of original roughness value.

IV. CONCLUSION

In this paper through mathematical mode finally observed that the heat transfer coefficient (h W/m2K) associated with dropwise condensation is decreases with increase in plating thickness of coatings. It can be calculated depending on the formula with respect to plating thickness. The drop wise condensation is also affected by roughness of coated surface. In mathematical mode finally it is observed that the heat transfer coefficient (h W/m2K) associated with dropwise condensation is decreases with increase in roughness of coated plate. Plating thickness of coatings. It can be calculated depending on the formula with respect to plating thickness.

And also this paper suggest that whenever the requirement of condensation is more ,the surface should be with minimum plating thickness and with minimum value of surface roughness.

REFERENCES

[1] Saurabh pandey, Dropwise and filmwise condensation, International Journal of Scientific & Engineering Research, Volume 3, Issue 4, April-2012 ISSN 2229-5518.

[2] M. Rama Narasimha Reddy, Dr M.Yohan, K.Harshavardhan Reddy, Heat transfer coefficient through dropwise and filmwise condensation apparatus, International Journal of Scientific and Research Publications, Volume 2, Issue 12, December 2012 1 ISSN 2250-3153

[3] Gagan Deep Bansal, Sameer Khandekar, and K. Muralidhar, Measurement of heat transfer during dropwise condensation of water on polyethylene, Nanoscale and Microscale Thermophysical Engineering, 13: 184–201, 2009.

[4]Dr.S.Alec   Watson,Nickel   Development Institute,Watson   Consultancy Services,Solihull,England, 1989.

[5] P.J. van Zwol, G. Palasantzas* and J. Th. M. De Hosson, Influence of random roughness on the adhesion between metal surfaces due to capillary condensation, Applied Physics letters 91, 101905 _2007.

[6] Cecil E. Kirby, Promotion of dropwise condensation of ethyl alcohol,methyl alcohol and a roethylene,National Aeronautics and Space Administration Washington,D.C.July 1971.

[7] S. C. Garg, Ph.D., Technical Note N-1041The effect of coating and surfaces on dropwise co ndensation July 1969

[8]Yunus A.Cengel,Reference book on Heat Transfer.

A REVIEW PAPER ON TRIBOLOGICAL AND MECHANICAL PROPERTIES OF ALUMINIUM METAL MATRIX COMPOSITES MANUFACTURED BY DIFFERENT ROUTE

Zeeshan Ahmad[1], Dr. Sabah Khan[2]
[1]Research Scholar, Mechanical Department, JMI, New Delhi,
[2]Asst. Professor, Mechanical Department, JMI, New Delhi,

Abstract- Particulate reinforced aluminium matrix composites (AMCs) are attractive metal matrix composite (MMC) materials due to their strength, ductility and toughness as well as their ability to be processed by conventional methods. There are many techniques used to manufacture metal matrix composites, but casting and powder metallurgy are extensively used to manufacture the composites. The powder metallurgy technique is more cost effective than the casting methods, but it cannot be used for the production of complex shapes. Compared with powder metallurgy, casting which involves the stirring of the particles into melt has some advantages: better matrix–particle bonding, easier control of matrix structure, low cost, simplicity, a nearer net shape can be produced and there is a wide selection of materials that can be used in this method. Recently it is shown that aluminium metal matrix composites have superior wear resistance and mechanical properties. This review paper is aimed to summarize tribological and mechanical properties of aluminium alloy matrix composite fabricated by different casting techniques.

Keywords: Aluminium Alloys Matrix, Fabrication techniques, tribological and mechanical properties

I. INTRODUCTION

Aluminum alloys reinforced with particles reiforcement are being extensively used in various field of life, especially in aerospace and automobile industries, because of good thermal stability and excellent specific strength [1,2]. Low weight aluminum alloys lead to reduction of weight resulting in considerable economic advantages [3-6]. Wear behavior of particulate aluminum matrix composites has been extensively studied due to their high secondary workability and superior wear resistance compared to unreinforced metal alloys [7,8]. Aluminium matrix materials can be reinforced with various oxides, carbides, nitrides and borides. SiC and Al_2O_3 are the most common reinforcing material in AMC's limited research has been conducted on B_4C reinforced AMC due to the higher cost of B_4C [11-17]. The ceramic particulate reinforced composites exhibit improved abrasion resistance [18]. They find applications as cylinder blocks, pistons, piston insert rings, brake disks and calipers [19]. The strength of these composites is proportional to the percentage volume and fineness of the reinforced particles [20]. These ceramic particulate reinforced Al-alloy composites led to a new generation tailorable engineering materials with improved specific properties [21]. The structure and the properties of these composites are controlled by the type and size

of the reinforcement and also the nature of bonding [22-24].

II. Manufacturing Techniques

Metal matrix composites are manufactured using different techniques. These techniques can be classified into liquid phase processes (casting), liquid–solid processes (semi-solid forming) and solid-state processes or powder metallurgy [25, 26]. The powder metallurgy technique is widely used in the manufacture of particle MMCs and it is more cost effective than the casting methods. Compared with powder metallurgy, liquid processing which involves the stirring of the particles into melt has some advantages: better matrix–particle bonding, easier control of matrix structure, low cost, simplicity, a nearer net shape can be produced and there is a wide selection of materials that can be used in this method. However, the casting process has two main problems: first, the reinforcement particles are generally not wetted by the liquid metal matrix, and second, the particles tend to sink or float according to their density relative to the matrix liquid. [27,28].

Semisolid forming has many advantages, such as complex shapes can be formed with some reduction in forming steps and with near net shaping capabilities, less energy consumption, less solidification shrinkage, prolonged die life, good filling of the die and improved mechanical properties [30,31]. The production of raw material for semisolid processing requires specialized techniques such as mechanical stirring, inductive electromagnetic stirring and the cooling slope method. Of all the techniques employed to produce thixotropic microstructure feedstock, the cooling slope casting method is particularly attractive because it is simple, requires a very low amount of equipment and is therefore cost effective [29-31].

Baradeswaran & A. Elaya Peruma [2014] investigated the influence of graphite on the wear behavior of Al 7075/ Al_2O_3/5 wt.% graphite hybrid composite. The composites were fabricated using liquid metallurgy route. Ceramic particles along with solid lubricating materials were incorporated into aluminium alloy matrix to accomplish reduction in both wear resistance and coefficient of friction. The mechanical and tribological properties of the Al 7075–Al_2O_3–graphite hybrid composites were found to be increased by increased weight percentage of ceramic phase as shown in fig(1). The wear properties of the hybrid composites containing graphite exhibited the superior wear-resistance properties [32]. Rao R. N. et al [2013] studied dry sliding wear maps for aluminium matrix composite fabricated by stir casting technique and examined under specific applied load and sliding speed [33]. Taufik R. S. and Sulaiman S. [2013] presented the development of thermal expansion model for casted aluminium silicon carbide [34]. F. Toptan et al. [2013] investigated corrosion behavior of Al-Si-Cu alloy matrix composites reinforced with B4C particulates [35].

M.B. Karamıs et al. [2012] Studied a number of metal matrix composites were manufactured to determine their tribological properties. AA2124 matrix material, reinforced by SiC, B_4C or Al_2O_3 (of different particle sizes), was used for manufacturing by powder metallurgy. The specifics wear rates of the composite reinforced with 10% volume fraction of B_4C or SiC were each lower than that of the GGG40 cam material. While the composites having 30% volume fraction of 20 mm SiC gave the best wear performance, the sample with B_4C showed the best performance at 10% volume fraction as shown in fig. 2, [36]. D. Cree & M.pugh [2011] investigated dry sliding wear and friction behaviors of A356 aluminum alloy and a hybrid composite of A356 aluminum alloy and silicon carbide foam in the form of an interpenetrating phase composite were evaluated using a ball-on-disk apparatus at ambient conditions[37]. Yusuf Shahin [2010] investigated behaviour aluminium alloy matrix reinforced with 15 wt% SiC particles were prepared by powder metallurgy (PM) method. Table 1 summarizes the investigation done by various research

groups to study effect of different parameters as per fabrication techniques on tribological and mechanical properties for Aluminium alloys composite [38].
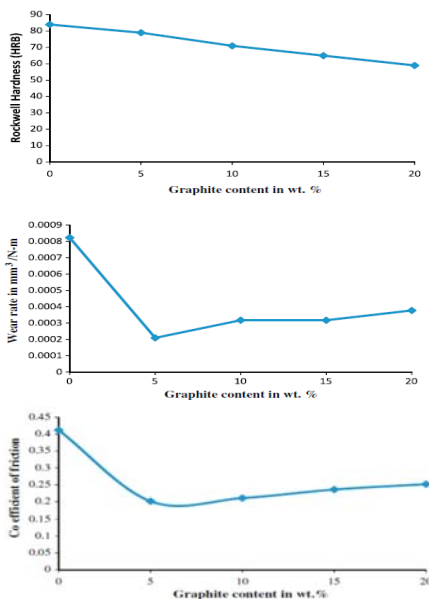
Fig(1): (a). Hardness with varying graphite content (b). Wear rate with varying graphite content(c). coefficient of friction with varying graphite content.
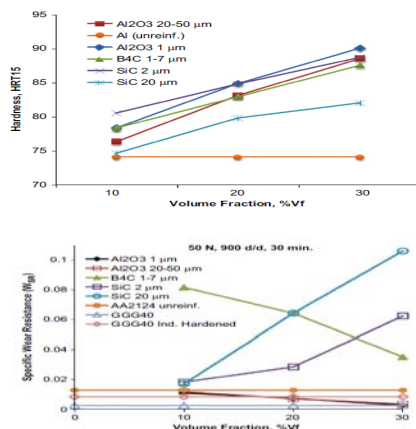
Fig.2: (a). The variation of the composite hardness versus the volume fraction of reinforcement (b). The variation of specific wear with reinforcing particle volume fraction

Table1: Review of Aluminium alloys matrix composites properties.

Author/Group	Fabrication Technique	Parameter	Tribological Properties	Mechanical Properties
A. Baradeswar A. Baradeswaran & A. Elaya Peruma [2014] [39]	Liquid casting	Load: 20-60N Speed: 0.6-1.0 m/s	Wear: .0023-.0034 mm³/m	Hardness: 115-134 MPa Ultimate Strength: 215-240 MPa Flexural Strength: 330-
				440 MPa
Yuhai Dou et al. [2014] [40]	Casting	Slidng time:30-120 min Load: 10-40 N Slidng velocity: 60-240m Heat Treatment	Mass loss: 1.6-16.5 mg COF: 0.55-0.59	Hardness: 108-135HB

Gheorghe Iacob et al [2014] [41]	Powder Metallugy		Morphological changes	Hardnrss: 150-390 HV
M. Lieblich et al. [2014] [42]	powder met allugy	load: 42 &140N Varying Mixing method	COF: 0.18-0.73 Volume loss: 11-23mm^3	Hardness: 1.08-1.47HV

Sachin Vijay Muley et al. [2014][43]	Ulionrasonic Vibrations	Load: 500-1500g Sliding Distance:0-3500 Sliding Speed: 1 m/s	Microstructural Analysis Wear: .0026-.014mm^3/m	Compressive Strength: 0-410 MPa Compressive Strain: 0-0.23
Faiz Ahmad et al. [2013] [44]	Casting	Load: 0-100N Sliding Distance:0-1000m	Weight loss: 0.0043-0.103gm COF: 0.16-0.32 Microstructural Analysis	Nil

K.S. Alhawari et al. [2013] [45]	Semi solid processing technique & Stirr Casting	Sliding Distance:0-10Km	Wear: 0.0000 28-0.00019 mm3/m Microstructural Analysis	Hardness: 62-74BHN
G. Elango &B.K. Raghunath [2013] [46]	Casting	Load: 30-50N Sliding Distance:0-500m	Wear: 0.014-0.04mm3/m 0.46-0.7 Microstructural Analysis	Nil
J. Gandra et al. [2013] [47]	Friction surfacing	Sliding Distance: 0-300m	Wear: 0.042-0.076mg/m COF: 0.25-0.56 Microstructural Analysis	Hardness: 65-108 HV
Anand Kumar et al [2013] [48]	Casting	Load: 10-30N Sliding Distance:1000-2000m	COF: 0.41-0.5 Weight loss: 32-69mg Microstructural Analysis	Nil

Author	Method	Parameters	Results	Properties
Ravinder Kumar and Suresh Dhiman [2013] [49]	Stir casting	Speed: 2-6m/s, Sliding Distance: 1000-5000m, Load: 20-60N	Wear:.000042-.000465 mm³/Nm, Microstructural Analysis	Nil
C.A. Leon-Patino et al [2012] [50]	Directional Infiltration	Speed: 0.3-0.9 m/s, Sliding Distance: 0-2000m, Load: 103N	Wear: 0.0000014-.0076mm³/m, Microstructural Analysis	Hardness: 84-290 HV
P. Ravindran et al. [2013] [51]	Powder metallugy	Speed: 0-3.0 m/s, Sliding Distance: 500-3000m, Load: 0-30N	Weight loss: 0.0012-0.021 gm, COF: 0.02-0.3	Hardness: 52-63 BHN
M. Uthayakumar et al. [2013] [52]	Stir Casting	Speed: 0-6.0 m/s, Load: 0-100N, Sliding Distance: 0-4000m	COF: 0.28-0.7, Wear: .000025-0.00027 mm3/m	Nil
			Temperature: 32-36C	
F. Toptan et al. [2012] [53]	Squeeze Casting	Speed: 0.02 & 0.03 m/s, Load: 20 & 40N, Sliding Distance: 200 & 400m	COF: 0.48-0.98, Wear: 0.00650-0.03650 mg/m	Hardness: 119-135HV
Heguo Zhu et al. [2012] [54]	Powder metallugy	Speed: 0.4-0.75 m/s, Load: 20-50N, Sliding Distance: 0-200m	Wear: 0.000043-0.000095g/Nm, COF: 0.067-0.534	Hardness: 60-77.2HV, Ultimate Strength: 190-215Mpa

III. Conclusion

There are exciting opportunities for producing exceptionally strong, light weight, wear resistant aluminium matrix composites with acceptable ductility by different fabrication

route. From the various fabrication process discussed in this paper, mechanical stirring method, it is extremely difficult to distribute and disperse particles uniformly in aluminium metal alloy due to their large surface and volume ratio due to and their low wettability. The hardness and wear resistance of the aluminium allos matrix composite fabricated by cooling slop casting were found to be higher than those of aluminium matrix composite fabricated by using stirring. Powder metallurgy is the branch with a remarkable development for the fabrication of aluminium alloys matrix in recent years due its ability to give more uniform dispersions. Parts produced by this technology require minimal finishing, and have technical/economic advantages which made them very attractive. It is also possible to deposit composite layers by friction surfacing in aluminium based alloys. Multi layering enable to tailoring coating composition in order to achieve pre defined gradient. The multilayer composite coatings present a sound bonding to substrate and between layers with exception of edges.

References

[1].

aluminium composite: review and discussion," Wear, vol. 189, pp. 1-19, 1995.

[2]. S.C.Simon, M.L. McMillan, "Automotive tribology overview of current advances and challenges for the future," Tribol Int, vol. 37, pp.517–36, 2004.

[3]. V.M. Kevorkijan, "Aluminum composites for automotive applications: a global perspective," JOM, vol. 8, pp. 51-54, 1999.

[4]. A. Mazahery, M.O. Shabani, " Nano-sized silicon carbide reinforced commercial casting aluminum alloy matrix: Experimental and novel modeling evaluation," Powder Technology, vol. 217, pp. 558-565, 2012.

[5]. A. Mazahery, M. Shabani, "Characterization of wear mechanisms in sintered Fe-1.5 Wt % Cu alloys," Archives of Metallurgy and Materials, vol. 57(1), pp.93-103, 2012.

[6]. N. Saheb et al., " Influence of Ti addition on wear properties of Al-Si eutectic alloys," Wear, vol. 249(8), pp.656-662, 2001.

[7]. N. Saheb et al., "Microstructure and hardness behaviours of Ti-containing Al-Si alloys. Philosophical Magazine A: Physics of Condensed Matter, Structure, Defects and Mechanical Properties, vol. 82(4), pp. 803-808, 2002.

[8]. N. Chawla, K.K., Chawla, "MetalMatrixComposites," Springer, pp. 67-68, 2006.

[9]. A. P. Sannino, H.J. Rack, "Dry sliding wear of disc continuously reinforced

[10]. K. Tokaji, "Fatigue and fracture of engineering materials and structures," vol. 28, pp. 539-545, 2005.

[11]. K.B. Lee et al, "Metallurgical and materials transactions A- Physical metallurgy and materials science," vol. A4-32, pp. 1007-1018, 2001.

[12]. I. Kerti, F. Toptan, " Materials letters," vol. 62, PP. 1215-1218, 2008.

[13]. R. Ipek, "Journal of materials processing technology," vol. 162-163, PP. 71-75, 2005.

[14]. F. Bedir, " Materials and designs," vol.62, pp. 1238-1244, 2008.

[15]. A. Kalkanli, S. Yilmaz, "Materials and design," vol. 29, pp. 775-780, 2009.

[16]. Kerti I., F. Toptan, "Materials letters," vol. 62, pp. 3795-3800, 2008.

[17]. S. Kassim Al-Rubaie, N.Humberto Yoshimura, and Jose Daniel Biasoli de Mello, "Two body abrasive wear of Al–SiC composites," Wear 233–235, pp. 444–454 , 1999.

[18]. L. Ceschini, C. Bosi, A. Casagrande, and G.L. Garagnani, "Effect of thermal treatment and recycling on the tribological behaviour of an AlSiMg–SiCp composite," Wear 251, pp. 1377–1385, 2001.

[19]. Bermudez M.D., Martinez-Nicolas G., Carrion F.J., Martinez-Mateo

I., Rodriguez J.A., Herrera E.J., "Dry and lubricated wear resistance of mechanically-alloyed aluminum-base sintered composites," Wear, 248, pp. 178–186, 2001.

[20].   H. Y. Sohn, S. PalDey, "Synthesis of ultrafine particles and thin films of Ni4Mo by the vapor-phase hydrogen coreduction of the constituent metal chlorides," Materials Science and Engineering A, vol. 247,1-2, pp. 165-172, 1998.

[21].   N. Wang, Z. Wang, G.C. Weatherly, "Formation of Magnesium Aluminate (spinel) in Cast SiC Particulate-Reinforced Al(A356) Metal Matrix Composites," Metallurgical and Materials Transactions A, vol. 23, pp. 1423–1430, 1992.

[22].   H. Ribes, M. Suery, G. L. Esperance, J.G. Legoux, "Microscopic examination of the interface region in 6061-Al/SiC composites reinforced with as-received and oxidized SiC particles," Metallurgical and Materials Transactions A, vol. 21, pp. 2489–2496, 1999.

[23].   S.K. Thakur, B.K. Dhindaw, "The influence of interfacial characteristics between SiCp and Mg/Al metal matrix on wear, coefficient of friction and microhardness," Wear 247, pp. 191–201, 2001.

[24].   S. Amirkhanlou, B. Niroumand, "Development of Al356/SiCp Cast Composites by Injection of SiCp Containing Composite Powders," Journal of Materials & Design, vol. 32, pp. 1895-1902, 2011.

[25].   S.A. Sajjadi. et al., "Fabrication of A356 composite reinforced with micro and nano Al2O3 particles by a developed compocasting method and study of its properties," Journal of Alloys and Compounds, vol. 511, pp. 226– 231, 2012.

[26].   C.G. Kang, S.W. Youn, "Mechanical properties of particulate reinforced metal matrix composites by

electromagnetic and mechanical stirring and reheating process for thixoforming," Journal of Materials Processing Technology, vol. 147, pp. 10–22, 2004.

[27].   Lin.et al., "Effects of Mg content on microstructure and mechanical properties of SiCp/Al-Mg composites fabricated by semi-solid stirring technique," Trans. Nonferrous Met. Soc. China, vol. 20, pp. 185-189, 2010.

[28].   M.Z. Omar et al., "Thixoforming of a high performance HP9/4/30 steel," Materials Science and Engineering A, vol. 395, pp. 53-61, 2005.

[29].   M.S. Salleh, M.Z. Omar, J. Syarif, M.N. Mohammed, K.S. Alhawary, "Thermodynamic simulation on thixoformability of aluminium alloys for semisolid metal processing," International Journal of Mathematics and computers in simulation, vol. 7(3), pp. 286-293, 2013.

[30].   M.N. Mohammed, M.Z. Omar, M.S Salleh, M.A. Zailani, K.S. Alhawari, "Joining Two Metals Via partial remelting Method," Journal of Asian Scientific Research, vol. 2(11), pp. 724-730, 2013.

[31].   T. Haga, S. Suzuki, "Casting of Aluminium Alloy Ingots for Thixoforming Using a Cooling Slope," Journal of Materials Processing Technology, vol. 118, pp. 169-172, 2001.

[32].   M.S. Salleh, M.Z. Omar, J. Syarif, , M.N. Mohammed, "An Overview of Semisolid Processing of Aluminium Alloys," ISRN Materials Science pp. 1-9, 2013.

[33].   A. Baradeswaran and A. E. Perumal, "Composites : Part B Study on mechanical and wear properties of Al 7075 / Al 2 O 3 / graphite hybrid composites," *Compos. Part B*, vol. 56, pp. 464–471, 2014.

[34].   R. N. Rao, S. Das, D. P. Mondal, G. Dixit, and S. L. T. Devi, "Tribology International Dry sliding wear maps for AA7010 (Al – Zn – Mg – Cu) aluminium

matrix composite," vol. 60, pp. 77–82, 2013.

[35]. R. S. Taufik and S. Sulaiman, "Thermal Expansion Model for Cast Aluminium Silicon Carbide," vol. 68, pp. 392–398, 2013.

[36]. F. Toptan, A. C. Alves, I. Kerti, E. Ariza, and L. A. Rocha, "Corrosion and tribocorrosion behaviour of Al – Si – Cu – Mg alloy and its composites reinforced with B 4 C particles in 0 . 05 M NaCl solution," *Wear*, vol. 306, no. 1–2, pp. 27–35, 2013.

[37]. M. B. Karamıs, "The effects of different ceramics size and volume fraction on wear behavior of Al matrix composites (for automobile cam material)," vol. 289, pp. 73–81, 2012.

[38]. D. Cree and M. Pugh, "Dry wear and friction properties of an A356 / SiC foam interpenetrating phase composite," vol. 272, pp. 88–96, 2011.

[39]. S. Yusuf, "Tribology International Abrasive wear behaviour of SiC / 2014 aluminium composite," vol. 43, pp. 939–943, 2014.

[40]. A. Baradeswaran and A. E. Perumal, "Composites : Part B Wear and mechanical characteristics of Al 7075 / graphite composites," *Compos. Part B*, vol. 56, pp. 472–476, 2014.

[41]. Y. Dou, Y. Liu, Y. Liu, Z. Xiong, and Q. Xia, "Friction and wear behaviors of B 4 C / 6061Al composite," *Mater. Des.*, vol. 60, pp. 669–677, 2014.

[42]. G. Iacob, V. G. Ghica, M. Buzatu, T. Buzatu, and M. Ionut, "Composites : Part B Studies on wear rate and micro-hardness of the Al / Al 2 O 3 / Gr hybrid composites produced via powder metallurgy," pp. 2–10, 2014.

[43]. M. Lieblich, J. Corrochano, J. Ibáñez, V. Vadillo, J. C. Walker, and W. M. Rainforth, "Subsurface modi fi cations in powder metallurgy aluminium alloy composites reinforced with intermetallic MoSi 2 particles under dry

sliding wear," *Wear*, vol. 309, no. 1–2, pp. 126–133, 2014.

[44]. S. V. Muley, S. P. Singh, P. Sinha, P. P. Bhingole, and G. P. Chaudhari, "Microstructural evolution in ultrasonically processed in situ AZ91 matrix composites and their mechanical and wear behavior," *Mater. Des.*, vol. 53, pp. 475–481, 2014.

[45]. F. Ahmad, S. H. J. Lo, M. Aslam, and A. Haziq, "Tribology Behaviour of Alumina Particles Reinforced Aluminium Matrix Composites and Brake Disc Materials," *Procedia Eng.*, vol. 68, pp. 674–680, 2013.

[46]. K. S. Alhawari, M. Z. Omar, M. J. Ghazali, M. S. Salleh, and M. N. Mohammed, "Wear Properties of A356 / Al 2 O 3 Metal Matrix Composites Produced by Semisolid Processing," *Procedia Eng.*, vol. 68, pp. 186–192, 2013.

[47]. G. Elango and B. K. Raghunath, "Tribological Behavior of Hybrid (LM25Al + SiC+ TiO2) Metal Matrix Composites," *Procedia Eng.*, vol. 64, pp. 671–680, 2013.

[48]. J. Gandra, P. Vigarinho, D. Pereira, R. M. Miranda, A. Velhinho, and P. Vilaça, "Wear characterization of functionally graded Al – SiC composite coatings produced by Friction Surfacing," *Mater. Des.*, vol. 52, pp. 373–383, 2013.

[49]. A. Kumar, M. M. Mahapatra, and P. K. Jha, "Modeling the abrasive wear characteristics of in-situ synthesized Al – 4 . 5 % Cu / TiC composites," *Wear*, vol. 306, no. 1–2, pp. 170–178, 2013.

[50]. R. Kumar and S. Dhiman, "A study of sliding wear behaviors of Al-7075 alloy and Al-7075 hybrid composite by response surface methodology analysis," *Mater. Des.*, vol. 50, pp. 351–359, 2013.

[51]. S. Me and C. A. Leo, "Dry sliding wear of gradient Al – Ni / SiC

composites," vol. 301, pp. 688–694, 2013.

[52]. P. Ravindran, K. Manisekar, P. Rathika, and P. Narayanasamy, "Tribological properties of powder metallurgy – Processed aluminium self lubricating hybrid composites with SiC additions," vol. 45, pp. 561–570, 2013.

[53]. M. Uthayakumar, S. Aravindan, and K. Rajkumar, "Wear performance of Al – SiC – B 4 C hybrid composites under dry sliding conditions," *Mater. Des.*, vol. 47, pp. 456–464, 2013. [1] F. Toptan, I. Kerti, and L. A. Rocha, "Reciprocal dry sliding wear behaviour of B 4 C p reinforced aluminium alloy matrix

composites," *Wear*, vol. 290–291, pp. 74–85, 2012.

[54]. X. Shi, J. Yao, Z. Xu, W. Zhai, S. Song, M. Wang, and Q. Zhang, "Tribological performance of TiAl matrix self-lubricating composites containing Ag , Ti 3 SiC 2 and BaF 2 / CaF 2 tested from room temperature to 600 ° C," *Mater. Des.*, vol. 53, pp. 620–633, 2014.

[55]. H. Zhu, C. Jar, J. Song, J. Zhou, J. Li, J. Xie, " High Temperture Dry Sliding Friction and Wear Behavior of Aluminium Matrix Composites ($Al_3Zr+\alpha$-Al_2O_3)/Al," Tribolody International, vol. 48, pp. 78-86, 2012.

4. S. N. Soid, Z. A. Zainal, "Combustion characteristics and optimization of CPG (compressed producer gas) in a constant volume combustion chamber," Energy, 73, pp. 59-69, May 2014.

5. E. Ramjee, K. Vijaya, Kumar Reddy, "Performance analysis of a 4-stroke SI engine using CNG as an alternative fuel,"Indian Journal of Science and Technology, vol. 4, No-7, pp. 0974-6846, Jully 2011.

6. Munde Gopal G., Dr. Dalu Rajendra S., "Review of Compressed Natural Gas as an Alternative Fuel for Spark Ignition Engine," IJEIT, vol. 2(6), pp. 2277-3754, Dec 2012.

7. Shashikantha *et al.,* "Development and Performance Analysis of a 15 kWe Producer Gas Operated SI Engine," Renewable Energy, Vol. 5, Part-II, pp. 835-837, 1994.

8. S. Dasappa, G, Sridhar, H. V. Sridhar, N. K. S. Rajan, P. J. Paul, A. Apasani, "Producer gas engine- Proponent of clean energy technology," 15th European Biomass Conference & Exihibition, 7-11, May 2007.

9. G. Sridhar, P. J. Paul and H. S. Mukunda,"Biomass derived producer gas as a reciprocating engine fuel-an experimental analysis," Biomass & Bioenergy, 21 pp. 61-72, 2001.

10. S. Hassan, F. Mohd Nor, Z. A. Zainal, M A Miskam, "Performance and emission characteristics of Supercharged Producer Gas -Diesel Dual Fuel engine," Journal of Applied Sciences 11(9), pp. 1606-1611, 2011.

11. N.R. Banapurmath , P. G. Tewari, V. S. Yaliwal, Satish Kambalimath, " Combustion characteristics of a 4-stroke CI engine operated on Honge oil, Neem and Rice Bran oils when directly injected and dual fuelled with producer gas induction," Renewable Energy, 33, pp. 2077-2083, Dec 2007**.**

12. P. D. Shah, "Optimisation of Design and performance Parameters of CNG Fuelled S.I. Engine," M.Tech Thesis, Sardar Vallabhbhai National Institute of Technology, Surat, 2014.

13. Heywood J. B.," Internal Combustion Engine Fundamentals," 1st Edition, Tata McGraw Hill Book Company, USA, 1988.

14. Shashikantha, Klose W. and Parikh P. P., "Producer-gas engine and dedicated Natural gas engine-Computer simulation for performance optimization," SAE, 1998.

15. Anand W. J. D., "Heat transfer in the cylinders of reciprocating Internal combustion engines," Proc. I. Mech. E., 177 (1963).

16. Junior Quarter Midgets Australia (JQMA) – Honda GX-120 Technical Manual.

SIMULATION OF MRAC BASED SPEED CONTROL OF BRUSHLESS DC MOTOR WITH LOW-RESOLUTION HALL-EFFECT SENSORS

[1]Gundra Sunil, [2]B.Rajasekhar

(M.E), Control Systems, ANITS College, M.E , Asst.Professor, ANITS College ,

Abstract—A novel speed estimation approach with control system based on model reference adaptive control (MRAC) is presented for low cost brushless dc motor drives with low-resolution hall sensors. The back EMF is usually used to estimate speed. But the estimation result is not accurate enough at low speeds because of the divided voltage of stator resistors and too small back EMF. Moreover, the stator resistor is always varying with the motor's temperature. A speed estimation algorithm based on MRAC was proposed to correct the speed error estimated by using back EMF. The proposed algorithm's most innovative feature is its adaptability to the entire speed range including low speeds and high speeds and temperature and different motors do not affect the accuracy of the estimation result. The effectiveness of the algorithm was verified through simulations and experiments.

Index Terms—Brushless dc motor, low-resolution hall sensor, model reference adaptive control, speed estimation

I. INTRODUCTION

Brushless dc (BLDC) motors are preferred as small horsepower control motors due to their high efficiency, silent operation, compact form, reliability, and low maintenance. However, the problems are encountered in these motor for variable speed operation over last decades continuing technology development in power semiconductors, microprocessors, adjustable speed drivers control schemes and permanent-magnet brushless electric motor production have been combined to enable reliable, cost-effective solution for a broad range of adjustable speed applications.

Due to the nonlinearity of the motor system, MRAC or model reference adaptive control which is one of a kind in adaptive control techniques is implemented. It is regarded as an adaptive servo system in which the desired performance is expressed in terms of reference model, which gives the desired response to a command signal. The nonlinearity occurs because the system transfer function varies or changes with the speed of the motor and the controller ought to be adaptive and robust for these changes.

Brushless dc (BLDC) motors usually use three or more Hall sensors to obtain rotor position and speed measurement. It would be necessary to inverse the time difference between two successive Hall sensor signals to obtain reliable speed measurement. Notice that there are only a few sensor signals available to the motor at low speeds. There may be 12 or 24 sensor pulses per round which depend on the number of poles. The sampling time, thus, becomes a variable according to the motor speed. These systems have uncertainty in a discrete time model and have a lot of difficulties to design speed regulators. Moreover, the sampling time is too long for speed regulations at low speeds. In order to make BLDC motors with low-resolution encoders work at very low speed and reduce the difficulty of speed regulators' design, several

methods have been developed to obtain high accurate speed measurement. These methods are commonly addressed as estimation methods. Instantaneous speed estimation based on a reduced-order disturbance torque observer provides the merits of simple structure and easy implementation [1]. But the high gain problem occurs in real application for mechanical noise and oscillation of system. In [2], a reduced-order extended Luenberger observer was proposed to reduce the sensitivity to the instantaneous speed estimation by the variation of the inertia moment. A computationally intensive Kalman filter is successfully used in dealing with velocity transients [3], but it is susceptible to the mismatch of parameters between the filter's model and the motor. In [4], a dual observer was proposed. The dual observer can estimate the rotor speed and position without time delay or bumps. All the observer-based methods share the feature of providing high accuracy of the speed estimation with satisfactory dynamic performance. But they suffer from the dependence on system parameters and need heavy computation [5]. A model free enhanced differentiator is proposed for improving velocity estimation at low speed [6], [7]. But the computation includes the fractional power of variables. Many other authors have suggested that accurate speed estimation can be obtained by using a low-resolution encoder, together with a position extrapolation algorithm, implemented in the drive control processor [8]–[12]. However, the estimation in [12] was dependent on the accuracy of position sensor and mechanical parameters. Hardware approaches involving a phase locked loop [13], [14] are feasible for a drive running at near-constant velocity, but may be unable to deal with transient velocity operation. For BLDC motors, the most popular speed estimation method may be based on back EMF. Operation rotor speeds determine the magnitude of the back EMF. At low speeds, the back EMF is not large enough to estimate the speed and position due to inverter and parameter nonlinearities. This paper presents a MRAC speed estimation algorithm by using the back EMF. The proposed algorithm can compensate the voltage occupied by the stator resistor adaptively at low speeds and is valid over the

entire speed range. Moreover, the parameters of the algorithm can be commonly used for different BLDC motors.

II. DESCRIPTION OF ESTIMATION ALGORITHM

A. Model of BLDC Motors

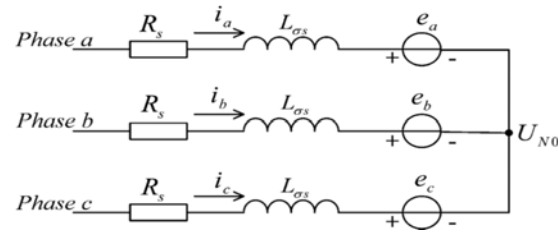The equivalent circuit of Y-connection BLDC motor is shown in Fig. 1 [15].

Fig.1.Equivalent circuit of a star connection BLDC motor.

A BLDC motor has three stator windings and permanent magnets on the rotor. Its voltage equation of three windings with phase variables is

$$
\begin{bmatrix} v_{as} \\ v_{bs} \\ v_{cs} \end{bmatrix} = \begin{bmatrix} R_s & 0 & 0 \\ 0 & R_s & 0 \\ 0 & 0 & R_s \end{bmatrix} \begin{bmatrix} i_a \\ i_b \\ i_c \end{bmatrix} +
$$
$$
\frac{d}{dt} \begin{bmatrix} L_{aa} & L_{ab} & L_{ac} \\ L_{ba} & L_{bb} & L_{bc} \\ L_{ca} & L_{cb} & L_{cc} \end{bmatrix} \begin{bmatrix} i_a \\ i_b \\ i_c \end{bmatrix} + \begin{bmatrix} e_a \\ e_b \\ e_c \end{bmatrix} \quad (1)
$$

and the electromagnetic torque equation is

$$
T_e = (e_a i_a + e_b i_b + e_c i_c) / \omega_m \quad (2)
$$

Where u_a, u_b and u_c are the terminal phase voltages with respect to the power ground, Rs is the stator resistance of phase windings, ia, ib and ic are phase current, $L\sigma s = Ls - Lm$ is the equivalent inductance of phase windings,Ls and Lm are self inductance and mutual inductance, respectively, ea, eb and ec are trapezoidal back EMFs, U_{N0} is the neutral point to ground voltage, and ω_m is the speed of the rotor. As a BLDC motor, there are only two phases which have current at the same time. For this analysis,

the current from phase *a to* phase *b* is considered. There are following equations:

$$\begin{cases} i_a = -i_b \\ i_c = 0 \\ e_a = -e_b \\ T_e = \dfrac{2e_a i_a}{\omega_m} \end{cases} \quad (3)$$

and the line voltage between phase *a* and phase *b* is

$$u_{ab} = u - u_b = 2R_s i_a + 2L\sigma s \frac{di_a}{dt} + 2e_a \quad (4)$$

Because the rotor of a BLDC motor is permanent magnet, the back EMFs are proportional to the electric speed of the rotor

$$e_a = -e_b = k_e \omega_r \quad (5)$$

where *ke* is back EMF coefficient and is a constant. According to (4) and (5), the speed of the rotor can be given as

$$\omega_m = (u_{ab} - 2R_s i_a - 2\sigma s \frac{di_a}{dt}) / p k_e \quad (6)$$

and $\omega_r = p\omega_m/2$, where *p* is the number of poles of a motor

Fig.2. Block diagram of the system

In stable condition or when *ia* is changed very slowly *dia/dt* ≈ 0. Then, (6) can be rewritten as

$$\omega_m = (u_{ab} - 2R_s i_a) / p k_e \quad (7)$$

B. Speed Estimation

The speed of the rotor can be calculated by voltage and current without Hall sensors with reference to (7). The line voltage u_{ab} can be estimated by pulse width modulation (PWM) signals. The phase current i_a can be sensed from hardware. R_s is a parameter of the motor and is proportional to the temperature. If the change of *Rs* is neglected, the estimated speed is very accurate especially at high speed but when a motor is working at low speed, the estimated speed is not accurate enough. It is mainly because the back EMF is too small comparing with R_s i_a. A small error of u_{ab} or *Rs ia* would lead to an inaccuracy of the estimated speed. *p* and k_e in (7) are constant for a known BLDC motor. But they are changed with different BLDC motors. Actually, *p* is usually on the plate of a motor and can be obtained easily. k_e, however, is seldom on the plate. Thus, there are two problems with the speed estimation based on the back EMF of BLDC motors. 1) The accuracy of the estimated speed is not enough at low speed and 2) *Rs* is not constant. It is varying by temperature. *p* and k_e are variables for different motors. Therefore, the algorithm based on (7) cannot be commonly used for different motors or in different conditions for the same motor.

C. Basic Idea

Our objective is to solve these two problems mentioned above, a speed estimation algorithm based on MRAC was proposed. Fig. 2 shows the block diagram of the speed control system with the proposed speed estimation algorithm. It consists of a power circuit and control circuits which perform following functions: PWM strategy, current control, current commutation, speed estimation, and speed control.

The main blocks of the speed estimation is a MRAC-based regulator. The speed estimated by the back EMF and the speed calculated by Hall sensors are the inputs of the regulator. The output of the regulator is a correction variable for
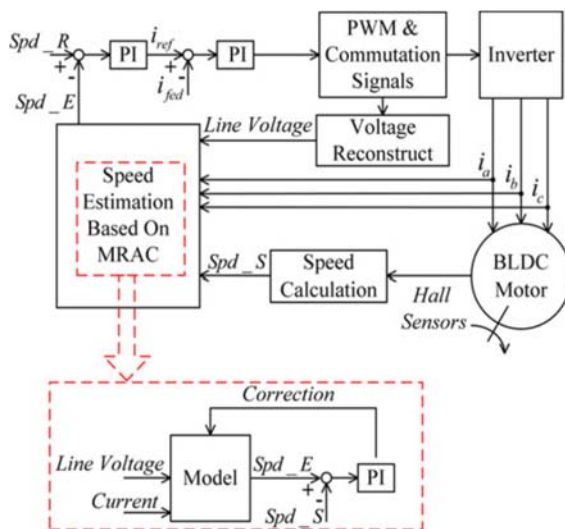
the estimated speed. *Spd_E* is the estimated speed. *Spd_S* is the calculated speed by Hall sensors. If *Spd_E* is not equal to *Spd_S*, a correction is given by the PI regulator and then, *Spd_E* is calculated again based on the proposed model. The reference current *i*ref is changed by the speed regulator. Through the current regulator, the output voltage of the inverter is being tuned and *Spd_S* is changed. In
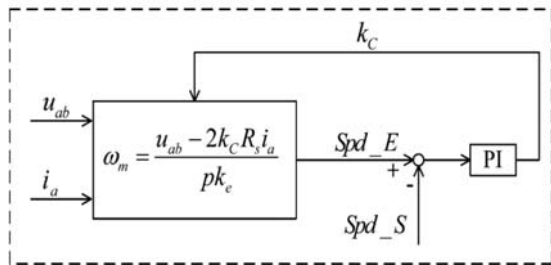

Fig3. Speed estimation algorithm considering the voltage compensation of stator resistor.

this way, the PI regulator used in the estimation Algorithm is always working until *Spd_E* equals to *Spd_S*.

The basic block diagram brushless dc motor as shown Fig.4.The brush less dc motor consist of four main parts power converter, permanent magnet-synchronous machine (PMSM) sensors and control algorithm. The power converter transforms power from the source to the PMSM which in turn converts electrical energy to mechanical energy.

One of the salient features of the brush less dc motor is the rotor position sensors, based on the rotor position and command signals which may be a torque
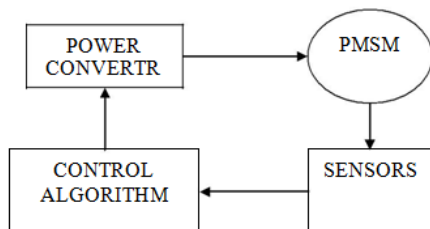

Fig.4 Basic Block Diagram of BLDC motor

command, voltage command, speed command and so on the control algorithms determine the gate signal to each semiconductor in the power electronic converter.

The structure of the control algorithms determines the type of the brush less dc motor of

which there are two main classes voltage source based drives and current source based drives. Both voltage source and current source based drive used with permanent magnet synchronous machine with either sinusoidal or non-sinusoidal back emf waveforms .Machine with sinusoidal back emf may be controlled so as to achieve nearly constant torque. However, machine with a non sinusoidal back emf offer reduces inverter sizes and reduces losses for the same power level.

The model reference adaptive system (MRAS) is one of the major approaches for adaptive control. The model reference adaptive system (MRAS) is one of many promising techniques employed in adaptive control. Among various types of adaptive system configuration, MRAS is important since it leads to relatively easy- to-implement systems with high speed of adaptation for a wide range of applications.

One of the most noted advantages of this type of adaptive system is its high speed of adaptation. This is due to the fact that a measurement of the difference between the outputs of the reference model and adjustable model is obtained directly by the comparison of the states (or outputs) of the reference model with   those
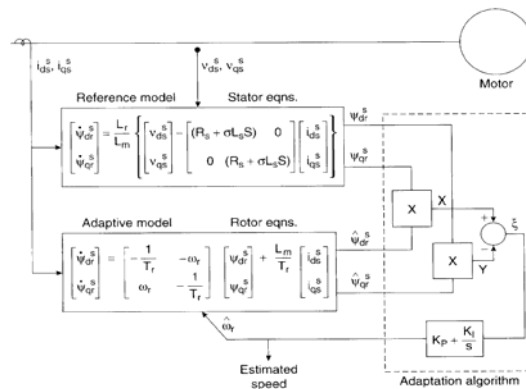

Fig 5 Basic Block Diagram of MRAS speed estimation

''reference model'' represents demanded of the adjustable system. The block dynamics of actual control loop. The block ''adjustable model'' has the same structure as the reference one, but with adjustable parameters instead of the unknown ones.

III.DESIGN OF ESTIMATION ALGORITHM
BASED ON MRAC

For this analysis, the current from phase a to phase b is considered.

A. Speed Estimation Algorithm

The inaccuracy of the low speed estimation is mainly because of the divided voltage of the stator resistor. So an estimation algorithm considering the voltage compensation of the stator resistor is presented firstly. It is shown in Fig. 3. The estimated speed is calculated by using (7). In Fig. 3, where *Rs* is not accurate or changed with the temperature, *Spd_E* will not be equal to *Spd_S*. Because *kc* affects *Spd_E* and *Spd_E* is the input of the speed PI regulator, the speed PI regulator will change the output voltage to compensate divided voltage of the stator resistor adaptively. *kc* is always tuning until *Spd_E* equals to *Spd_S.* Therefore, the control system including this proposed speed estimation algorithm can keep the accuracy of the estimated speed at very low speed. The 2*kcRs ia* not only needs the value of *Rs* but also needs the value of current. Actually the output of the PI regulator proposed in Fig. 3 can completely compensate the divided voltage of the stator resistor. Therefore, a simple algorithm is proposed in Fig. 6 the *vc* is the output of the PI regulator and 2*kcRs ia* is replaced by *vc* .

B. Algorithm Approach Considering Different Motors

For different motors, the value of *p* and *ke* may be changed. *p* could be easily obtained from the plate of a motor. However,. *ke* is seldom shown on the plate. Therefore, the initial value of *ke* may be inaccuracy.
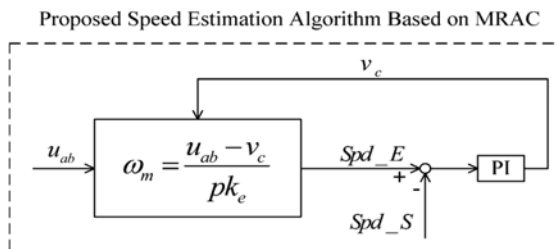

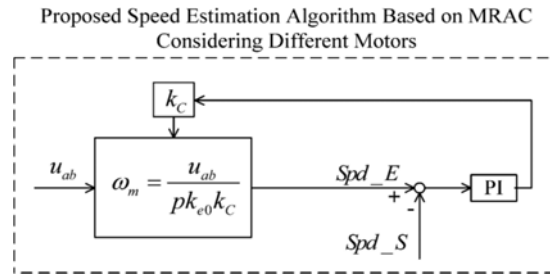Fig.6. Approach to simplify algorithm.

Fig 7. Estimation algorithm approach considering motors at high speed.

At high speed, the divided voltage of stator resistors can be neglected. The voltage on a motor is almost the back EMF. Then, referring to (7), an approach of the high speed estimated algorithm is proposed here.

$$\omega_m = u_{ab} / pk_e \qquad (8)$$

According to (8), *ke* produces great influence on the accuracy of the estimated result at high speeds. An approach of the high speed estimated algorithm was proposed based on Fig. 6. The block diagram is shown in Fig. 7. *ke*0 is the initial value of *ke* and *ke* = *ke*0*kC* . If *ke*0 is not accurate, the PI regulator will change the value of *kc* until *Spd_E* equals to *Spd_S*. In this way, the error of the estimated speed caused by the inaccuracy of *ke* is corrected by *kc* .

C. Speed Estimation Algorithm Considering Voltage Compensation and Different Motors

At low speed, the primary reason of the estimated inaccuracy is the effect of divided voltage on stator resistors. At high speed, the primary reason is the effect of inaccuracy of *ke* according to different motors. Therefore, a speed threshold is set. If *Spd_S > Spd_T_1*, the estimation algorithm shown in Fig. 7 is used and *kc* is the output of the regulator to correct the estimated speed. If *Spd_S < Spd_T_2*, the estimation algorithm shown in Fig. 6 is used and *vc* is the output of the regulator to compensate divided Voltage on stator resistors. Avoiding repeatedly jumping, there is a hysteresis value between *Spd_T_1* and *Spd_T_2*. The selection of *Spd_T_1* and *Spd_T_2* is based on the period of speed loop, the number of poles of BLDC, and the number of Hall-effect sensors. Following

rules can be used: 1) the longer the period of speed loop, the smaller the value of *Spd_T_1*. 2) The more the number of the poles of BLDC motor, the smaller the value of *Spd_T_1*. 3) The more the number of Hall-effect sensors, the smaller the value of *Spd_T_1*. 4) The hysteresis value between *Spd_T_1* and *Spd_T_2* can be selected by experimental results.

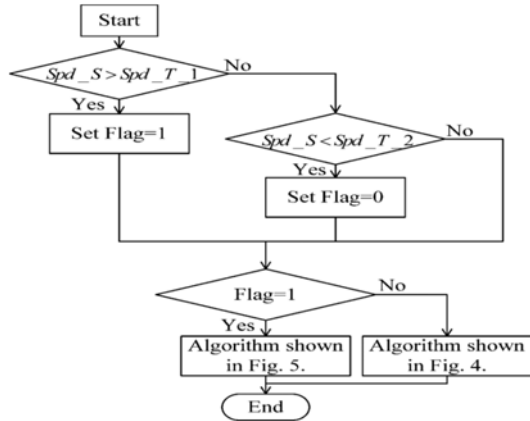The flowchart of estimation algorithm is as shown below

Fig.8.Flow chart of estimation algorithm.

IV. SIMULATION RESULTS

Firstly, outputs of BLDC motor i.e. voltage and current are converted into d-q axis with respective stator are given to Reference and Adaptive model of MRAC. Now these outputs i.e. voltage and current are inputs of MRAC in d-q axis. Finally the output of MRAC is given to PI Controller. By this way BLDC motor speed can be controlled.

The simulation results of MRAC based speed control of Brushless DC Motor with low resolution Hall Effect sensors is as shown below
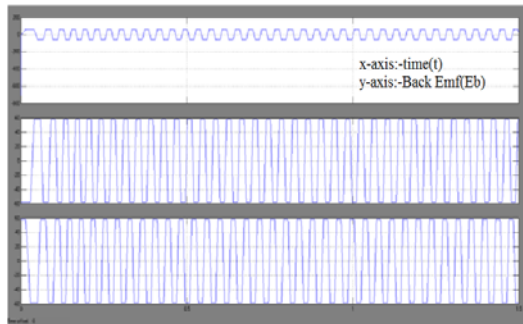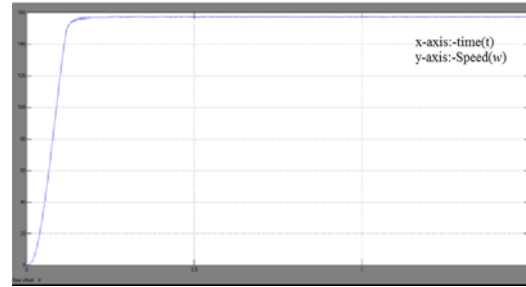

Fig.9.Back emf's of BLDC Motor with MRAC

Fig.10.Speed Characteristics of BLDC Motor with   MRAC

V.CONCLUSION

In this paper, a novel speed estimation algorithm based on MRAC is introduced. The proposed algorithm includes two regulators. One regulator corrects back EMF coefficient at high speed. The other regulator compensates the divided voltage of stator resistors at low speed. In this way, the estimation algorithm can work validly at both high speed and very low speed. The drive system with the proposed algorithm widens the speed range of BLDC motors. Moreover, it is not needed to tune parameters according to motors with different back EMF coefficient when using the estimation algorithm.

Extensive simulation have been performed and the results verify that the estimation algorithm proposed in this paper is effective.

REFERENCES

[1] N. J. Kim, H. S. Moon, and D. S. Hyun, "Inertia identification for the speed control of induction machines," *IEEE Trans. Ind. Appl.*, vol. 32, no. 6, pp. 1371–1379, 1996.
[2] K. B. Lee, J. Y. Yoo, J. H. Song, and I. Choy, "Improvement of low speed operation of electric machine with an inertia identification using ROELO," *IEE Proc.-Elect. Power Appl.*, vol. 151, no. 1, pp. 116–120, 2004.
[3] H.-W. Kim and S.-K. Sul, "A new motor speed estimator using Kalman filter in low-speed range," *IEEE Trans. Ind. Electron.*, vol. 43, no. 4, pp. 498–504, Aug. 1996.

[4] A. Yoo, S. K. Sul, D. C. Lee, and C. S. Jun, "Novel speed and rotor position estimation strategy using a dual observer for low resolution position sensors," *IEEE Trans. Power Electron.*, vol. 24, no. 12, pp. 2897–2906, Dec. 2009.

[5] R. Petrella, M. Tursini, L. Peretti, and M. Zigliotto, "Speed measurement algorithms for low resolution incremental encoder equipped drives: A comparative analysis," in *Proc. Int. Aegean Conf. Electrical Machines Power Electron,* Sep. 2007, pp. 780–787.

[6] Y. X. Su, C. H. Zheng, S. Dong, and B. Y. Duan, "A simple nonlinear velocity estimator for high-performance motion control," *IEEE Trans. Ind. Electron.*, vol. 52, no. 4, pp. 1161–1169, Aug. 2005.

[7] Y. X. Su, C. H. Zheng, P. C. Mueller, and B. Y. Duan, "A simple improved velocity estimation for low-speed regions based on position measurements only," *IEEE Trans. Control Syst. Technol.*, vol. 14, no. 5, pp. 937–942, Sep. 2006.

[8] J. Bu and L. Xu, "Near-zero speed performance enhancement of PM synchronous machines assisted by low-cost Hall effect sensors," in *Proc. 13th Ann. IEEE Appl. Power Electron. Conf. Exp.*, 1998, vol. 1, pp. 64–68.

[9] K. Hyunbae, Y. Sungmo, K. Namsu, and R. D. Lorenz, "Using low resolution position sensors in bump less position/speed estimation methods for low cost PMSM drives," in *Proc. IEEE 40th IAS Ann. Meeting Conf. Rec.*, 2005, vol. 4, pp. 2518–2525.

[10] S.Morimoto, M.Sanada, and T. Takeda, "Sinusoidal current drive system of permanent magnet synchronous motor with low resolution position sensor," in *Proc. IEEE 31st IAS Ann. Meeting Conf. Rec.*, 1996, vol. 1, pp. 9–14.

[11] R. D. Lorenz and K. W. Van Patten, "High-resolution velocity estimation for all-digital, AC servo drives," *IEEE Trans. Ind. Appl.*, vol. 27, no. 4, pp. 701–705, Jul./Aug. 1991.

[12]Z.Feng and P.P.Acarnley, "Extrapolation technique for improving the effective resolution of position encoders in permanent-magnet motor drives," *IEEE/ASME Trans. Mechatronics*, vol. 13, pp. 410–415, Aug. 2008.

[13] T.Emura and L.Wang, "A high resolution interpolator for incremental encoders based on the quadrature PLL method," *IEEE Trans. Ind. Electron,* vol. 47, pp. 84–90, Feb. 2000.

[14] C. Nasr, R. Brimaud, and C. Glaize, "Amelioration of the resolution of a shaft position sensor," in *Proc. Power Electron. Appl. Conf.*, Antwerp, Belgium, 1985, vol. 1, pp. 2.237–2.241.

[15] A. E. Fitzgerald, Charles KingsleyJr., and Stephen D. Umans, *Electric Machinery 6th edn*.Beijing:Tsinghua Univ. Press, 2003.